8-2005

A Computational Model to Predict *In Vivo* Kinetics in Implanted and Non-Implanted Shoulders

Matthew Brennon-Kyle Kubo
University of Tennessee, Knoxville

To the Graduate Council:

I am submitting herewith a thesis written by Matthew Brennon-Kyle Kubo entitled "A Computational Model to Predict *In Vivo* Kinetics in Implanted and Non-Implanted Shoulders." I have examined the final electronic copy of this thesis for form and content and recommend that it be accepted in partial fulfillment of the requirements for the degree of Master of Science, with a major in Engineering Science.

Richard D. Komistek, Major Professor

We have read this thesis and recommend its acceptance:

Mohamed R. Mahfouz, William R. Hamel

Accepted for the Council:
Carolyn R. Hodges

Vice Provost and Dean of the Graduate School

(Original signatures are on file with official student records.)

To the Graduate Council:

I am submitting herewith a thesis written by Matthew Brennon-Kyle Kubo entitled "A Computational Model to Predict *In Vivo* Kinetics in Implanted and Non-Implanted Shoulders." I have examined the final paper copy of the thesis for form and content and recommend that it be accepted in partial fulfillment of the requirements for the degree of Master of Science, with a major in Engineering Science.

Richard D. Komistek, Major Professor

We have read this thesis and

recommend its acceptance

Mohamed R. Mahfouz

William R. Hamel

Acceptance for the Council:

Vice Chancellor and Dean of
Graduate Studies

To the Graduate Council:

[illegible]

Major Professor

We have read this thesis and recommend its acceptance:

[illegible]

[illegible]

Accepted for the Council:

[illegible]

Vice Chancellor and Dean of Graduate Studies

A COMPUTATIONAL MODEL TO PREDICT *IN VIVO* KINETICS IN IMPLANTED AND NON-IMPLANTED SHOULDERS

A Thesis
Presented for the
Master of Science Degree
The University of Tennessee, Knoxville

Matthew Brennon-Kyle Kubo
August, 2005

Dedication

This thesis is dedicated to my parents Jerry and Judi Kubo, who not only taught me perseverance through trial, but who embodied servant leadership through serving their children with their lives and growing them up in the LORD. I hope to honor you with my life. May you be filled with joy and peace as you live out your days together. To Rebecca, my lovely wife-to-be, I have never known love, encouragement and hope as strong as yours. I look forward to the new adventures we will enjoy together! I love you. Finally, to Him who is, who was, and who is to come, be honor, praise, and glory forever!

Acknowledgements

I would like to thank all those who helped me in the pursuit of this Master of Science Degree in Engineering Science. I would like to thank Dr. Komistek for helping me to realize my potential through an opportunity to work in his lab. I thank him also for his patience and the many opportunities he provided me to increase in knowledge and skill in my craft. I give many thanks to Dr. Mohamed Mahfouz for giving me responsibility for this study. He was responsible for the design of the 2D-to-3D registration method and loci tracking software used in this project, as well as the design of the metal artifact reduction algorithm. These elements were critical to the success of this thesis. I would also like to thank Dr. Hamel for his mentorship during graduate school, encouragement, and for his attentive ear. I would like to extend a special thanks to Zimmer, Inc. for funding this project. I would also like to thank Dr. Greg Nicholson and Dr. David Hovis for providing the patients for this study.

I would like to thank my colleague Adrija Sharma, for his patience, knowledge, skill, and invaluable help during the past two and a half years of my endeavor towards this degree. You have the gift of teaching. I hope to hear of you using it to the benefit of many. I would also like to thank Mitchell Ladd and Emily Pritchard for performing metal artifact reduction and segmentation of the CT datasets used in this study. Finally, to Shaun, Katie, Joey, and Joel, thank you for your friendship and encouragement throughout graduate school. We made it!

Abstract

The purpose of this study was to develop and implement a computational model designed to input *in vivo* kinematics and predict *in vivo* forces and torques for the shoulder, elbow, and wrist in normal, rotator cuff-deficient (RCD), reverse shoulder arthroplasty (RSA) and total shoulder arthroplasty (TSA) shoulder subjects. Twenty subjects, divided evenly amongst the four shoulder types, performed a box-lift activity while under fluoroscopic surveillance. Three dimensional (3D) *in vivo* kinematics was determined for the subjects using implant models and bone models created from CT (computed tomography) scans in a 2D-to-3D registration process. The kinematics were used as input for an inverse dynamics mathematical model, and the subject-specific kinetics were derived. Average resultant shoulder forces were 78.3N (range: 70.4N to 117N, SD: 5.213), 102N (range: 90.2N to 180.2N, SD: 12.339), 94.9N (range: 84.9N to 149N, SD: 10.02), and 92.5N (range: 87.984N to 95.370N, SD: 1.848), for normal, RCD, RSA, and TSA subjects, respectively. Average resultant shoulder torques were 23.6Nm (range: 8.32Nm to 73.7Nm, SD: 11.227), 29.6Nm (range: 22.892Nm to 71.377Nm, SD: 7.581), 27.2Nm (range: 19.961Nm to 59.352Nm, SD: 6.664), 20.3Nm (range: 11.700Nm to 31.409Nm, SD: 6.496), for normal, RCD, RSA, and TSA shoulders, respectively. This study revealed that RCD subjects exhibited a decreased ROM (range of motion) of the humeral head with respect to the glenoid, as compared to the other groups. This study also showed that subjects having a rotator cuff-deficient shoulder and/or a replaced shoulder tend to use compensatory motions to perform the task of lifting a box, and, as a result, they experience greater forces at the glenohumeral joint. Paradoxically, the RCD subjects experienced the highest joint forces and torques among the different shoulder types.

Table of Contents

List of Tables

List of Figures

List of Abbreviations

Chapter 1

Background

1.1 Anatomy of the Shoulder

The shoulder, or glenohumeral, joint is an enarthroidal, or, "ball and socket" joint, linking the arm to the thoracic region of the torso. The arrangement of the bones and soft-tissues which comprise the shoulder joint allows for considerable movement, and a greater range of motion (ROM) as compared to all other articular joints in the human body. Like the knee and other synovial joints, the shoulder is encapsulated by a number of muscles and ligaments, and is lubricated by synovial fluid, a natural lubricant produced by the human body.

1.1.1 Bone Structure

The bones entering into the formation of the shoulder joint are the humerus (upper arm bone), which inserts into the shallow glenoid cavity of the scapula (or shoulder blade),

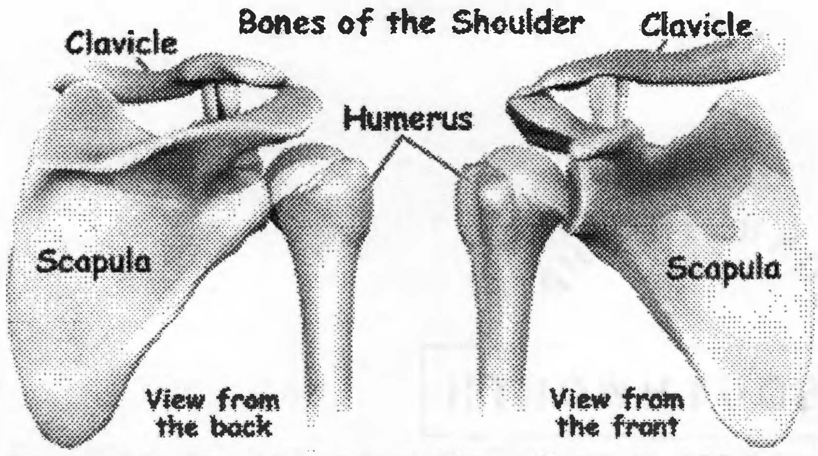

Figure 1-1: Bones of the Shoulder [Adapted from the Medical Multimedia Group]

the scapula, and the clavicle (collar bone).

The Scapula

The scapula forms the back part of the shoulder joint. It is a large, flat, triangular-shaped bone, positioned at the posterior and lateral regions of the thorax, and extends between the second and seventh (or eighth) ribs. At its superio-lateral extremity, the scapula has two extensions, one located anteriorly and the other posteriorly (Figure 1-1). The tip of the posterior extension, called the Acromion Process (acromion), forms the roof of the shoulder joint. The entire posterior structure extends laterally and anteriorly from the base of the Supra-Spinatus, a valley comprising the superior topology of the scapula, via a plate of hard bone, called the "Spine," and ends at the acromion. The acromion and clavicle join via ligamentous tissue to form the acromioclavicular (A/C) joint, which assists the surrounding joint musculature in constraining the humeral head to the glenoid cavity (glenoid). The A/C joint also provides flexibility for the scapula. The glenoid is a shallow depression on the superio-lateral aspect of the scapula and is the site of insertion for the proximal humerus into the shoulder joint. It is situated between the acromion, and the coracoid processes.

The extension upon which the glenoid rests is called the neck of the scapula, and is the site of lateral connection for the acromion and coracoid processes to the scapular body. The coracoid process (coracoid) is a thick, curved process of bone which arises from the neck of the scapula; it is directed, at first, upward and inward, then, becoming smaller, it changes its direction and passes forward and outward. Overall, the scapula is composed internally of cancellous (trabecular, or "spongy") bone, and externally of cortical bone. However, the majority of the scapular body is composed of thin cortical bone – so thin it is, in some cases, transparent.

The Humerus

The humerus is the longest bone in the upper extremity and is, itself, considered to be the arm. Like the scapula, it is composed of cortical and cancellous bone. The humerus is comprised of a proximal articulation, shaft, and a distal articulation. Both the proximal and distal ends of the humerus enter into joints which operate the majority of the upper extremity. The proximal humerus is hemispherical in shape and it's bearing surface is covered with articular cartilage. This region is called the "head" of the humerus. Just below the circumference of the humeral head, there lies a tapered region of bone known as the anatomical neck. The anatomical neck separates the head from the greater and lesser tuberosities, which project out to form muscle attachment sites. The greater tuberosity is located on the lateral aspect of the humerus and projects likewise from the humeral head, while the lesser tuberosity is located anterior to the head and projects itself forward. As the shaft projects distally, one finds multiple attachment sites for muscles to operate the humerus.

Terminating the shaft is the distal articulation. Projecting from either side are the condyles. The articular surface of the distal humerus extends slightly lower than the condyles, and is also covered with cartilage for articulation with the radius and ulna, the two bones comprising the lower arm, just above the hand. Together these bones comprise the shoulder and elbow joints, responsible for the majority of upper extremity operation.

1.1.2 Soft Tissues

Altogether, there are eleven main muscles that provide motion to the shoulder from insertion and attachment points on both the scapula and humerus. There are six important muscles responsible for shoulder movement and maintaining the integrity of the shoulder joint. The muscles can be grouped by regions relative to the bone(s) from which they originate; they are the: acromial, anterior scapular, posterior scapular, anterior humeral and posterior humeral regions.

From the acromial region of the scapula originates the deltoid muscle, which gets its name from its resembling the inverse of the greek letter delta (Δ). This muscle arises from the anterior aspect of the clavicle, acromion process, and the posterior border of the spine of the scapula, and inserts into the lateral aspect of the humeral shaft via a large, fibrous tendon. The deltoid is responsible for abducting the arm away from the body, so as to create a right angle between the arm and torso.

Muscles of the Rotator Cuff

Inferior to the deltoid are four muscles that comprise the rotator cuff. The rotator cuff, as can be seen in Figure 1-2, is the soft-tissue "cuff" which surrounds the shoulder joint and is responsible for managing arm movement and position. Also, a bursa, located beneath the acromion process provides lubrication for the rotator cuff. The muscles making the rotator cuff are the:

- Subscapularis
- Supraspinatus
- Infraspinatus
- Teres Major/Minor

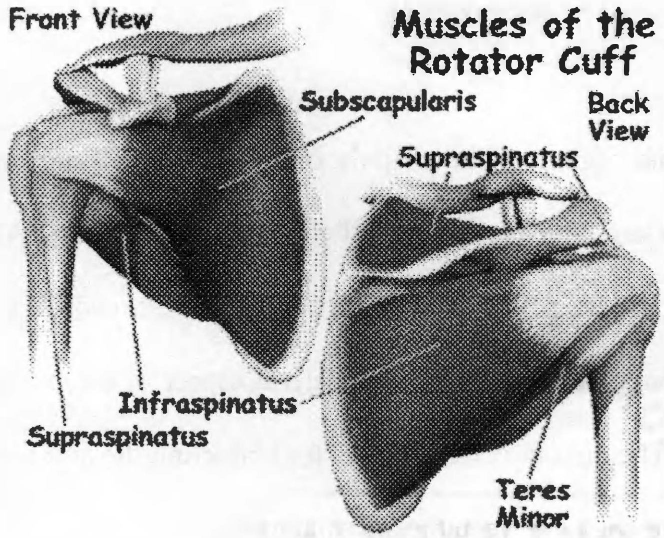

Figure 1-2: Muscles of the Rotator Cuff [Adapted from the Medical Multimedia Group]

The subscapular region on the anterior scapula gives rise to the subscapularis muscle. Its boundary of origin coincides with the perimeter of the subscapular fossa. The subscapularis muscle fibers extend outward and eventually meet to form a tendon which inserts into the lesser tuberosity on the humerus. Activation of the subscapularis muscle rotates the humeral head internally; when the arm is raised and also draws the humerus forward and downward (adduction) – action which defends the humeral head separation from the glenoid.

The Supraspinatus, Infraspinatus, and Teres Major form the posterior rotator cuff. The supraspinatus covers the entirety of the Supraspinous fossa (scapular body). It originates from the medial axis of the scapula, extends over the joint capsule, and attaches to the highest of three facets on the greater tuberosity of the humerus. The Supraspinatus muscle helps the Deltoid in abducting the arm away from the body, and also helps to fix the humeral head to the glenoid. The Infraspinatus muscle occupies the majority of the infraspinous fossa. Its muscle fibers cross the posterior portion of the capsular ligament of the shoulder and insert into the middle facet on the greater tuberosity of the humerus. The Teres Minor muscle originates from the lower-third of the axillary boundary of the scapula. The Teres Minor extends obliquely upward and outward and inserts into the lowest of three facets on the greater tuberosity. The Teres Major also extends upward and outward, and ends in a flat tendon that attaches to the humerus just below the greater tuberosity. Together the muscles of the posterior rotator cuff help to externally rotate and adduct the arm.

Articular Cartilage and the Capsular Ligament

Articular cartilage, made of smooth collagen fibers, covers the ends of the bones entering into the shoulder joint. This cartilage, lubricated by synovial fluid in the joint, allows the almost frictionless motion observed in the shoulder and other synovial joints in the body. Also surrounding the shoulder joint is the capsular ligament, joining the humerus to the scapula. The capsular ligament (Figure 1-3) performs similarly to the rotator cuff, in that it is responsible for maintaining the stability of the shoulder by preventing both small and large distractions of the humerus from the glenoid cavity.

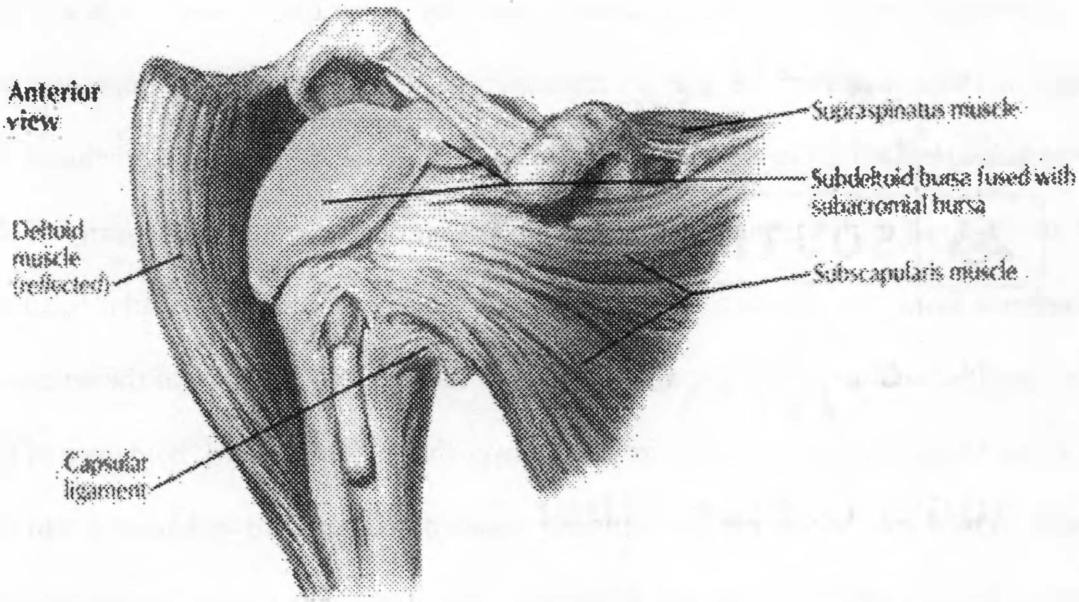

Figure 1-3: Shoulder Joint Capsule

There are multiple injuries and medical conditions that may result from such distractions. These are discussed in the following section.

1.2 Shoulder Injuries and Osteoarthritis

As the shoulder ages and/or becomes overused, as is likely in major league sports, or jobs requiring prolonged use of the hands in the overhead position, it becomes more susceptible to a number of joint injuries and disease. This section provides a brief outline of examples found in the patients required for this study.

1.2.1. Rotator Cuff Tears

There are a number of possible contributors to the occurrence of a rotator cuff tear. For instance, regular use of hands in an overhead position (i.e. baseball players, occupational necessity) can cause tendonitis and lead to an eventual rotator cuff tear. In more serious cases, a direct blow to the shoulder, as in a football tackle, or a fall onto an outstretched hand can cause dislocation of the shoulder and/or a possible full-thickness tear of the rotator cuff. Degeneration of the shoulder due to age can result in a rotator cuff tear known as a "degenerative tear." Also, bone spurs rubbing on tendons can cause rotator cuff tears.

1.2.2 Shoulder Impingement Syndrome

Shoulder Impingement Syndrome (SIS) is also common in those patients with a rotator cuff tear, and is typically the result of regular use of the hands in the overhead position. SIS is caused by compression of the rotator cuff between the acromion and the proximal head of the humerus. The compression and rubbing of the tendons against bone causes inflammation, pain, and weakens the rotator cuff. In some cases small chips of bone (bone spurs) may be present at the bone/rotator cuff interface, initiating the rotator cuff tear. Inflammation of the bursa due to SIS may also occur. This and the former condition are known as bursitis and tendonitis (tendinitis), respectively. These conditions can be treated with a combination of rest, ice, and anti-inflammatory medications. For intense, debilitating pain, steroid injections are sometimes used. When the aforementioned treatments fail, arthroscopic surgery is sought. To alleviate the pain and rubbing in impingement cases, pieces of the acromion can be removed through small incisions in the shoulder, a technique called shoulder decompression. For a torn rotator cuff, the tear can be repaired by suturing the torn tendons back together. This technique is also done through small incisions in the shoulder. In the most severe cases of rotator cuff injury, the torn tendons of the rotator cuff are severely scarred and have retracted away from the shoulder joint. Total shoulder replacement is then considered as the remedy.

1.2.3. Shoulder Instability

Shoulder Instability is another problem that can occur in the injured shoulder. Shoulder instability results when the tendons of the rotator cuff and/or the capsular ligament are very weak or torn, and cannot keep the glenohumeral joint intact. Two types of shoulder instability are possible, based on severity. If the instability is mild, slight subluxations of the humerus into and out of the glenoid fossa may occur, usually in one direction. However, contact between the glenoid and proximal humerus remains. The most severe instability is called dislocation, where the humeral head comes completely out of the glenoid and is displaced in one or more directions from the seated position.

When the rotator cuff is severely torn, dislocations may become a regular event. Thus, the sliding motion of the humerus against the scapula will eventually wear the articular head and glenoid, to bone-on-bone contact between the two. Another result may be the development of osteophyte on the glenoid and/or the humeral head. Osteophyte show up in radiographs or fluoroscopy as abnormal bone growth at the periphery of the glenoid fossa or at the base of the humeral head, just above the anatomical neck.

The painful combination of a torn rotator cuff and osteoarthritis is called rotator cuff arthropathy. Patients with rotator cuff arthropathy will typically forego pain medications and physical therapy, as these are insufficient in treating the damage, and opt for total shoulder replacement.

1.3 Total Shoulder Replacements

Patients with rotator cuff arthropathy experience pain and decreased range-of-motion (ROM). However, in some cases, the rotator cuff may remain intact for the majority of these shoulders, but it functions poorly due to bone deformity (osteophyte) and soft-tissue contracture. In these cases, total shoulder arthroplasty has proven to be a successful procedure for pain relief and improved ROM. In shoulder arthroplasty (Figure 1-4), the humeral head is typically resurfaced with a Cobalt-Chrome (Co-Cr) hemisphere and attached to a stem (titanium, or Co-Cr) that is inserted into the upper arm. The resurfaced humerus may be allowed to articulate with the natural glenoid, if it is still healthy. This type of procedure is called a hemi-arthoplasty. If the glenoid is also diseased, it may be

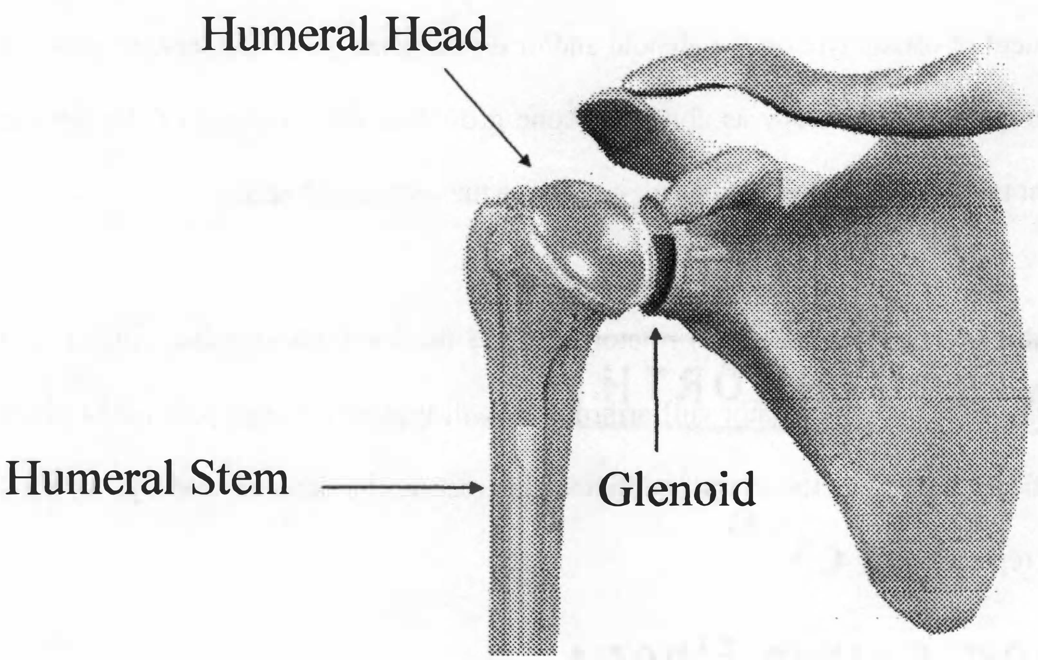

Figure 1-4: Example of Total Shoulder Arthroplasty Components [Adapted From Medical Multimedia Group]

replaced with an insert made of Ultra High Molecular Weight Polyethylene (UHMWPE). Such a procedure is referred to as total shoulder arthroplasty (TSA). The insert may be implanted as-is, or may have metal backing. A third technique, called reverse shoulder arthroplasty, is utilized to treat rotator cuff deficiency, joint injury, and shoulder dysfunction when no other satisfactory option is available. For this modality, a Co-Cr hemisphere, as in the hemi-arthroplasty, is used to replace the glenoid, and the mating UHMWPE surface is inserted into the metallic stem implanted in the upper arm. The ultimate functionality of these shoulder arthroplasty depends upon multiple factors, including alignment of the prosthetic implant, rotator cuff muscle belly health, soft-tissue balance achieved from surgery, and patient compliance with rehabilitation.

Chapter 2

Literature Review

2.1 Motion Studies

Previously, the majority of scapular and glenohumeral kinematic studies have been conducted under *in vitro* conditions, using cadaveric specimens. However, several more recent studies have utilized a number of alternative approaches to determine the *in vivo* kinematics of the shoulder. Both invasive (McClure 2001, Koh 1998) and non-invasive (Rhoad 1998, Borstad 2001, Kelkar 2001, Yamaguchi 2000, Baeyens 2001, Eisenhart-Roth 2002) techniques have been implemented. Some of the more invasive techniques include the use of inter-cortical bone bins fitted with optical sensors to track scapular motions (McClure 2001, Koh 2001). This method does provide direct *in-vivo* data, but is not widely accepted, due to the inherent risks involved in invasive techniques.

A number of more recent, non-invasive techniques used to record *in vivo* kinematics of the shoulder and other joints, such as the knee and hip, include strict use or combinations of fluoroscopy (Dennis 2003), computed tomography (Mahfouz, 2003), magnetic resonance imaging (MRI) (Rhoad 1998, Baeyens 2001, Eisenhart-Rothe 2002), and radiographic analysis (Yamaguchi 2000). Skin markers have also been used to gather kinematic data non-invasively (Andriacchi 2000, Alexander 2001, Borstad 2002), but are known for the error induced by relative motion between the skin and underlying bone during dynamic analyses. Fluoroscopic techniques have become increasingly more popular and have proven to yield very accurate kinematic results under *in vivo* conditions (RMS error of 0.4° rotation and 0.1mm translation; Mahfouz 2003).

2.2 Force Studies

According to literature, the determination of forces in the upper extremity consists of both *in vitro* cadaveric methods (Gupta, 2005) as well as a number of *in vivo* methods (Murray and Johnson, 2004). Others have also tried electromagnetic and electromyographic methods to track motions and predict muscle forces (Pascoal et al., 2000). A more recent attempt has been made to validate the use of implantable force transducers in the measurement of *in vivo* muscle tendon forces (Bull et al., 2005).

The majority of cadaveric studies involve test rigs that produce results hampered by the inherent limitations of such studies, i.e. use of simulated joint forces based on unspecified criteria. Furthermore, the motions these rigs produce are limited to each rig's capability to produce a certain number of motions, and mimic the natural rhythm of the joint *in vitro*. Cadaveric studies are also limited in application to musculoskeletal biomechanics because they are performed in a static loading environment, whereas human joints are largely dynamic systems.

Another widely used method in the determination of *in vivo* joint forces is the incorporation of telemetric sensors interfaced with natural and artificial joints. Such sensors have been used successfully in knees and hips. However, successful use of telemetric sensors for the determination of upper extremity joint forces has not, to the author's knowledge, been widely published. While telemetry does provide direct, real-time *in vivo* measurement of joint forces, the cost in producing the sensors, risk of damaging the sensors, and the risk to subject health, make them a work-in-progress.

Less invasive methods of determining *in vivo* forces of the upper extremity include the use of skin markers tracked by cameras to gather kinematic data for computational model inputs (Murray and Johnson 2004), monitoring the electromyographic (EMG) activity of muscles to predict joint loads (Laursen et al., 1998), and mathematical modeling (Komistek 1998, Murray and Johnson, 2004). The use of skin markers to determine *in vivo* joint kinematics carries its large potential for error over to their use in determining *in* *vivo* forces. It is well documented that such methods contain error due to the relative motiȯn between the skin and underlying bone (Fuller 1997, Alexander 2001)

More recently, the use of mathematical modeling has presented an efficient, non-invasive means of determining *in vivo* forces theoretically. Previous mathematical models have employed two techniques to arrive at a solution. These are optimization techniques and reduction techniques. The human body can be viewed as an indeterminate system, as the number of unknowns (i.e. muscle forces) to be solved for vastly outnumbers the maximum number of DOF (i.e. a maximum of six, when considering the shoulder, for example) in the system. Since this is the case, optimization techniques attempt to minimize strategically formulated cost functions based on the inequality of unknown quantities to known quantities in the system, in order to come up with a solution. Brand et al. has shown that these methods tend to produce higher results than those experimentally determined through telemetry (Brand et al., 1994). According to Komistek, the observed results may be high due to the grouping of the available muscles, such that each is theoretically determined to carry a load greater than the actual (Komistek 2005).

On the other hand, those mathematical models utilizing the reduction technique contain underlying assumptions that allow for a determinate system – where the number of unknowns (i.e. muscle/interaction forces and/or torques) equals the number of dynamic equations that can be solved. Here, the underlying assumption is that certain muscles do not greatly influence the system, and their effect can be neglected. For some other models, it is assumed that the muscles in the system can be grouped together, and that the force produced by the group is a good estimate of the force produced by each muscle contributing to the group (Komistek 2005). It is this latter assumption that has been incorporated into the present model.

To date, there are a number of studies that have been conducted to experimentally (with telemetry) and theoretically (with mathematical modeling) determine forces in several joints, including the hip and knee. However, accurate experimental and theoretical data regarding *in vivo* motions, forces and torques in the shoulder is somewhat lacking in literature. Therefore, the purpose of this study was to utilize proven methods in fluoroscopy, CT data analysis, and mathematical modeling to improve and expand upon existing kinematic and kinetic data for the shoulder.

Chapter 3

Statement of Purpose

The use of various types of telemetry, medical imaging and computational methods in the determination of *in vivo* motions and forces for biomechanical systems has been widely successful. A plethora of information exists, describing the dynamics of the shoulder joint while performing different tasks. However, these studies have focused on normal and degenerative shoulders *in vivo* and *in vitro* only. There has been no data published (to the author's knowledge) comparing implanted and non-implanted shoulders under *in vivo*, weight-bearing conditions. Thus, the ability to assess the performance of the shoulder pre-and post-operatively has great clinical relevance.

The purpose of this study was to use established methods in fluoroscopy, and CT for kinematic analysis and to devise a computational model capable of utilizing the *in vivo* kinematics obtained through these methods to predict the *in vivo* joint forces and torques for the shoulder, elbow, and wrist during a dynamic box-lift exercise. It is hypothesized that the mathematical model will predict TSA and RSA shoulder forces that are similar in pattern and magnitude to those of the normal shoulder, but the subjects having a RCD shoulder will experience more variable forces, with differing patterns and magnitudes.

Chapter 4

Materials and Methods

4.1 Study Population and Implant Description

Twenty subjects comprising four categories of shoulder conditions were chosen for this study. Five subjects had a normal shoulder with no bone and/or soft-tissue injury, or disease; five were rotator cuff-deficient (RCD), five had a total shoulder arthroplasty (TSA), and five had a reverse shoulder arthroplasty (RSA) [TSA: B/F Shoulder; RSA: Implex Reverse, Zimmer, Inc.]. The rotator cuff-deficient patients each suffered from rotator cuff arthropathy, expressing itself through a chronic rotator cuff tear (event causing initial tear unknown), where the humeral head is observed sliding in either the superomedial or superolateral directions relative to the glenoid, initiating the onset of osteoarthritis (OA). All RCD patients also showed the existence of osteophyte growth on both the acromion and glenoid. Subjects having a primary arthroplasty had both their humeral head and glenoid replaced. The patients in this study who did not have the necessary shoulder constraints for a primary arthroplasty underwent reverse shoulder

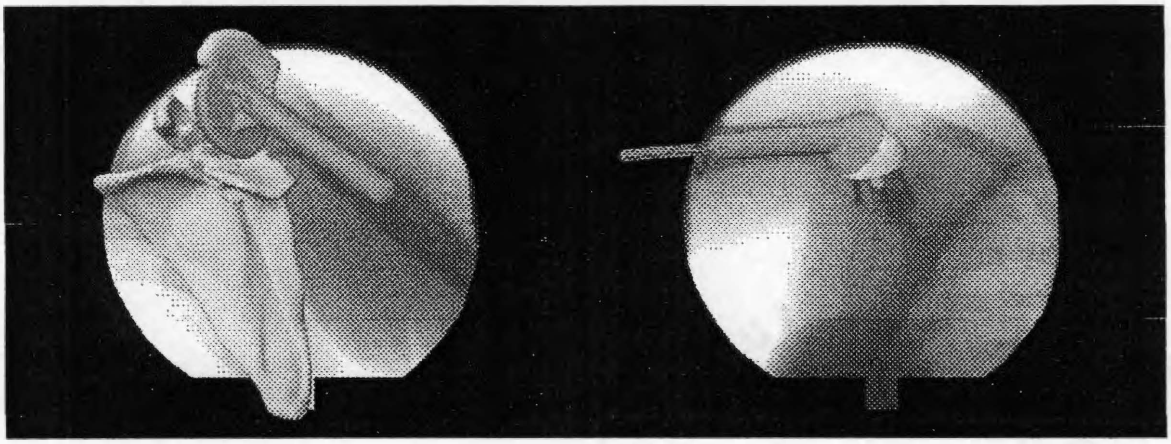

Figure 4-1: Example of TSA (left) and RSA (right) Shoulder Arthroplasties

arthroplasty for chronic rotator cuff-deficiency, anterior shoulder instability (ASI), pain, and shoulder dysfunction. The reverse implants were customized for each patient, depending on the nature of the damage to their shoulder.

The Bigliani/Flatow (B/F) total shoulder (Figure 4-1, left) is a commercially available design which consists of a low-profile, Neer-Style (Cobalt-Chrome (Co-Cr) humeral stem, modular Co-Cr humeral head and ultra high molecular weight polyethylene (UHMWPE) glenoid. The low-profile stem preserves bone stock, and the glenoid provides a unique variable-conformity articular surface, where the glenoid size and offset can be changed incrementally to best match the anatomical position of the replaced bone. The articular design provides joint stability throughout the ROM while reducing improper loading of the implant and associated wear. The reverse-style implants consisted of a series of custom components used primarily in revision surgeries. For these implants, a stem with a dished, articular surface replaced the humeral head articulation proximally, and the UHMWPE glenoid insert found in the TSA was replaced by a Co-Cr glenosphere (Figure 4-1). The custom designs utilized porous tantalum (Ta) and solid titanium (Ti) alloy for the stem and glenosphere base plates. An UHMWPE liner was cemented into the porous tantalum. The glenosphere attached to the base plate with a locking screw and taper. The tantalum surface provided a surface for bony apposition (osseous in-growth).

The patients with severe osteoarthritis underwent successful total shoulder arthroplasty. These patients had undergone no previous surgery and, therefore, had an intact rotator cuff. All subjects had cemented polyethylene glenoid and uncemented humeral components. Each had the long head of biceps immobilized as part of the procedure, and performed the same aftercare protocol. The average age at surgery was 63 years (range: 58 to 65 years). The average follow-up at the time of this study was 1.8 years (range: 1 to 2 years). The average Visual Analog Score (VAS) for pain dropped from 6.5 to 0.5 post-operatively, and the average active forward elevation improved to 155° (range: 145° to 168°). All RSA patients in this study had undergone previous surgery with sustained extreme shoulder dysfunction, pain, and ASI. Three had failed hemi-arthroplasty for fractures and two had multiple rotator cuff repair failures.

On average, these patients had experienced three (range: 1 to 5) surgeries. The average age was 63 years (range: 45 to 74 years), and pre-operative average scores were as follows: American Shoulder & Elbow Surgeons (ASES) Shoulder Index = 29.6 (range: 15 to 38); Simple Shoulder Test (SST) = 1.7 (range: 0 to 3), and Visual Analog Score (VAS) for pain = 6.4 (range: 3 to 9). The average pre-operative active motions were as follows: active forward elevation (AFE) = 35° (range: 10° to 60°), and external rotation (ER) = 6° (range: -15° to 20°).

4.2 General Methodology

Several precursory tasks were completed in order to determine the *in vivo* kinetics of the shoulders under study (Figure 4-2). Each of the subjects chosen for this study underwent a CT scan of their shoulder region and performed a box lift activity under fluoroscopic surveillance. The CT data was utilized to create 3D computer aided design (CAD) models of each subject's humerus and scapula, and/or implant components. The CAD models and fluoroscopic data were then used in a 2D-to-3D registration process to determine subject-specific kinematics. The kinematic data were used as input to an inverse dynamics model representing the box lift. Anthopometric data on body segment parameters was obtained from previous publications (D'Leva, 1996), and input to the model. The 2D-to-3D registration process was also used to determine the 3D motion of the humeral head within the shoulder joint – information which has not yet, to the author's knowledge, been published in literature.

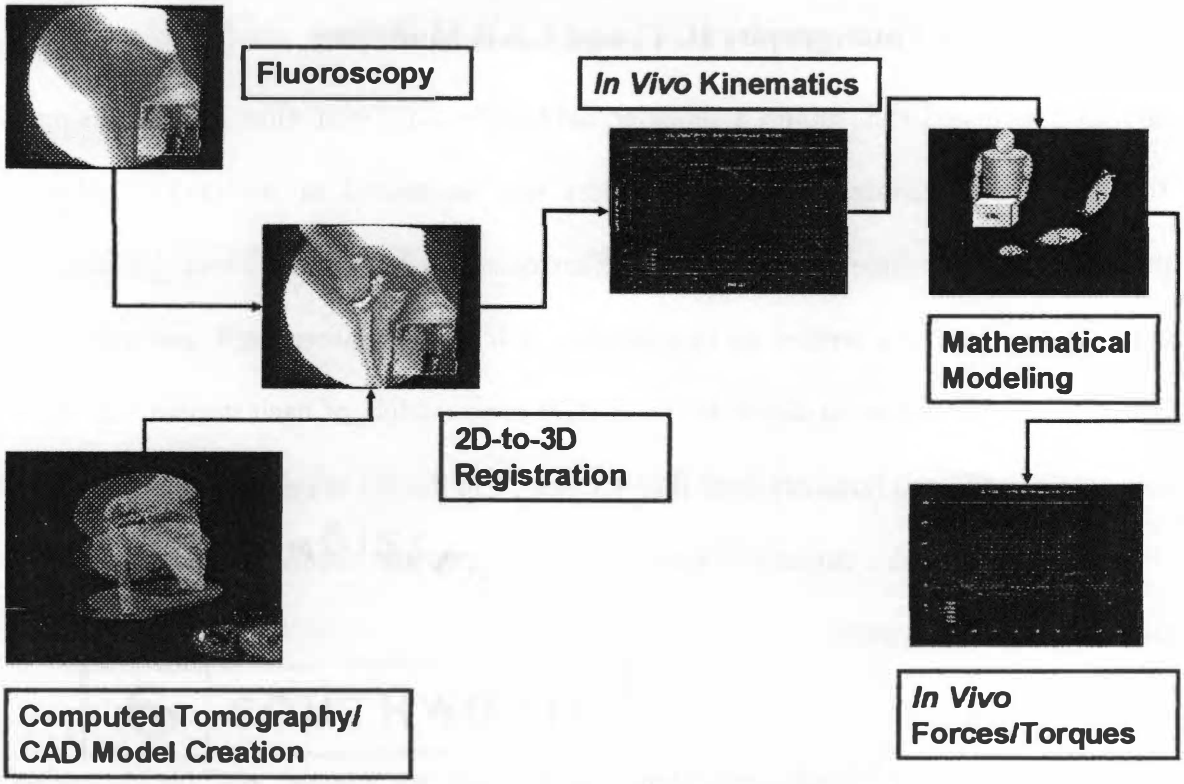

Figure 4-2: Flowchart for Methodology

4.3 Computed Tomography (CT) and CAD Modeling

Spiral CT scans of each subject's shoulder were made at 0.75mm slice intervals using a 16-detector CT scanner. The scanned data was segmented in Amira 3.0, using a threshold filter to isolate the bones from the surrounding soft tissues. Three dimensional bone density data was created by interpolation at 0.3 mm between each segmented CT image slice. 3D computer-aided design (CAD) bone models of each normal and RCD subject's scapula and humerus were then created from the 3D bone density data (Figure 4-2). The models were output in 'Open Inventor' format and consisted of approximately fifteen thousand polygons.

A lab-developed MATLAB algorithm was applied to remove any metal artifact (appearing as noise) from the TSA-implanted subjects' CT slices before the scapula was segmented. The TSA component models were provided in IGES format from the manufacturer and arranged in the correct pose using Pro-Engineer Wildfire 2.0™ and Mechanical Desktop 2004™. In order to more accurately determine the orientation of the humeral head on the stem, 3D CAD models of the TSA implants were also created from the CT data. This was necessary since the TSA implants can be configured to match subject-specific anatomy. Such information was not provided in the surgical notes and is not discernable from fluoroscopy alone. The RSA implant CAD models were provided in IGES format previously by the manufacturer, so no segmentation was required for the RSA subjects.

4.3.1 Metal Artifact Reduction

After the scan of a high-density object, like an implant, resulting images may include 'prominent streaks' known as metal artifacts which make the object in the image less distinguishable from the surrounding area. Through post-processing of the images these impurities can be eliminated, resulting in metal artifact reduction (MAR). High density or metal objects can cause these impure artifacts in the reconstructed image for two main reasons. The first is that extreme x-ray beam attenuation can result in incomplete data in the projections. The second is a result of beam hardening. Our discussion will be limited to the issue of missing data, since this was the cause for the metal artifact observed in this study.

Disrupted Data

During a CT scan a beam is emitted on one side of the object to be scanned by an x-ray source at a given point. This beam is registered by a detector arranged on the other side. The detector senses the photons that are not being absorbed by the object during the scan. These distinctive photons are then used to recreate the image based on CT filtered back-projection (FBP) algorithms, after taking into account the density and thickness of the object they were passed through. High density objects, such as the shoulder implants examined in this study, usually stop the incident photons from the x-ray beam, and leave the detectors with no good transmission data to record for the particular slice. Thus, the missing data causes the white streaks observed in the respective CT slice.

Methods for MAR

Procedures for MAR include iterative and interpolative methods as well as algebraic reconstruction, scanning, wavelet and material change methods. Interpolation and iterative methods will be the focus here, as they were the methods used in this study to clean up the CT images.

Interpolation method

The interpolation method can be used in correlation to the data in several ways. For instance, if the implant and its effects are precisely known, you can readily interpolate the data in the image. It is frequently difficult to separate the image from the implant, however, and even harder to ascertain what the exact effects of the implant are on the image. This method, therefore, is usually applied to the radon transform of the image or to the image's projections. When you know the exact location of the implant and the locations of the streaks caused by the implant, you can fill in the missing data by interpolating in the radon space.

4.4 Fluoroscopy

Each subject, while under fluoroscopic surveillance in the frontal plane, performed a dynamic box lifting exercise with two hands on the box throughout the motion cycle. Subjects were positioned so as to make their scapula flush with the image intensifier while performing the box lift (Figure 4-3). A 4-lb. box was lifted from downward, full-

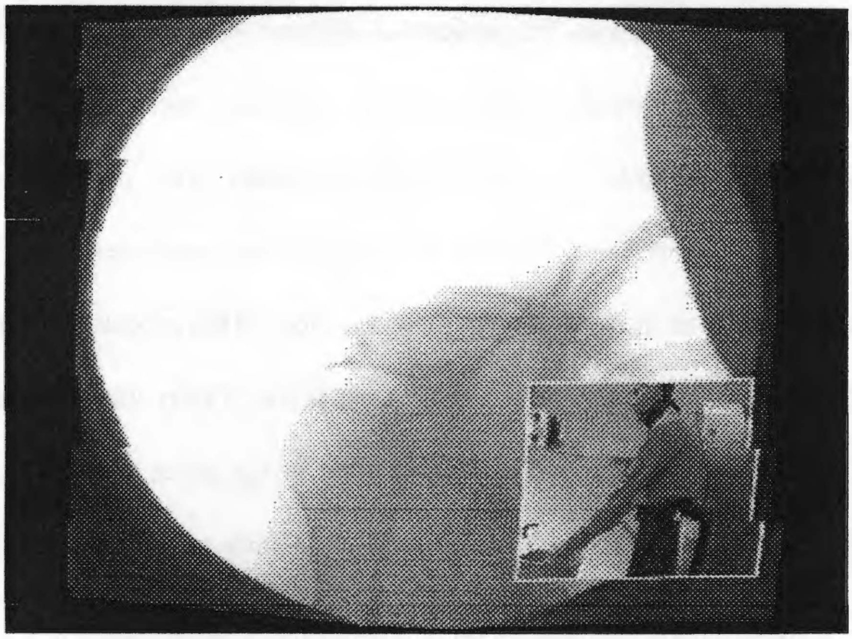

Figure 4-3: Fluoroscopic Image of Patient Performing Box Lift

arm extension to the top of the fluoroscopy unit and then retrieved. Fluoroscopic data was recorded in digital video format and downloaded to a workstation computer for further analysis. The video was recorded at thirty frames per second and produced 8-bit images. Using commercial video capturing software, a sequence of seven images representing the exercise from full extension to placing the box atop the fluoroscopy unit was captured for each subject's kinematic analysis. The images were sized at 640x480 pixels, and the current time at each capture of a pose was noted for use in curve-fitting the kinematic data before entering it into the mathematical model.

The images taken from the fluoroscopic video contain distortions that must be removed before the 2D-to-3D registration can be performed (Figure 4-4). In this study, a rectangular array of metallic beads was used to calibrate each image of the aforementioned sequence captured. A MATLAB program was used to create transformation coefficients that tell the distorted beads where they are in reference to the actual grid of beads and how to move to a coincident location. This process is known as "unwarping" (Figure 4-5). The advantage to this process is that it only has to be applied once for a particular fluoroscopy unit, and any subsequent image taken by the same unit can be unwarped with the respective transformations. Details of this procedure are outlined in a technical article by Mahfouz, et al. (Mahfouz et al., 2003).

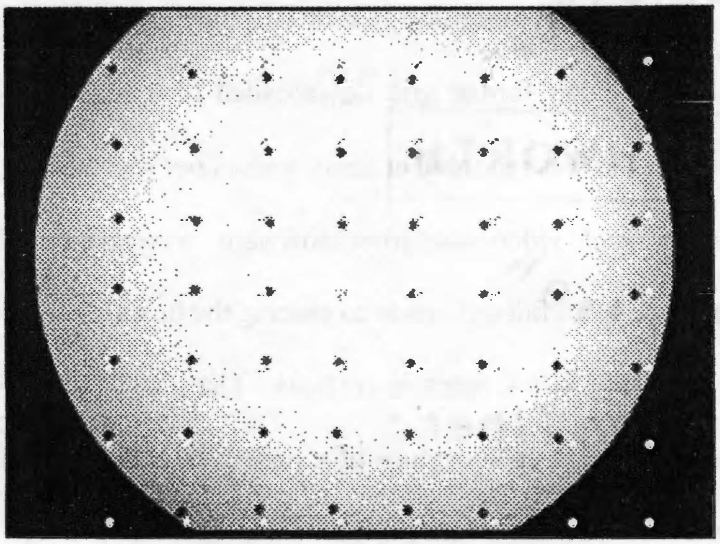

Figure 4-4: Example of Distortion in Fluoroscopy Image. The white dots are the original position of the beads in the grid, and the black dots are the distorted position of the beads.

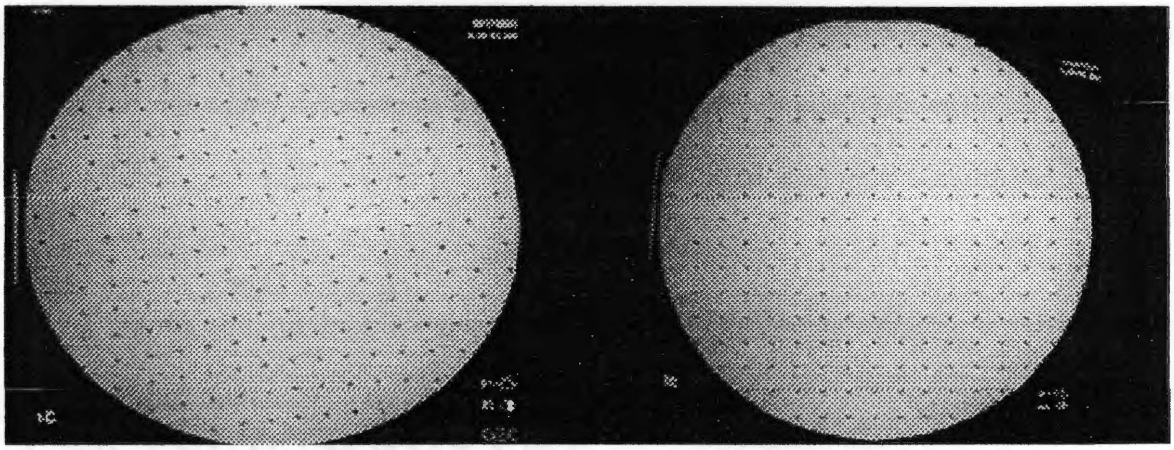

Figure 4-5: Example of Warped (left) and Unwarped (right) Images

4.5 2D-to-3D Registration

The method used here includes the same software and design elements used by Mahfouz, et al. (Mahfouz 2003). The technique involves the following steps: 1) an initialization step; 2) a matching algorithm which evaluates the match between the observed image and the predicted image from the current hypothesized pose; 3) a robust optimization algorithm; and 4) a method of supervisory control.

The purpose of the registration process is to be able to semi-automatically match the pose of 3D CAD models of bones and/or implants to their respective silhouette in the fluoroscopic image, in order to determine the 3D kinematics (three rotations and three translations) of the components in the 2D image.

Before performing the 2D-to-3D registration and pose estimation, we require geometric surface models of the bones and implant components. This step was taken care of previously with the provision of CAD models from the implant manufacturer and bone models reconstructed from each individual's CT scan.

This registration process encompasses the image matching algorithm, where a predicted X-ray image is matched to the actual X-ray image (Figure 4-6). The predicted image is created by illuminating the CAD model to create its projection onto the actual X-ray image. The projection and the actual image are matched by a comparison of two weighted metrics. The actual, unwarped, X-ray images from fluoroscopy are loaded into the software package, followed by the CAD models of implants and/or bones. The CAD models are automatically positioned with their geometrical center coinciding with the origin of the global coordinate system in the viewing plane. The geometrical center of the CAD models was determined by creating a 3D bounding box around the object and joining adjacent corners of the each face with diagonals. The location where the diagonals intersect was considered the geometrical center of the model.

To begin, the user manipulates the CAD models to approximate the match between the model pose and the silhouette of the implant/bone in the X-ray image. Once the user feels that he or she is close, they can opt to use an optimization function that is programmed into the software. The optimization technique is a robust algorithm called

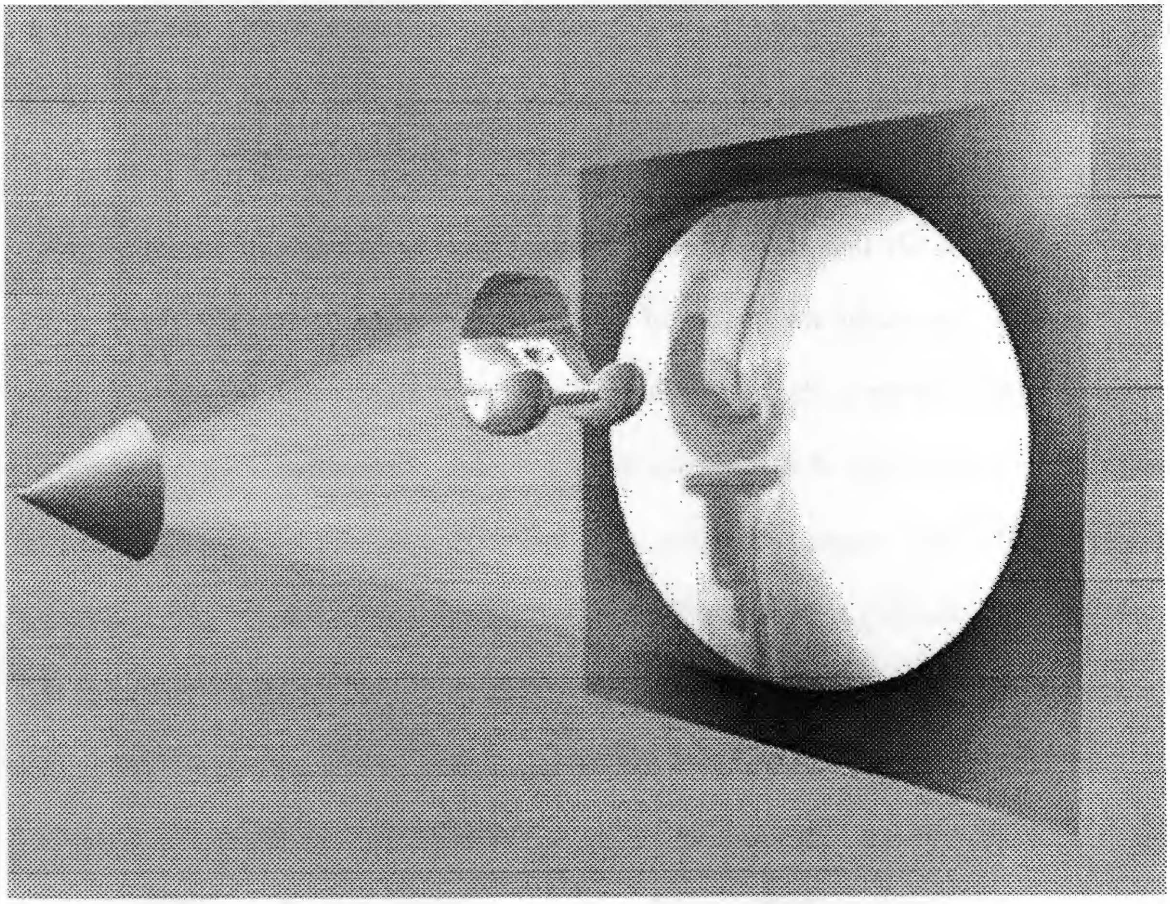

Figure 4-6: 2D-to-3D Registration [Adapted from Mahfouz 2003]

Simulated Annealing (SA). In its application to CAD model pose estimation, the SA algorithm will search the six-dimensional space (three rotations and three translations) to find a global minimum for a function comparing two weighted metrics. They are an intensity matching metric and a contour matching metric. The contour matching is weighted more heavily than the intensity matching since the intensity of the actual image can be greatly affected by the quality of the fluoroscopy video recorded. The intensity matching metric compares the pixel values of the two images, while the contour metric measures the coincidence of the edges of the two images. The optimal match is found by multiplying the two images, summing, and normalizing by the sum of the predicted image values. According to Mahfouz, making the contour score heavier than the intensity matching score allows the SA algorithm to more effectively find the global minimum and the exact match between the predicted and actual images. The accuracy of this method was found to be within a root mean square (RMS) value of 0.4° of rotation and 0.1mm of translation, with increasing RMS error for out-of-plane measurements (1.50° rotation and 0.65mm translation; Mahfouz 2003).

A limitation of all fluoroscopic matching processes is that they encounter difficulties when trying to automatically match symmetrical, or near-symmetrical objects to the X-ray images. Aside from the human scapula, the natural humerus and implant components are, for the most part, symmetrical. Therefore the automated process was not useful, and the registration was done manually.

4.6 Data Collection

Data collected from the registration process included the pose (three rotation and three translation) of the humerus/humeral component relative to the scapula or glenoid (in the case of RSA shoulders). The relative transformations were with respect to the geometrical center of the models, and not the actual centers of mass.

Loci tracking was performed, whereby one point was assigned to the most superior point on the normal and RCD humerus models, and four points were evenly distributed about the circumference of the humeral head. The same was done for the reverse implant models, where the superior point was placed at the center of the proximal face of the humeral component. A point was placed at the center of the glenoid cavity (for normal and RCD subjects) and at the most superior point at the center of the glenosphere (for RSA subjects). The translation of the aforementioned points designated to the humeral components was tracked with respect to the point on the glenoid/glenosphere in 3D space during the lift activity. The resulting data was used to determine translation of the humeral head in any combination of 2D planes created with the x-, y-, and z- point locations. Motion of the humeral head was tracked in the frontal plane for this study. This data was then used to determine relative separation of the humeral head from the glenoid. Once the kinematics was collected from the registration process, they were analyzed and input to the math model to determine *in vivo* forces and torques at the shoulder, elbow, and wrist.

4.7 Mathematical Model

An inverse-dynamics mathematical model, based on Kane's theory of Dynamics, (appendix B) was created to predict *in vivo* joint forces and torques for the shoulder, elbow, and wrist. The *in vivo* kinematics collected from the 2D-to-3D registration were then plotted with respect to time. The data was curve-fit to derive temporal motion functions that were input to the mathematical model and the results were calculated.

The choice of using Kane's equations was based on the proven efficiency to solve complicated, multi-body dynamics problems (Houston 1990; Kane 1983, 1985). Kane's method uses partial velocity and partial angular velocity vectors as multipliers in generalizing the active and inertial forces in the system. By doing so, the "nonworking," or non-contributing forces in the system are eliminated from the computation, and only the unknown forces, associated with the specified motions of the system are predicted. The current model assumes use of the reduction technique, keeping the number of unknown forces and torques to be solved for, equal to the number of derived equations.

4.7.1 Description of the Model

The free-body diagram (Figure 4-7) consists of the torso, designated as the fixed Newtonian (inertial) reference frame, the humerus (Body B), the radius and ulna (Body C) and the hand combined with the 4-lb. box (Body D); the hand and box were combined for simplicity. Point contact between bodies was assumed at each joint, and the scapula was considered fixed to the Newtonian reference frame. The global coordinate system (CS) was set up as follows: the $N_2>$ direction was oriented vertically upward (opposite of gravity), the $N_3>$ direction was directed from right shoulder to left and $N_1>$ was formulated as the cross multiplication of $N_2>$ by $N_3>$, according to the right hand rule (right hand coordinate system). Body B was given three rotational degrees of freedom (DOF) with respect to (w.r.t.) the Newtonian. Body C was given one rotational DOF in the sagittal plane (about $N_3>$) w.r.t. Body B, and Body D was also given one rotational DOF in the sagittal plane w.r.t. Body C. Separation of the humerus from the shoulder socket (glenoid) and frictional forces were neglected. Muscles were specifically solved for, but the predicted joint torques encompass the muscular force required to perform the box lift. We hypothesize that solving for joint torques, representing the muscle forces in the moment equations, and the appropriate use of generalized forces allows for accurate prediction of the joint forces.

Following the inclusion of bodies into the system, constants were declared, providing body segment dimensions and inertial properties. Next, to locate each of the bodies in

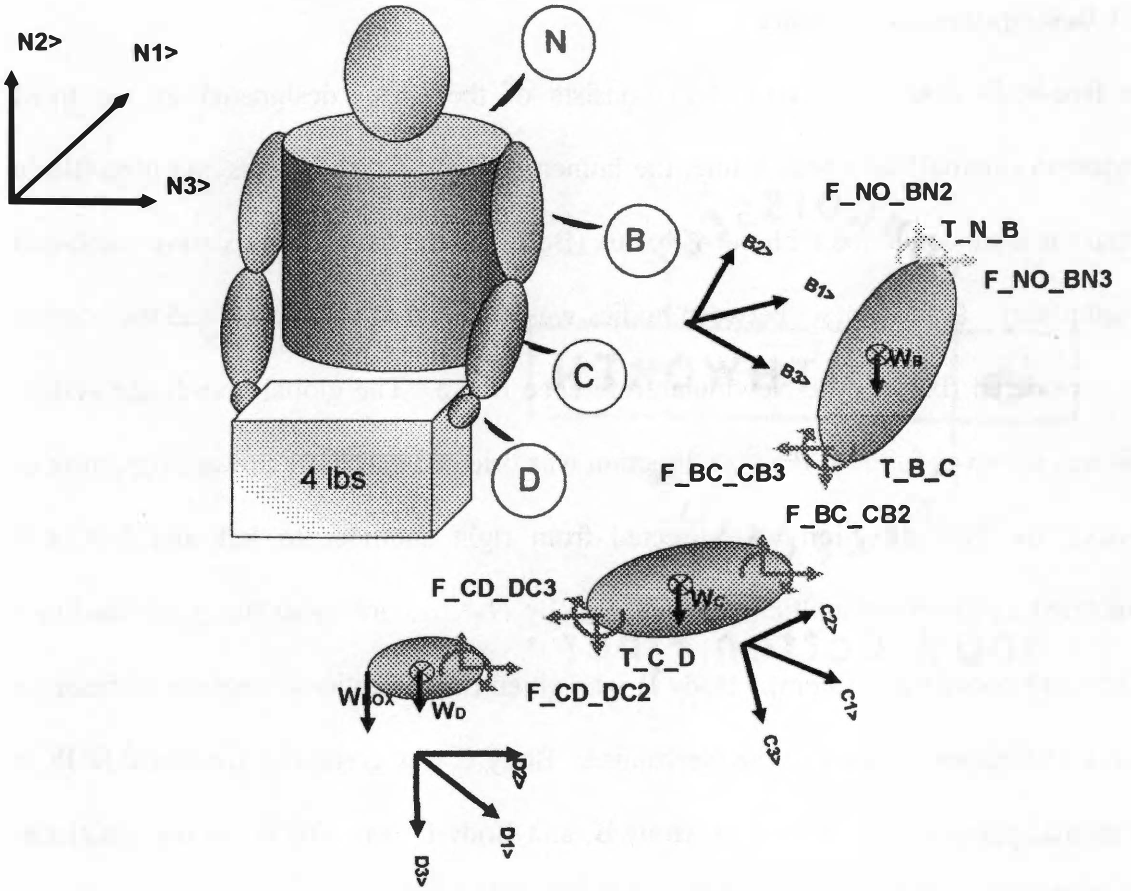

Figure 4-7: Simplified Free-Body Diagram Used in the Mathematical Model

the Newtonian space, a reference point, NO, was declared in N at the glenoid. The system represented an open chain from the scapula to the hand. At least three points were assigned to each body (including the center of mass) to define them in the N frame. Position vectors relating the points on each body to their respective CS were formulated, beginning with point 'NO' to the mating point, 'BN' on Body B, for example, moving through each adjacent point up to the hand.

Once the relative CS of each segment was related to N, the transformations describing the motion of each segment were input. The location of the geometrical center of the models used in the 2D-to-3D registration process does not coincide with the location of the CG of each body segment, as defined by the anthropometric data. Therefore, translation was neglected and only the relative rotations were entered. The rotations of Body B (humerus) were taken directly from the output of the 2D-to-3D registration process and input to the model. Since the bones corresponding to Bodies C and D were not overlaid in the registration process, their relative rotations were assumed as ten and five degrees, respectively. These assumptions are believed to be correct, since the majority of arm operation was managed by the humerus during the box lift. To ensure continuity of the transformation input up to second order (for acceleration terms), each of the rotations were curve-fit using 4th order local regression piecewise splines.

The model is invoked in Autolev™ and the equations of motion (appendix B) are solved for the unknown quantities. The model solved for fourteen unknowns – three forces and three torques at the shoulder, three forces and one torque at the elbow, followed by three forces and one torque at the wrist.

Chapter 5

Results

This chapter presents a comparison of the kinematic and kinetic results obtained for each shoulder group observed in this study. First, a comparison of rotational kinematics of the natural and implanted humerus is presented, and is preceded by data on the clinical outcome of the implanted patients and RCD patients used in this study. A comparison of loci tracking between groups is presented as an addendum to the kinematic data. This information is followed respectively by a comparison of joint forces and torques.

Due to the various sequences of rotations preferred by each patient performing the box-lift task as observed in the fluoroscopic data, and the time taken to complete the task, all kinematic data was input as a 1-2-3 sequence of rotations and standardized to a three-second duration. The rotation sequence is as follows: 1. ab-/adduction, 2. axial rotation, and 3. flexion/extension.

5.1 Clinical Results

For those with a replaced shoulder, average post-operative scores significantly improved ($p<0.05$), for example: American Shoulder & Elbow Score (ASES) = 74 [+44.4] (range: 60 to 83); SST = 7 [+5.3] (range: 6 to 8); Visual Analog Score (VAS) pain = 1 [-5.4] (range: 0 to 2); Active Forward Elevation (AFE)= 99° [+64] (range: 70° to 130°), and ER= 31° [+25] (range: 5° to 35°). ASI was eliminated and all no implant loosening or scapular notching was identified on X-rays. Custom RSA showed promise as a salvage procedure in complex shoulders with rotator cuff loss, ASI, and shoulder dysfunction. RSA provided stability, pain relief, and enabled patients to regain the ability to perform limited tasks.

5.2 Kinematics

5.2.1 Loci Tracking

All five normal patients experienced similar 3D motion patterns, with an average length of travel of 31.877 mm (range: 24.94489206to 39.20284134mm) in the frontal plane and 44.33810408 mm (range: 41.80846634 to 47.6631206 mm) in the sagittal plane, respectively (calculated by taking the sum of the average travel of all five points for a single shoulder group). RCD subjects experienced less overall motion than the normal subjects, averaging 39.68413238 mm (range: 33.99806228 to 43.21556675 mm) RSA subjects experienced the least amount of sagittal-plane motion. On average, they experienced 43.13383178 (range: 36.00628646to 49.27937898mm) of travel. TSA subjects experienced the most sagittal-plane motion with an average 47.02399946 mm (range: 40.89030425 to 51.12595795mm) of motion. This information is summarized in Table 5-1, below. Figures 5-1 through 5-12 display this data graphically.

5.2.2 Humeral Rotation Kinematics

Three rotational degrees of freedom were observed and recorded during the box-lift activity: abduction/adduction of the arm laterally away from or towards the body, axial rotation of the arm, and flexion/extension of the arm towards or away from the front of the body.

From the 2D-to-3D registration process it was determined that the normal subjects experienced an average arm abduction of 13.8° (range: 4.46° to 25.4°, SD: 4.187), external axial rotation of -15.7° (range: -31.7° to 6.18°, SD: 9.57), and an average flexion angle of -35.8° (range: -4.89° to -80.5°, SD: 29.0). RCD subjects experienced an average arm adduction of 15.1° (range: 23.5° to -0.324°, SD: 6.903), external axial rotation of 14.5° (range: 10.0° to 19.2°, SD: 3.0591), and an average flexion of 27.0° (range: 0.0614° to 43.4°, SD: 13.262). RSA subjects experienced an average arm abduction of 61.4° (range: 30.9° to 111°, SD: 30.238), internal axial rotation of -3.27° (range: -36.5° to -22.3°, SD: 2.504), and an average extension of 48.8° (range: 36.8° to 73.2°, SD: 11.117). TSA subjects experienced an average arm adduction of -3.88° (range: -9.10° to 1.12°, SD: 3.587), external axial rotation of 5.31° (range: 1.99° to 10.4°, SD: 2.099), and an average

Table 5-1: Average Travel of Humeral Loci with respect to the Glenoid

PLANE OF INTEREST		SUBJECT TYPE			
		NORMAL	RCD	RSA	TSA
		AMOUNT OF TRAVEL RELATIVE TO THE GLENOID (MM)			
FRONTAL					
MSP/MHP(REVERSE)		28.63023719	33.99806228	49.75319058	49.82931088
MLP		24.94489206	40.67088383	55.17650252	45.71697242
MMP		31.87887103	43.21556675	52.40535259	45.47322948
MPP		39.20284134	38.73408376	53.24112099	54.09911074
MAP		34.72636742	41.80206525	49.27937898	52.68764806
AVERAGE OVERALL TRAVEL		31.87664181	39.68413238	51.97110913	49.56125431
SAGITTAL					
MSP/MHP(REVERSE)		43.18612929	41.8248257	36.00628646	51.12595795
MLP		41.80846634	44.84841037	44.42479326	43.01181719
MMP		45.88754631	44.25333437	39.82881901	40.89030425
MPP		47.6631206	47.98215013	46.1298812	49.39504093
MAP		43.14525786	45.99395337	49.27937898	50.69687697
AVERAGE OVERALL TRAVEL		44.33810408	44.98053479	43.13383178	47.02399946

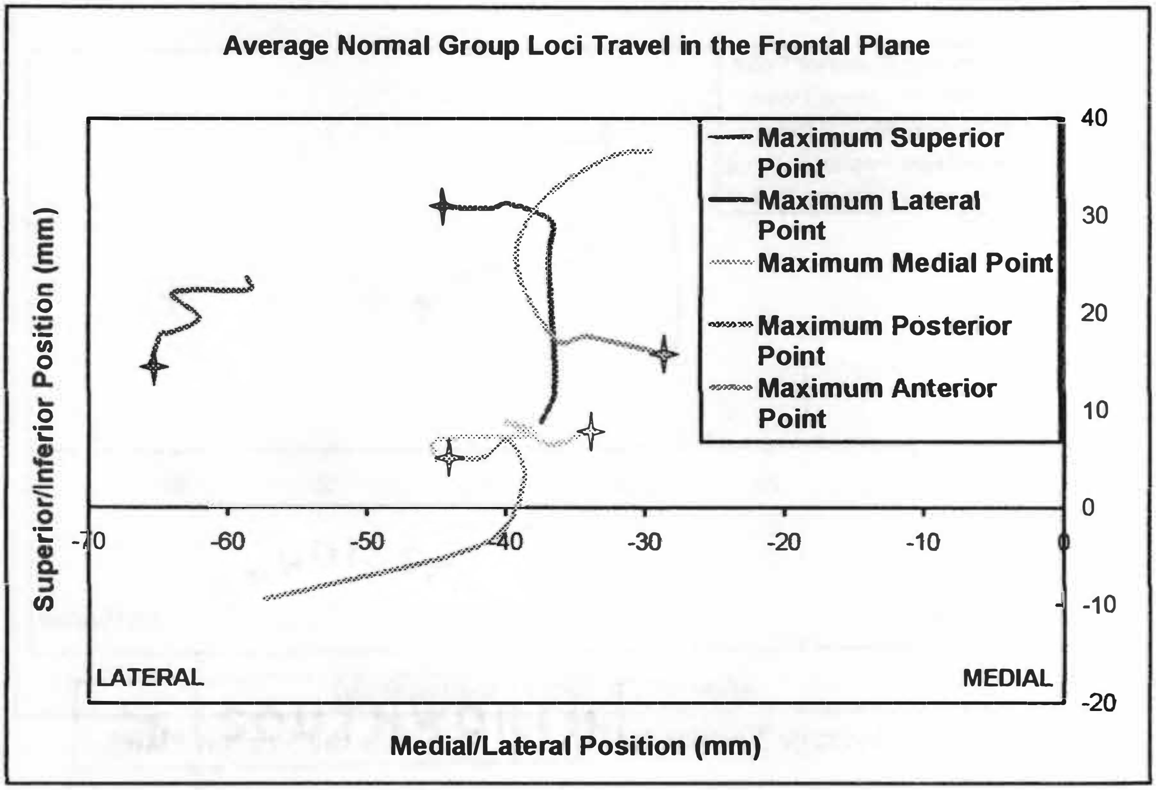

Figure 5-1: Average Normal Group Loci Travel in the Frontal Plane

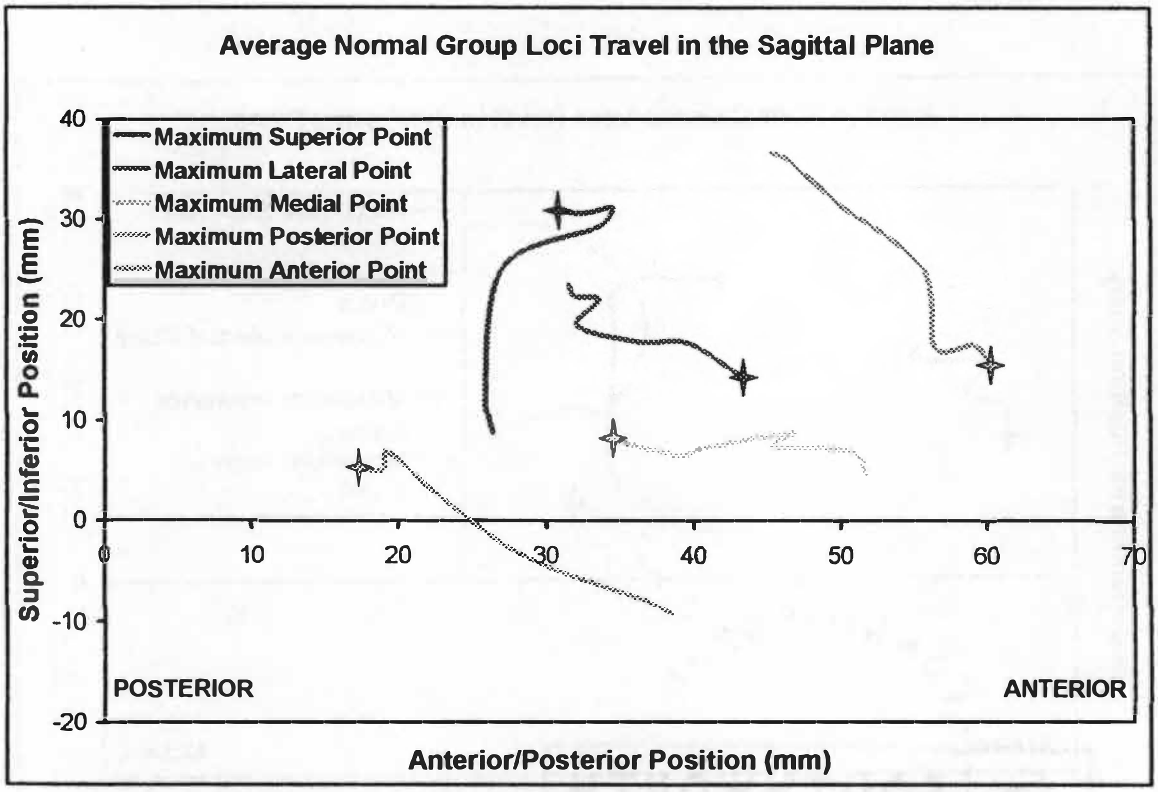

Figure 5-2: Average Normal Group Loci Travel in the Sagittal Plane

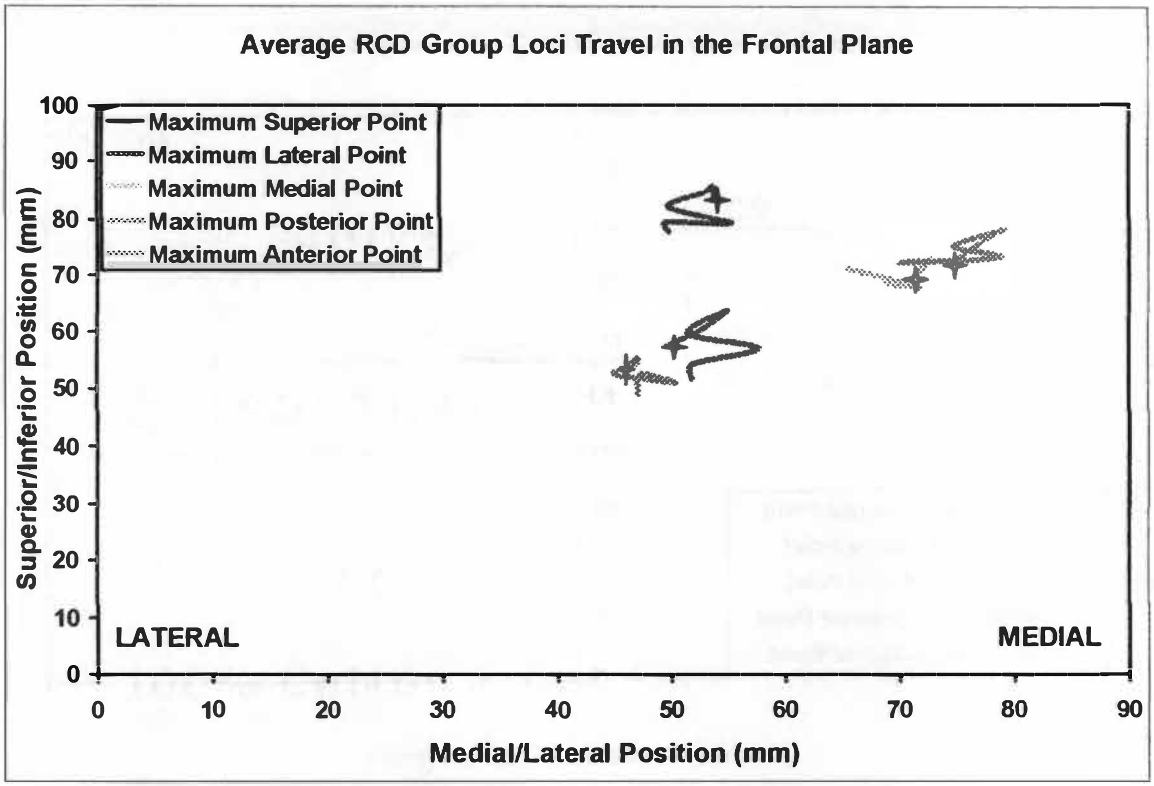

Figure 5-3: Average RCD Group Loci Travel in the Frontal Plane

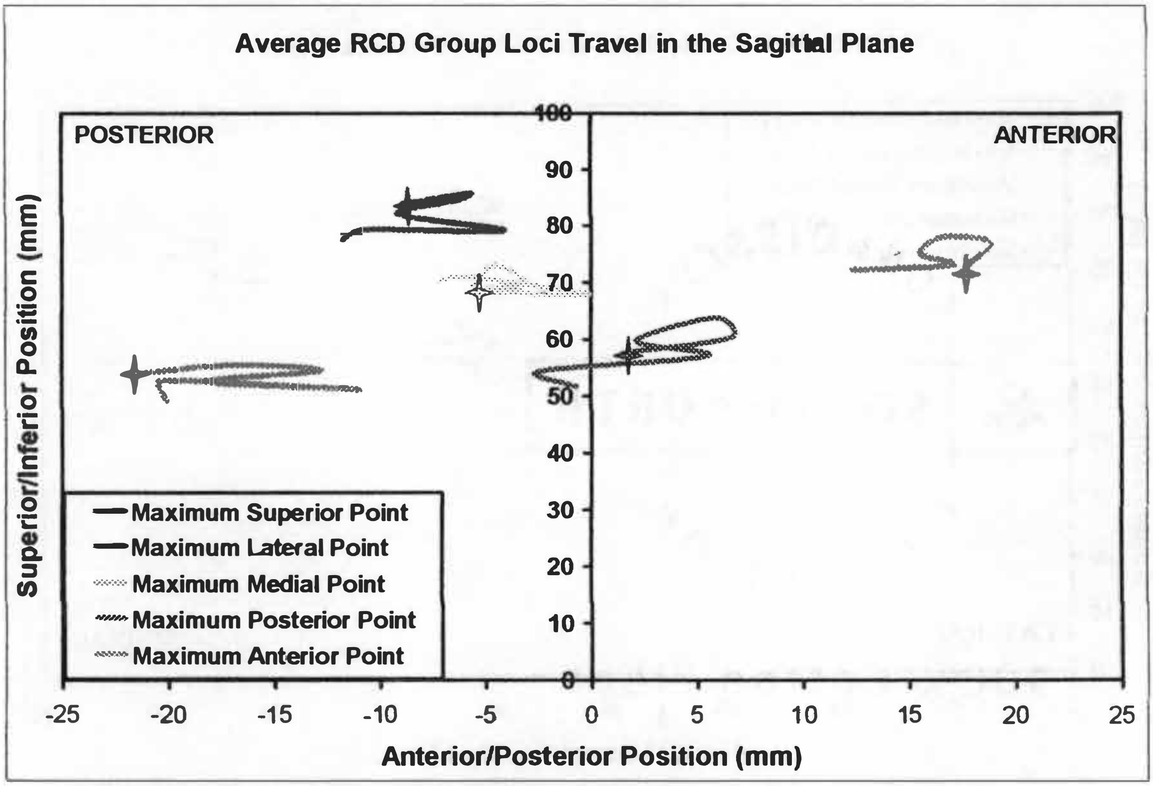

Figure 5-4: Average RCD Group Loci Travel in the Sagittal Plane

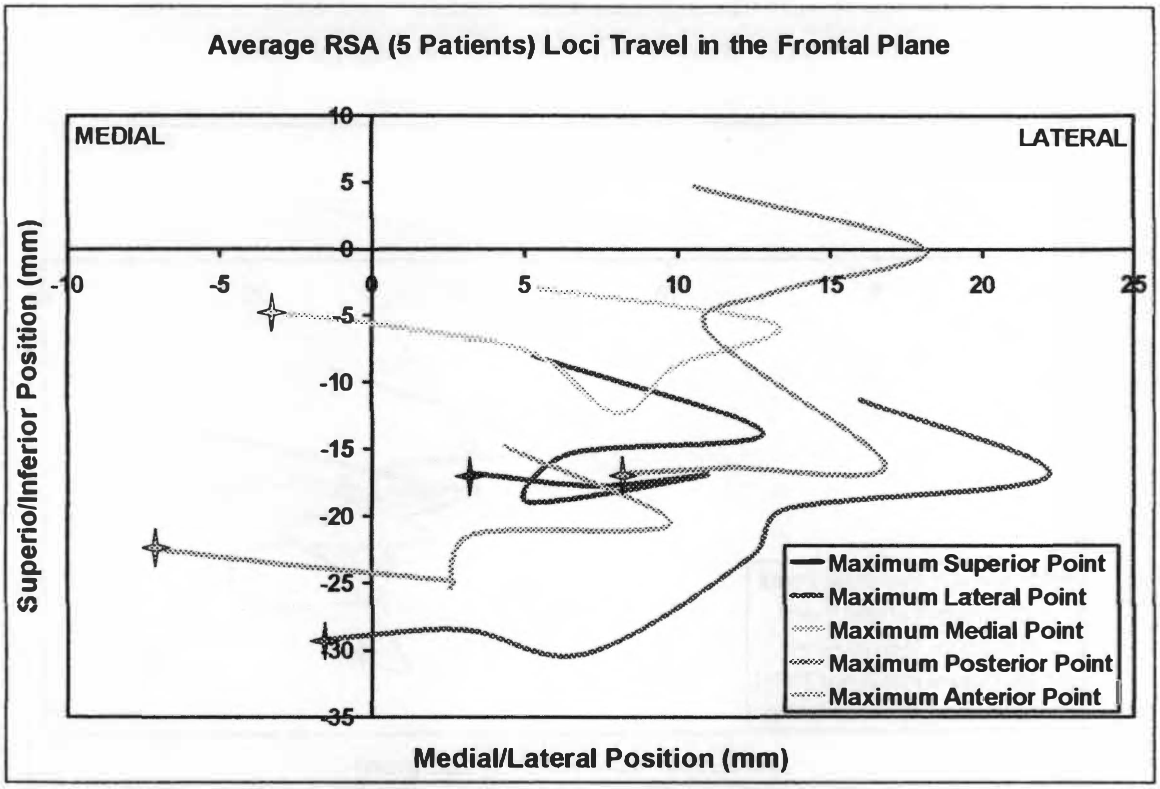

Figure 5-5: Average RSA (5 Patients) Loci Travel in the Frontal Plane

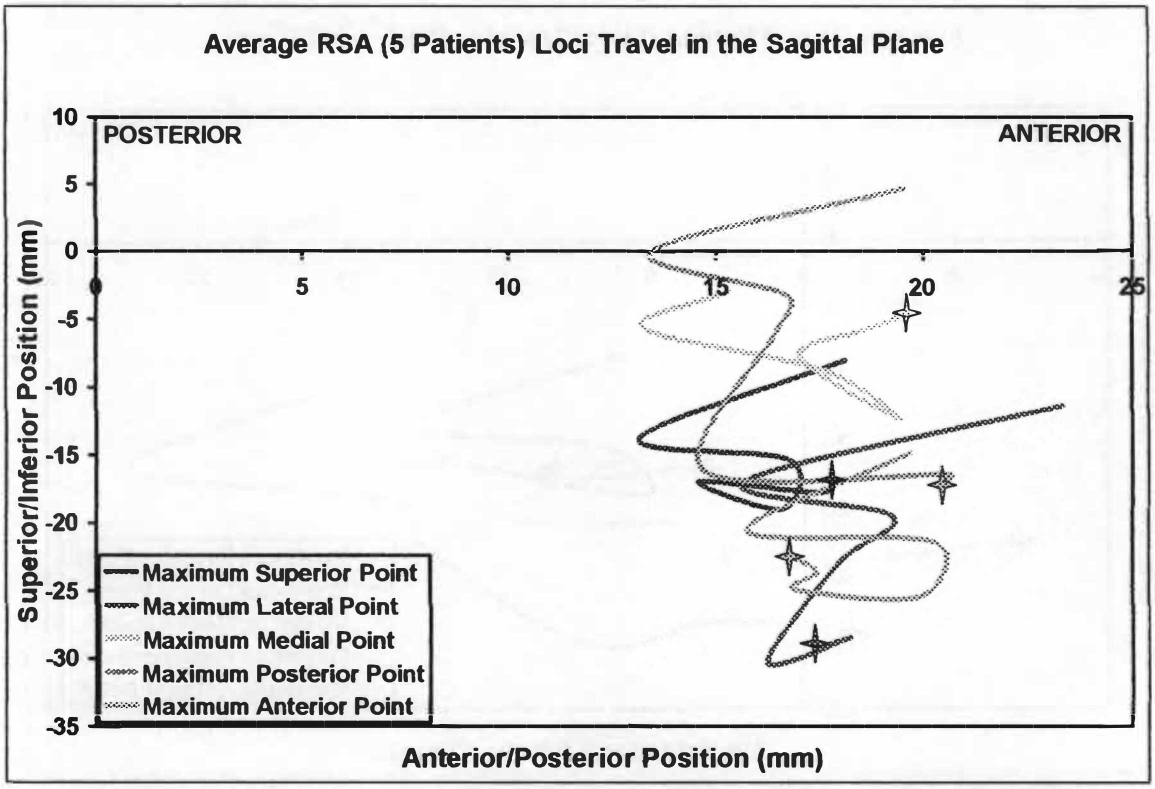

Figure 5-6: Average RSA (5 Patients) Loci Travel in the Sagittal Plane

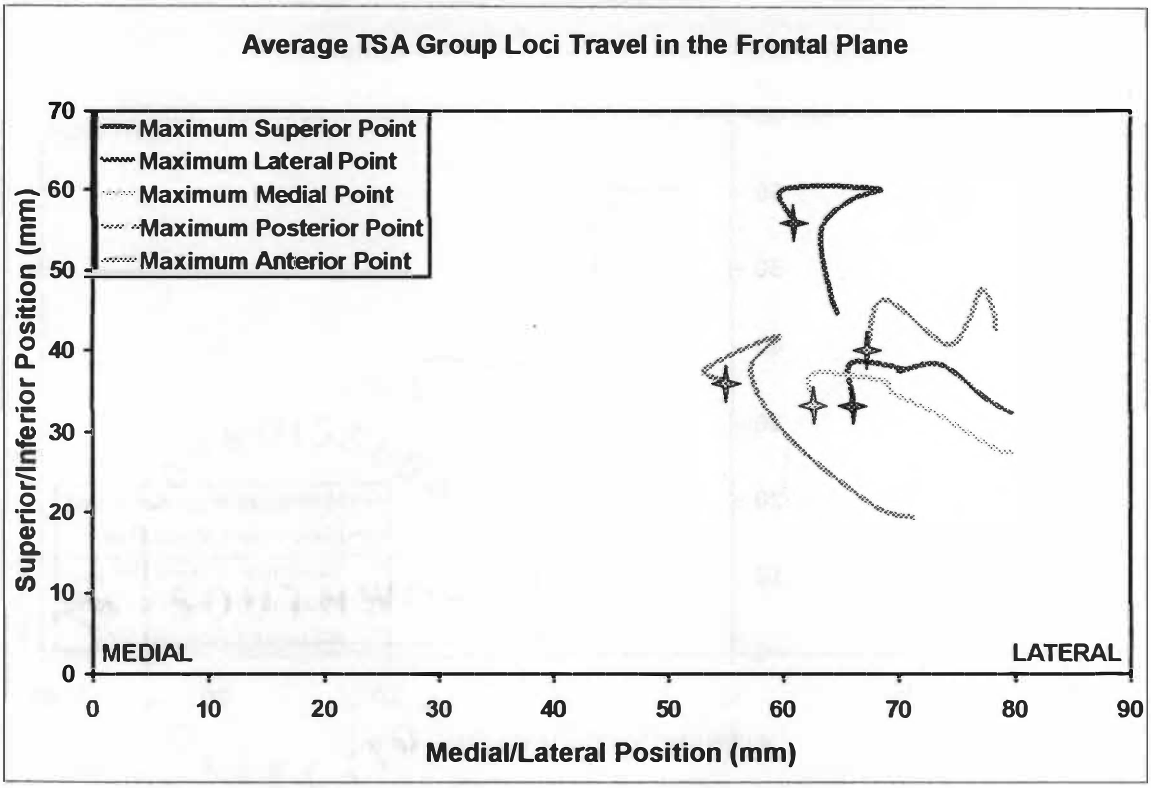

Figure 5-7: Average TSA Group Loci Travel in the Frontal Plane

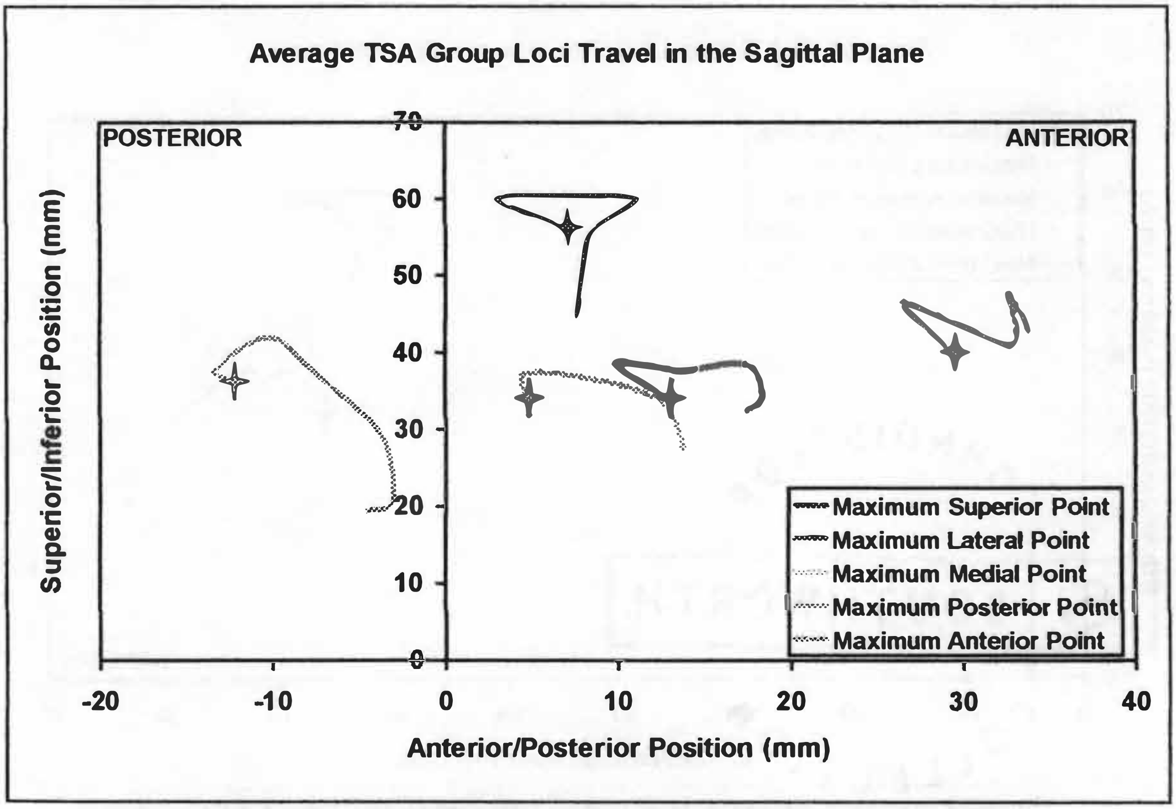

Figure 5-8: Average TSA Group Loci Travel in the Sagittal Plane

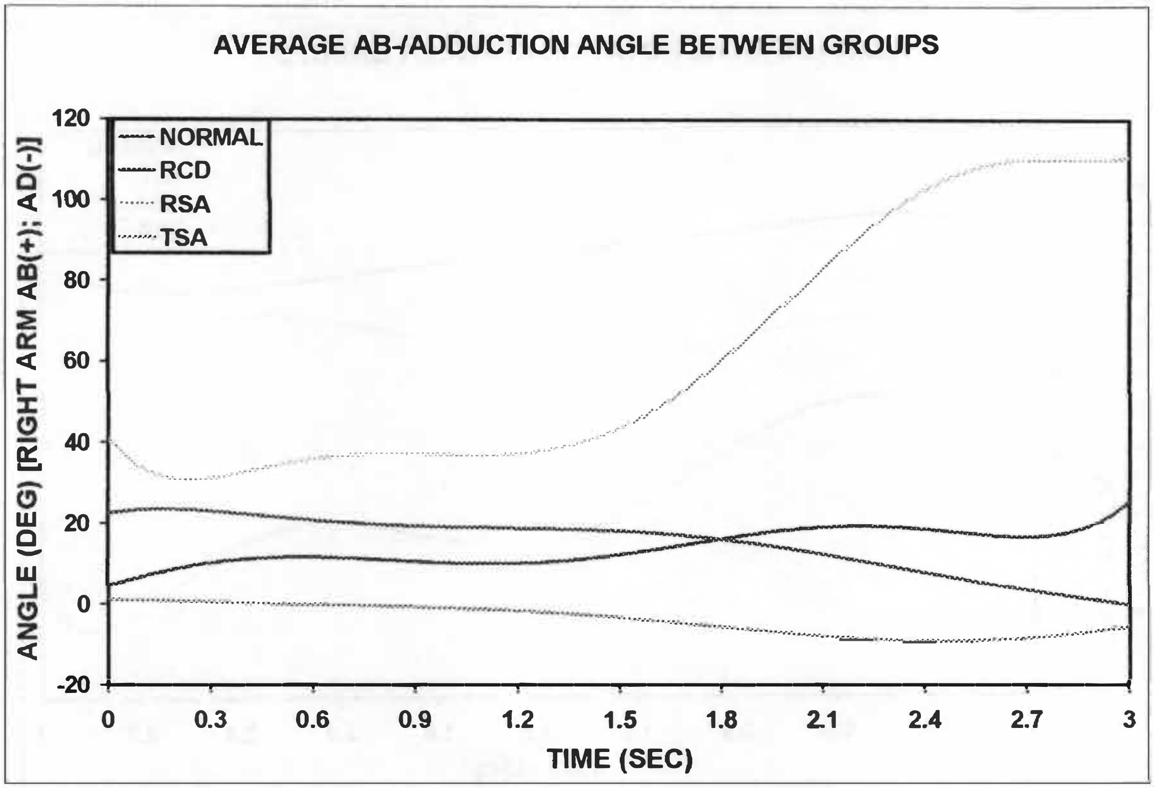

Figure 5-9: Average Abduction/Adduction Comparison Between Groups

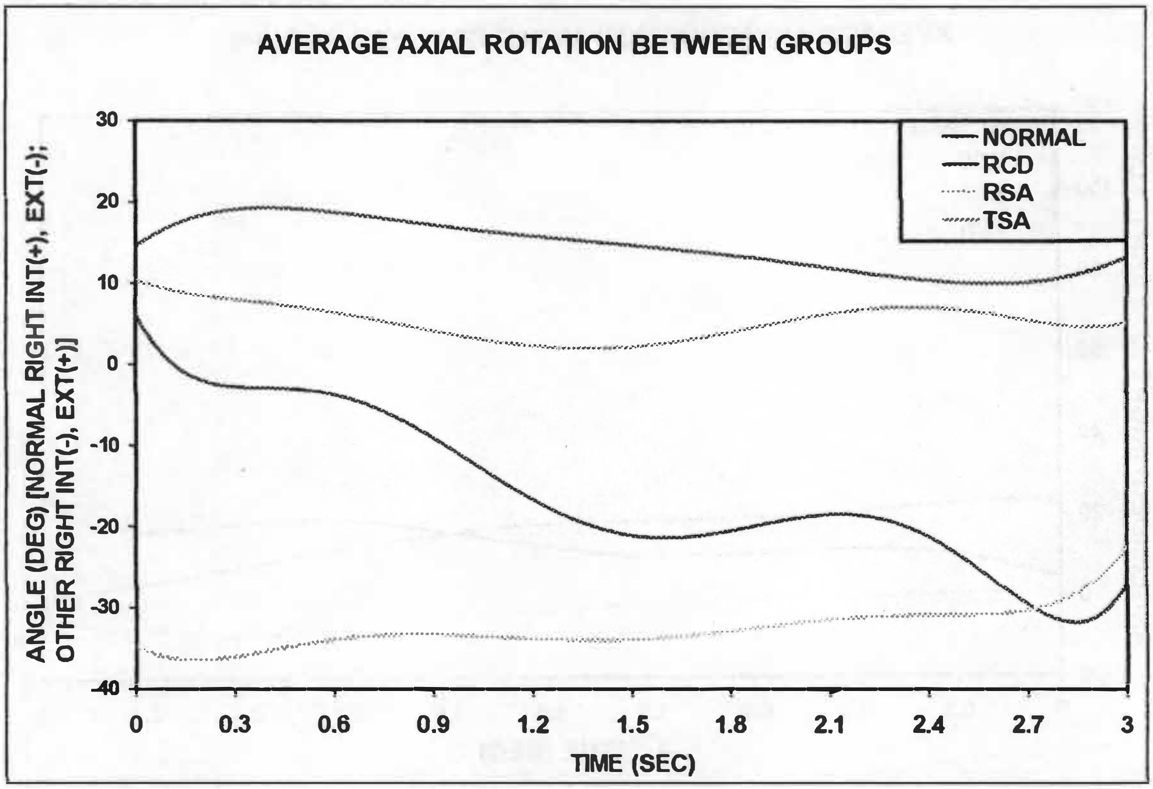

Figure 5-10: Average Axial Rotation Between Groups

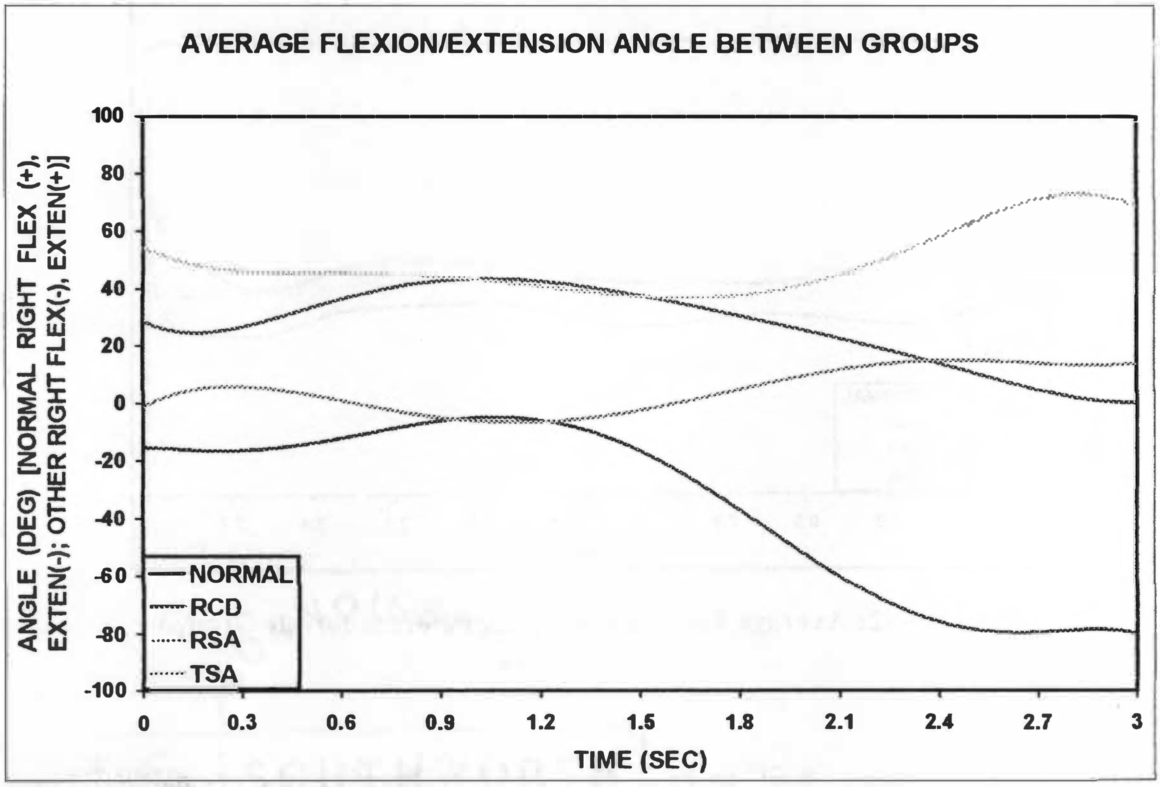

Figure 5-11: Average Flexion/Extension Angle Between Groups

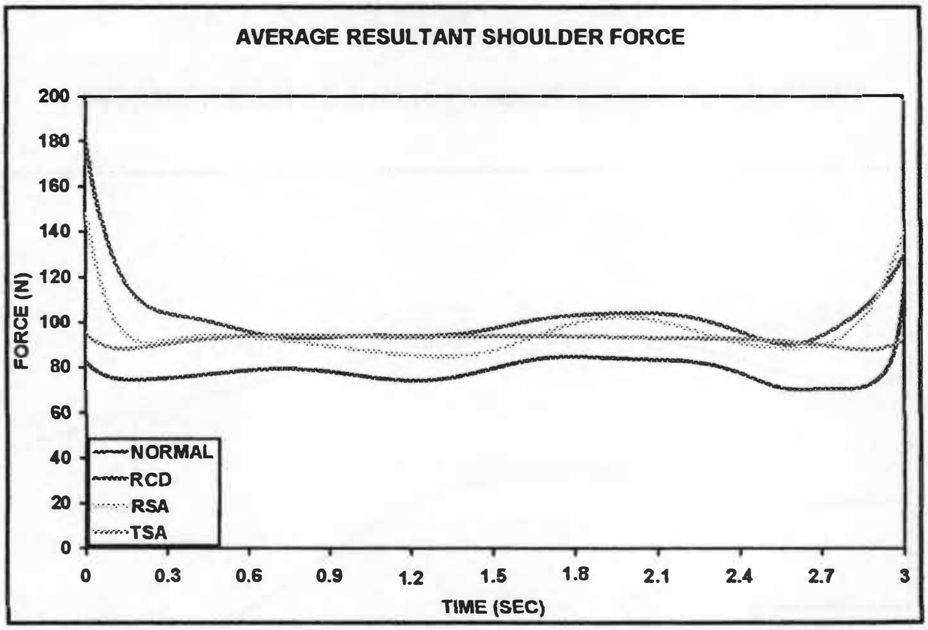

Figure 5-12: Average Resultant Shoulder Forces for all Groups

extension of 4.65° (range: -6.61° to 15.1°, SD: 7.567). Therefore, the normal, RCD and TSA subjects experienced similar motion patterns where the flexion rotation was greater than the adduction and external axial rotation, but the subjects having a RSA experienced adduction rotation as the dominant motion, with minimal internal and flexion rotation.

5.3 Kinetics – Resultant Joint Forces and Torques

Resultant joint forces were determined respectively for the shoulder, elbow and wrist for each patient during the standardized box-lift exercise. Average resultant joint forces were determined for each shoulder group and compared. The next subsections present the data for all four groups.

5.3.1 Resultant Forces

During the box lift, the normal subjects experienced average maximum resultant forces of 78.3N (range: 70.4N to 117N, SD: 5.213), 44.4N (range: 37.5N to 90.0N, SD: 5.193), and 23.9N (range: 18.8N to 60.7N, SD: 4.138) at the shoulder, elbow and wrist, respectively. RCD subjects experienced an average resultant force of 102N (range: 90.2N to 180.2N, SD: 12.339), 57.8N (range: 48.2N to 125N, SD: 10.779), and 30.8N (range: 24.2N to 77.4N, SD: 7.676). RSA subjects also experienced relatively higher average maximum joint forces of 94.9N (range: 84.9N to 149N, SD: 10.02), 52.1N (range: 43.7N to 95.3N, SD: 8.539), and 26.9N (range: 21.3N to 58.0N, SD: 6.008), respectively. Similarly, the TSA subjects experienced relatively high resultant joint forces of 92.5N (range: 87.984N to 95.370N, SD: 1.848), 51.2N (range: 47.7N to 54.973N, SD: 1.496), and 27N (range: 24.5N to 30.1N, SD: 1.083), respectively. Therefore, during the box lift the normal subjects experienced the least amount of forces at all three joints to perform the same task.

5.3.2 Resultant Torques

Normal subjects experienced average maximum resultant torques of 23.6Nm (range: 8.32Nm to 73.7Nm, SD: 11.227), -4.70Nm (range: -10.5Nm to 2.22Nm, SD: 4.123), and -0.853Nm (range: -4.00Nm to 3.46Nm, SD: 2.209) at the shoulder, elbow and wrist, respectively. RCD subjects experienced an average maximum resultant torques of

29.6Nm (range: 22.892Nm to 71.377Nm, SD: 7.581), 8.14Nm (range: 5.424Nm to 22.085Nm, SD: 2.100), and 5.03Nm (range: 3.189Nm to 14.490Nm, SD: 1.518). RSA subjects experienced average maximum resultant torques of 27.2Nm (range: 19.961Nm to 59.352Nm, SD: 6.664), 3.70Nm (range: 1.218Nm to 11.988Nm, SD: 1.427), and 0.620Nm (range: -1.064Nm to 3.502Nm, SD: 0.821), respectively. Finally, the TSA subjects experienced average maximum resultant torques of 20.3Nm (range: 11.700Nm to 31.409Nm, SD: 6.496), 3.99Nm (range: -0.679Nm to 5.702Nm, SD: 1.159), and 3.81Nm (range: 2.063Nm to 4.252Nm, SD: 0.389), respectively. Therefore, unlike the force results, subjects having a TSA shoulder experienced the least amount of torques at the three joints, with the normal subjects, on average, experiencing 3.3 Nm greater torque than the TSA subjects (Figure 5-13).

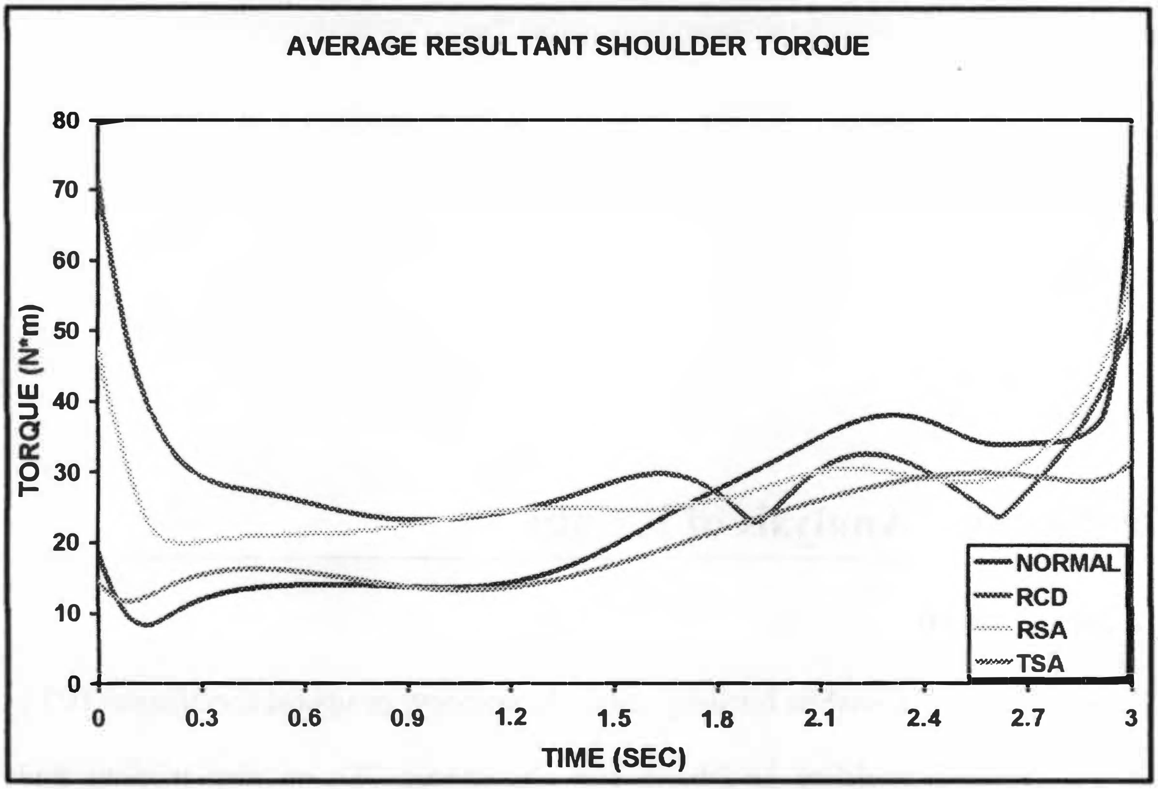

Figure 5-13: Average Resultant Shoulder Torque for all Groups

Chapter 6

Discussion – Analysis of Results

6.1 Introduction

This study presents a method for using x-ray fluoroscopy, computed tomography (CT), and mathematical modeling to obtain and characterize 3D, *in vivo* motions and forces/torques for implanted and non-implanted shoulders. The loci tracking used in this study provided a great amount of qualitative and quantitative data that effectively characterizes the 3D motion of the humeral head w.r.t. the glenoid. The mathematical code was compiled in FORTRAN and successfully solved for 14 unknowns: three forces and three torques at the shoulder, and three forces and one torque at both the elbow and wrist. To date, this is the first known study to use fluoroscopy, CT, and mathematical modeling to determine accurate *in vivo* forces and torques for both implanted and non-implanted shoulders.

6.2 Kinematics

6.2.1 Loci Tracking

Loci analysis was performed in the frontal and sagittal planes. The frontal plane was utilized to assess the amount of medial/lateral (M/L) motion of the humeral head w.r.t. the glenoid, while the sagittal plane was utilized to assess the amount of anterior/posterior (A/P) motion of the humeral head w.r.t. the glenoid. The superior/inferior (S/I) position of the humeral head could be readily obtained from either of the aforementioned views. From Table 1, we see that the RSA subjects averaged the greatest amount of frontal plane motion, tending toward an inferior and lateral position w.r.t. the glenoid, and maintaining approximately the same A/P position (Figures 5-5, 6). The subjects having a TSA showed the greatest amount of motion in the sagittal plane, beginning with a more posterior position of the humeral head, relative to the glenoid, and moving anteriorly. RCD subjects tended to remain localized relative to the glenoid space (Figures 5-3, 4).

Yamaguchi performed a radiographic analysis of symptomatic and asymptomatic shoulders with rotator cuff tears, and normal shoulders without rotator cuff tears (Yamaguchi 2000). Radiographs of each subject's shoulder were taken in thirty-degree increments of arm elevation in the scapular plane, from 0° to 150°. According to this study, the symptomatic and asymptomatic RCD groups showed progressive superior translation of the humeral head on the glenoid with increasing arm elevation, while the normal group, in contrast, maintained a constant center of rotation along the geometric center of the glenoid (Yamaguchi 2000). Qualitatively, the results of the current study and those of Yamaguchi appear to be consistent (Figure 5-1 thru 5-8). However, Yamaguchi shows a lower amount of average humeral shift in his symptomatic subjects than is observed in this study. At the beginning of his exercise, average translations start at almost zero, relative to the glenoid, and only reach approximately 1.7mm of shift by the end of the exercise. Our data shows almost 90mm of superior humeral shift and roughly 5mm of M/L shift in the frontal and sagittal planes. This may be explained by the fact that subjects in this study were asked to perform an activity that required use of the shoulder joint in more than one plane, coupled with the fact that there was a load applied at the hands. Also, the analysis in our study began once the subject picked up the box, causing contracture of the muscles and the large superior shift observed in the RCD subjects. Furthermore, differences could be attributed to his data lacking the effects of humeral shift out of the scapular plane.

Another study, by Eisenhart-Rothe, used MRI and CAD model re-creation to determine glenohumeral kinematics of subjects with traumatic and atraumatic shoulder instability (2002). Here the subjects were placed lying down in an open MRI unit (Figure 6-1). Passive elevation (abduction) of the arm was conducted at 30° and 90°, in combination with external rotation of the arm, and later coupled with muscle activity. CAD models were used to set up a glenoid-based coordinate system used to track the humeral head

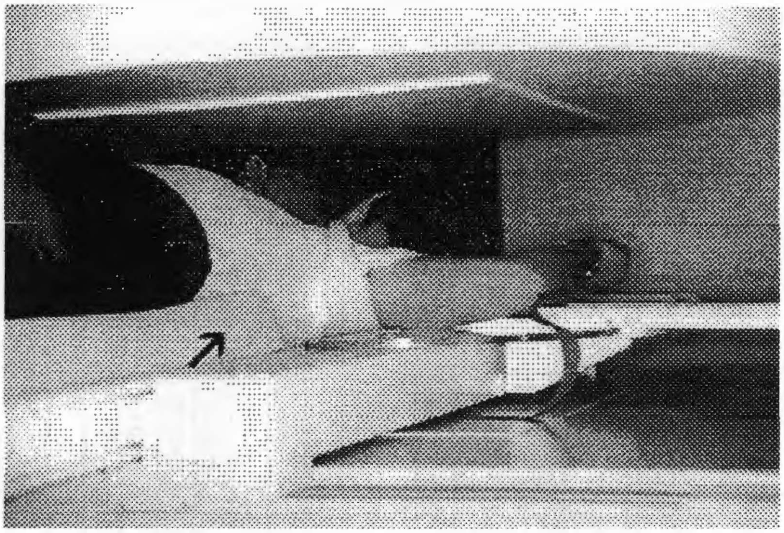

Figure 6-1: Example of MRI Activity [Adapted from Eisenhert-Rothe 2002]

during each activity. Results from this study show that glenohumeral motion was maximized when the arm was abducted at 90° with maximum external rotation. According to his results, subjects with traumatic instability experienced average maximum anterior and inferior shifts of 3.0 ± 1.1mm and 1.7 ± 1.5mm, respectively. The data retrieved in our study exceeds these magnitudes, which may be attributed to out-of-plane loading conditions and subject physique (i.e., many of the implanted and RCD subjects weighed in excess of 200 lbs. and presented with excessive tissue on the arms).

6.2.2 Humeral Kinematics

On average, RSA subjects performed the box lift using a greater amount of arm abduction than did the other three groups, who tended to remain adducted (Table 6-1).

Table 6-1: Humeral Kinematics

	SHOULDER TYPE					
	NORMAL			RCD		
ROTATION	***AVERAGE MAGNITUDE OF ROTATION (IN DEGREES)***					
AB/ADDUCTION (A)	13.8342836			15.09658		
IN/EXTERNAL ROTATION (B)	-15.668118			14.53928		
FLEXION/EXTENSION (C)	-35.814205			27.0057		
	(A)	(B)	(C)	(A)	(B)	(C)
STDEV	4.18698002	9.57141987	29.0001835	6.903425	3.059072	13.26198
MIN	4.45618	-31.731552	-80.4928	-0.3239	10.00393	0.061389
MAX	25.40176	6.17896	-4.890886	23.46733	19.22701	43.40205
	RSA			TSA		
ROTATION						
AB/ADDUCTION (A)	61.4345088			-3.88076		
IN/EXTERNAL ROTATION (B)	-32.656874			5.309572		
FLEXION/EXTENSION (C)	48.7662531			4.647043		
	(A)	(B)	(C)	(A)	(B)	(C)
STDEV	30.2376533	2.50381035	11.1172706	3.587251	2.099215	7.566887
MIN	30.877132	-36.460644	36.75133	-9.10258	1.99087	-6.61159
MAX	110.83762	-22.3306	73.216796	1.1225	10.44628	15.05708

The greater amount of abduction among RSA subjects is possibly due to disruption of the rotator cuff muscles during surgery, requiring subjects to use compensatory motions to lift the box. However, RSA subjects four and five were fluoroscoped using a table fluoroscopy unit that restricted the forward elevation of their arms. This was done because these particular subjects were not fluoroscoped at the same time as the others, and the table fluoroscope was the only one available at the scheduled time. So, these subjects held a stick between their hands to simulate the box lift and maintain an equal distance between their hands. This fact may have had the greatest impact on RSA abduction kinematics. TSA subjects averaged the least amount of abduction. In fact, their primary means of lifting the box appeared in the fluoroscopic data (Figure 6-2) to be extension of the humerus and lower arm, while keeping the elbow adducted. The normal subjects showed a greater ability to rotate their arm to lift the box, tending toward an external rotation.

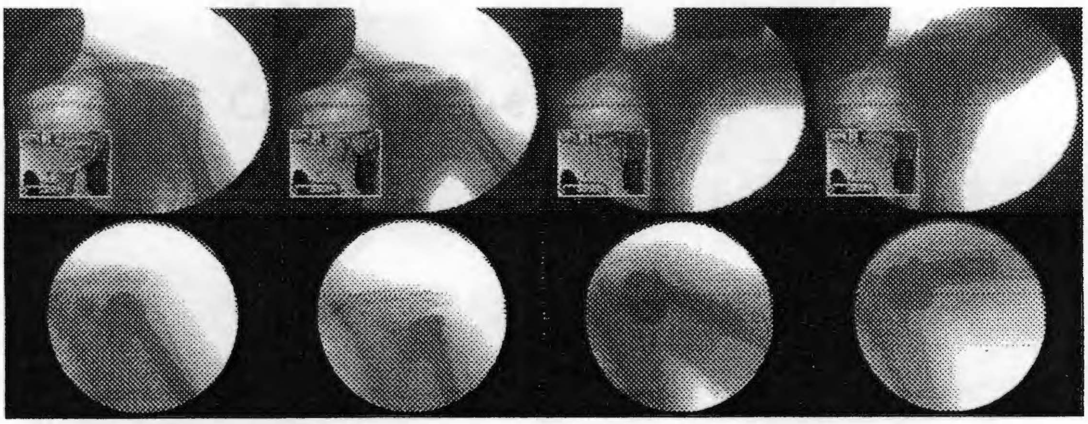

Figure 6-2: Comparison of Normal (Top) and TSA (Bottom) Box Lift

In addition, the RCD subjects showed the least amount of axial rotation of the humerus but had a tendency to externally rotate their arm. In comparison to the other subjects, the RCD group presented great evidence of their shoulder impairment by tending to bend at the waist and slowly lean forward while trying to lift the box. This was identified in the fluoroscopic video as a darkening of the arm nearing the end of the box lift, an indication that the arm had come closer to the X-Ray source (Figure 6-3). This compensatory motion was used instead of keeping their shoulder blade flush with the fluoroscope image intensifier (as prescribed by the activity protocol). Overall, the normal, RCD, and TSA subjects tended to externally rotate their humerus, while the RSA group tended to internally rotate, abduct, and flex their humerus to perform the lift.

The normal subjects were also able to exercise a greater amount of arm extension. The other three groups tended to keep the arm flexed. Furthermore, TSA subjects showed the

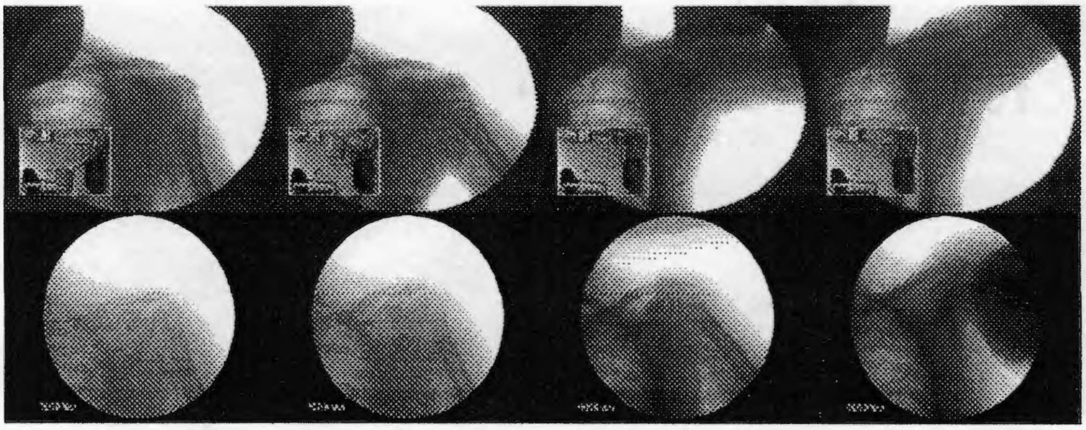

Figure 6-3: Comparison of Normal (Top) and RCD (Bottom) Box Lift Motion

least amount of arm extension, according to the registration process. This was due to the assumed humeral head offset angles during TSA component assembly for 2D-to-3D registration which caused a slight mismatch in the overlays and introduced *some* error into the kinematic results. Thus, these findings suggest that the RCD, RSA and TSA subjects relied mainly on compensatory motions to lift the box on top of the fluoroscopy unit (Figure 6-4).

6.3 Kinetics

6.3.1 Joint Forces

In this study, the mathematical model predicted that normal shoulder joint forces increased (approximately 80N) as the box was lifted from full-arm extension. Interestingly, the resultant forces for the RCD and RSA groups started with magnitudes almost two times higher than the normal subjects at the start of the lift exercise. Force magnitudes decreased abruptly from start of the lift to ten percent of the lift and remained

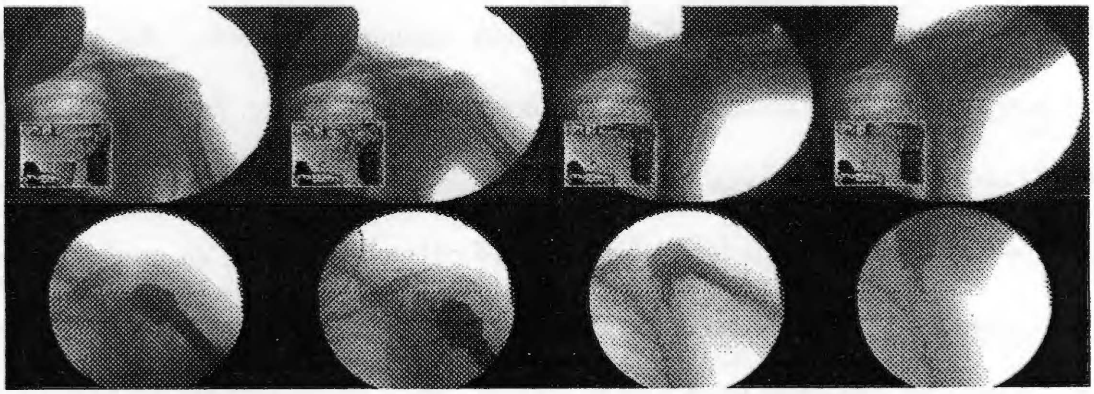

Figure 6-4: Comparison of Normal (Top) and RSA (Bottom) Box Lift Motion

steady throughout the majority of the lift cycle. The forces increased again at ninety percent of the motion cycle. This seems counter-intuitive, as one would tend to think that a rotator cuff tear combined with osteoarthritis would greatly decrease the muscle strength required to produce such results – and likewise for the RSA subjects with regard to soft-tissue balancing during surgery, considering that these subjects underwent multiple surgeries before receiving a reverse arthroplasty. The cause for such results may can attributed to the amount and direction of humeral head distraction in the RCD shoulders mimicking shoulder impingement syndrome, coupled with the fact that contact between arm segments is modeled by point contact, rather than surface contact. Therefore the distributed load at the shoulder is not observed. For both the RCD and RSA subjects, another factor influencing the results could be an increased amount of adipose tissue on the arms– thus adding to their arm segment weights.

Resultant joint forces for TSA subjects began and remained approximately 10N greater than those for the normal subjects. However, the trend changed as the resultant forces for the normal subjects increased to their higher, peak magnitude just before the end of the lift. Upon further review of this data, it was noted that each subject having a TSA joint experienced fairly constant force magnitudes throughout the motion activity (Figures 6-5 through 6-8). When comparing the kinematic data for the normal and TSA groups, we see that the magnitude of arm abduction and version between the groups appears similar. However, the TSA subjects achieved a lesser degree of arm extension than did the normal

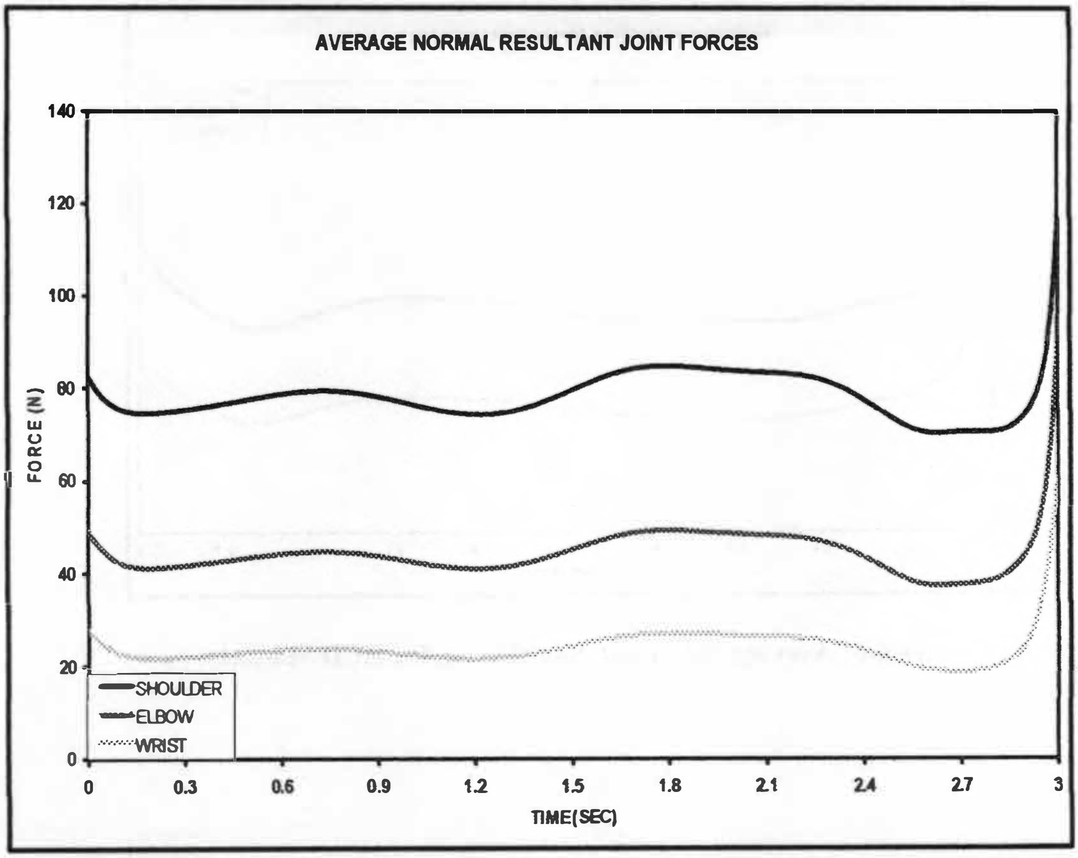

Figure 6-5: Average Resultant Joint Forces for Normal Shoulder Subjects

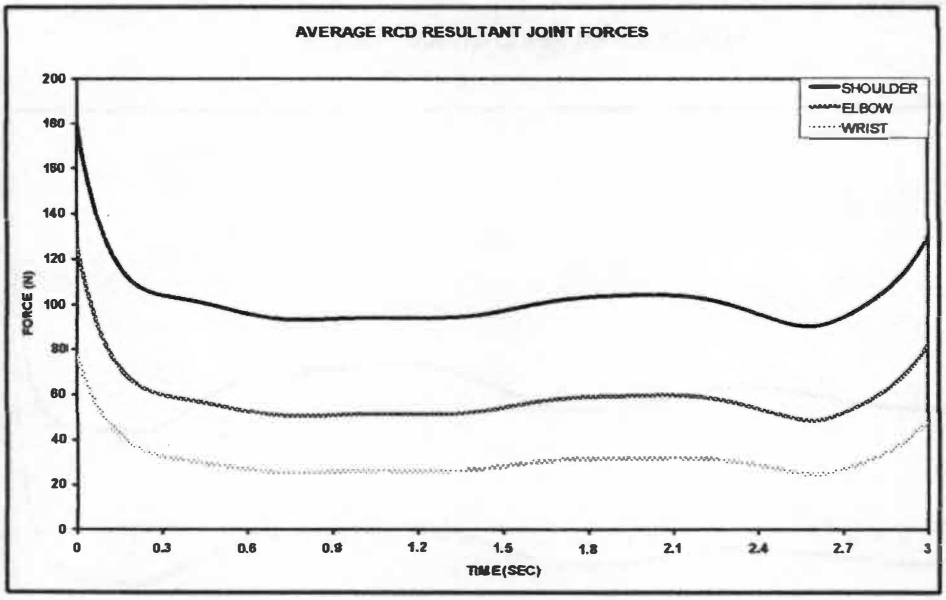

Figure 6-6: Average Resultant Joint Forces for RCD Subjects

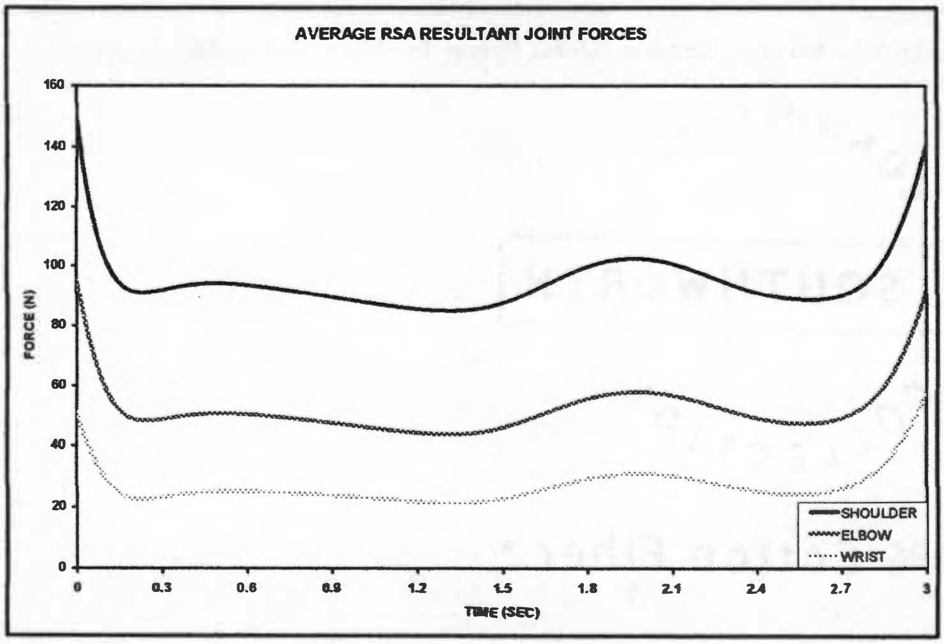

Figure 6-7: Average Resultant Joint Forces for RSA Subjects

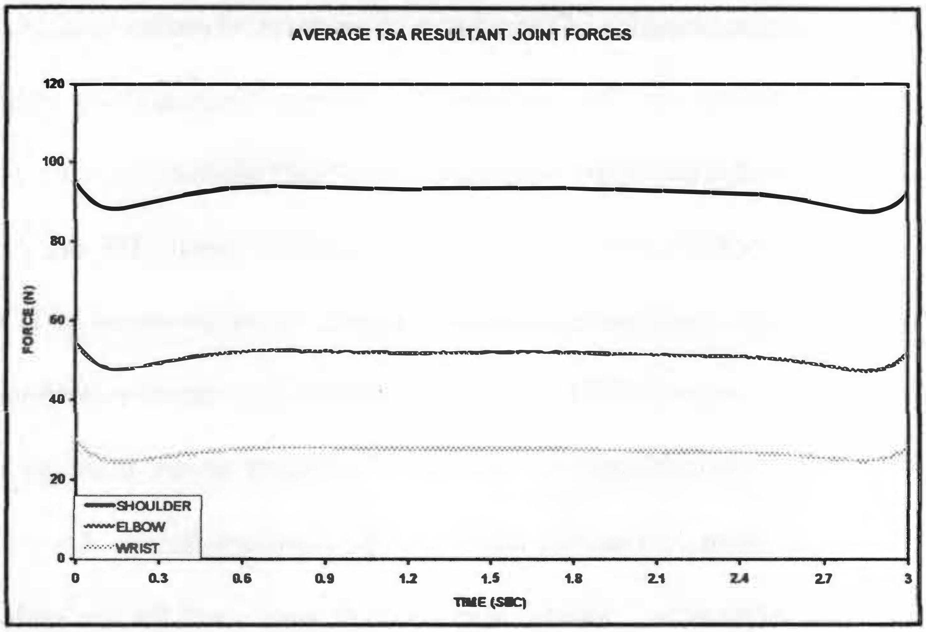

Figure 6-8: Average Resultant Joint Forces for TSA Subjects

subjects. We noted earlier that maximum joint forces for the normal, RCD, and RSA subjects came at maximum arm extension. Thus, there may be a correlation between the lower resultant joint forces and the decreased amount of arm extension seen in the TSA subjects, as compared to the other groups.

Murray and Johnson (2004) conducted a study where the objective was to establish a database of upper limb kinematics and kinetics for use in a mathematical model of the shoulder and elbow. They used cameras and skin markers to track the motion of ten healthy (average age: 34 yrs.) male subjects performing ten everyday tasks, one of which was lifting an object to head height, from the seated position. While our lift activity required a slightly higher elevation of the arms, a comparison of results is still valid. For the lift activity, Johnson and Murray used an inverse Newton-Euler optimization algorithm that predicted a maximum longitudinal (vertical) force of 51.5 N. However, from their presentation of data, it is unknown at what phase of the lift this occurred. Our model on the other hand predicted approximate resultant shoulder forces of 117 N, 180 N, 148 N, and 95 N for normal, RCD, RSA, and TSA subjects, respectively (Figure 5-12, Figure 6-2, 6-3, 6-4, 6-5) (Although we caluculated resultant forces, it should be noted that the vertical component the resultant forces was the dominant factor). Several reasons may explain these differences. Firstly, skin markers were used for the collection of kinematic data in the Murray study (2004), therefore increasing the error, as compared to our 2D-to-3D registration process. Secondly, the weight of the object the subjects lifted is unknown, and, thirdly, no information was provided regarding the inclusion of limb weight on the resulting kinetics.

Parsons, *et al.* (2002) determined the effects of multiple rotator cuff tear types on fourteen cadaveric upper extremities in abduction (raising the arm in the scapular plane). It is important to remember that the rotator cuff serves two principle functions for the glenohumeral joint: generate torque for humeral rotation and compress the humeral head into the glenoid cavity (Parsons 2002). In light of this, Parsons found that, by simulating a full-thickness tear in both the supraspinatus (SS) and infraspinatus (IS) muscles, glenohumeral joint reaction forces were significantly reduced, compared to the cadaveric shoulders used in his study without any damage to the rotator cuff. In the SS/IS tear condition, the arm was raised using a 5N force, and the normal shoulders were raised at a rate of 20 N/s after using an initial force of 5N to center the humeral head in the glenoid. The maximum shoulder force for the SS/IS simulation was 149 $\pm$ 15N at a maximum abduction angle of 41 $\pm$ 11°, and 337 $\pm$ 88 N at 85 $\pm$ 10° of maximum abduction, for the normal case. In our study, it was found that the maximum average resultant shoulder force for RCD subjects was 102N (range: 90.2N to 180.2N, SD: 12.339). Furthermore, the maximum force of 180.2 N occurred at the beginning of our box-lift activity, where the average RCD abduction angle was at a maximum. The discrepancy between these results arises from the fact that, in the Parsons study, the forces measured were due to muscles resisting arm abduction, whereas in our study, the forces obtained are a good estimate of the forces in the muscles used to produce the motion. While these studies differ in their methodology and the activity tested, their results give credibility to the importance of the rotator cuff in maintaining stability of the shoulder joint.

Favre, *et al.* (2005) recently performed a study in which an iterative algorithm was developed to determine shoulder muscle forces that would equilibrate the upper extremity for twelve arm positions experiencing arbitrary loads. The purpose in his attempt was to create the basis for a model that could adapt to various arm positions and external loads and predict muscle loads. In his study, Favre divides the main muscles of the shoulder (including the rotator cuff, pectoralis, deltoid, and latissimus muscles) into twenty-seven segments and simulates them in his model as ropes of varying thickness, depending on their physical attributes. The actions studied include abduction/adduction, internal/external rotation, and anterior/posterior humeral flexion. A 9Nm torque was applied to the shoulder, simulating a 15N load applied to an outstretched hand, and the reaction force in each muscle segment was determined. His results ranged between 200N and 642N, for adduction and internal [axial] rotation of the arm, respectively. These results are high, in comparison to ours, in which the largest resultant shoulder force of 180.2N was experience by an RCD subject.

Due to differences in methodology and physical parameters used in this and the Favre study, it is difficult to make direct comparison. However, the author believes that the results determined in the Favre study as well as several others involving cadaveric specimen and/or optimization techniques have tended to overestimate their resultant shoulder joint forces, and therefore, believes that the present method holds an advantage over them (Komistek 2005). For instance, Favre's algorithm interprets the load applied at the hands, and recruits certain muscles to resist the load and perform the required abduction, flexion, or arm rotation task. The error here, is that possible protagonist/antagonist stabilizing muscles are neglected from action and the algorithm shows that the muscles called upon are carrying a load greater than the actual load (Komistek 2005, Labriola 2005). Also, the setup described in the Favre study is cumbersome with regard to test rig complexity. The use of fluoroscopy and mathematical modeling, as described in this thesis, is advantageous, in that the results are obtained *in vivo*, and the contact forces obtained by the model are a good estimate to the load being carried by each of the muscles maintaining the joint. Therefore, the cumbersome calculation of individual muscle forces in an attempt to describe shoulder joint loading is eliminated. Furthermore, the external load applied and the activity of interest can be varied in the computational model as desired. Therefore, the model presented in this thesis can be adapted to analyze various, clinically relevant, configurations and loading conditions.

6.3.2 Joint Torques

Joint torques in this study were expressed in a fashion similar to the resultant joint forces. With the exception of the Normal and TSA shoulders, the RSA and RCD groups experienced greatly increased torque magnitudes during the start and end of the box lift sequence. With regard to the RCD subjects, this trend was driven, in part, by Subject #3. This particular subject's model of the lift was driven by the largest among RCD subject rotations, and resulted in the highest forces and torques observed in the RCD group. For instance, RCD subject #3 abducted his arm approximately 160° from his side, maintained an axial rotation angle of approximately 80°, and flexed his arm almost 150°. RSA subjects had the next highest average shoulder torque, at 27.2Nm. From the data it is difficult to say whether or not one or more subjects are primarily responsible, as each has a widely variable torque pattern at each joint. However, RSA Subject #2 had the most expressive abduction and flexion kinematics, owing to the larger joint torques among RSA subjects. Interestingly, the Normal and TSA subjects exhibited almost identical resultant torque profiles – especially at the shoulder. However, their difference in magnitude makes them distinguishable, as they differed by a magnitude of approximately 40Nm at the end of the lift activity (Figures 6-9 and 6-10). And, again, it is indicative of those groups having higher torque magnitudes, that compensatory motions were required to lift the box.

Although it is difficult to assess the accuracy of the present model in predicting shoulder torques by referring to literature, there are some interesting trends from literature which give credibility to the nature of the results observed in this study. For instance, Murray and Johnson predicted maximum moments during flexion/extension of the arm. The largest moment was predicted for shoulder flexion, and reached approximately 15 Nm. Interestingly, the largest rotation they measured was approximately 120° of shoulder flexion. Similar trends were found in our data, as the larger torques were consistent with the larger rotations observed (Figures 5-9 – 5-11, 5-13).

Williams *et al.* found that for TSA subjects, malrotation (offset) of the humeral head by 4-, 6-, and 8- mm in the S/I and A/P directions, simulating subacromial impingement, has a significant effect on glenohumeral joint torque (Williams 2000). They noticed that as

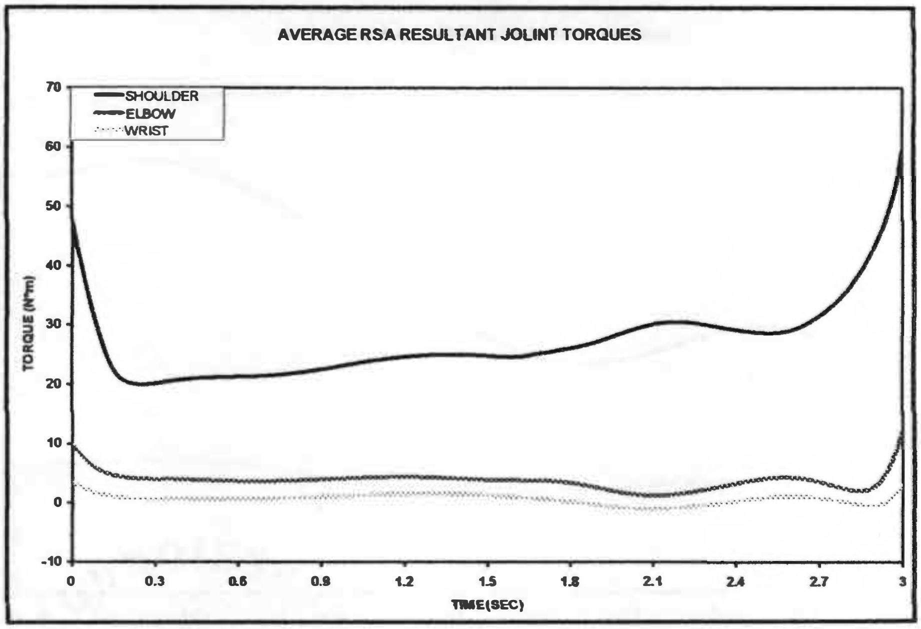

Figure 6-9: Average Resultant Joint Torques for RSA Subjects

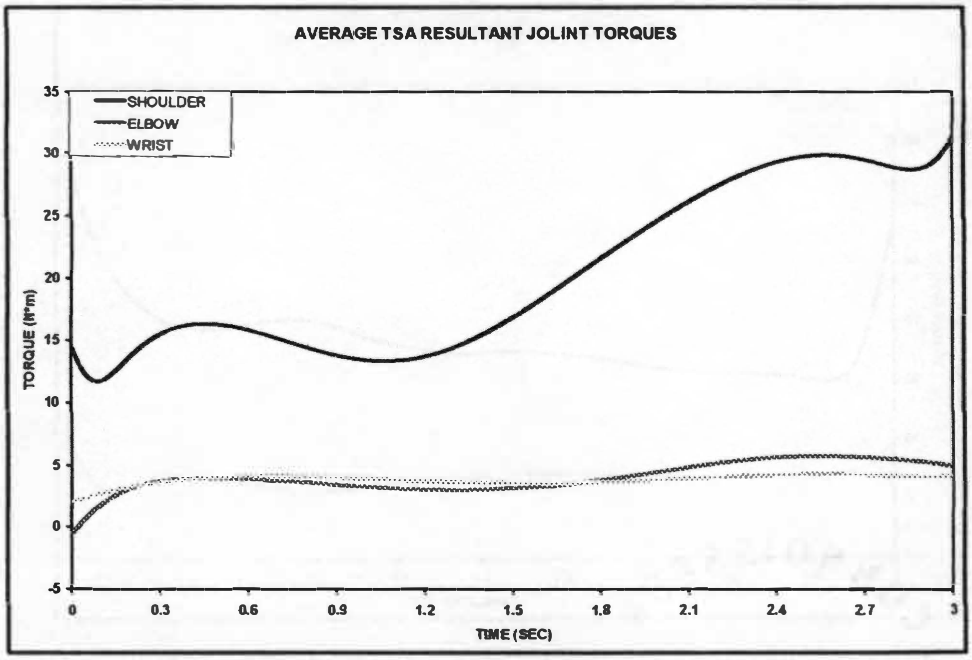

Figure 6-10: Average Resultant Joint Torques for TSA Subjects

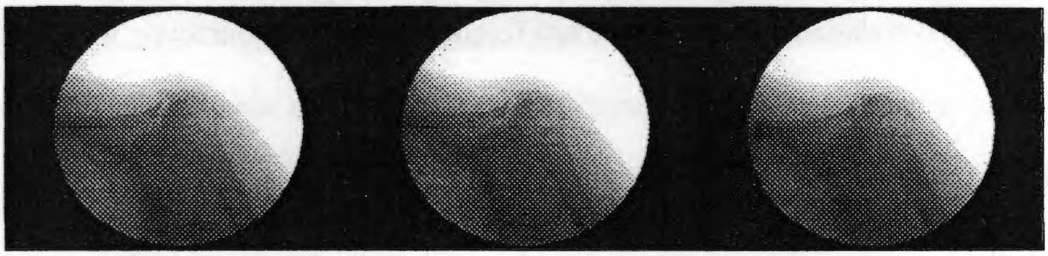

Figure 6-11: Example of RCD Shoulder Separation and Closure

little as 4mm of inferior offset causes significant subacromial contact, and an increase in shoulder joint torque. This could explain the high torque magnitudes observed in the RCD and TSA subjects, who showed considerable joint laxity between loading times (just before and just after initiating the box-lift exercise) (Figure 6-11).

Also, a comparison of torque magnitudes is not possible here, due to the difference in loading conditions in the Williams study and ours. Their test setup was limited to a 1.5 Nm torque, while ours was expected to be much greater and variable, depending on subject inertial properties and the weight of the box lifted.

Praggman (2000) used two quasi-static computational model types to correlate shoulder joint contact (compressive) forces to net joint torques about the shoulder. According to the results, there was high a correlation (> 0.90) between the two models. Review of his data shows that joint forces and torques have similar magnitude patterns, suggesting, as he says, that the total compressive joint forces are linearly related to the net joint torques.

A quantitative correlation between forces and torques predicted in our study was not one of the goals, however, the Pragmaan study does provide us with some certainty that their may be a possible linear correlation in our data, based on the trends observed in Figures 5-12 and 5-13.

6.4 Conclusions

This is the first documented study in which fluoroscopy, CT and mathematical modeling have been used to determine and analyze *in* vivo kinematics and kinetics of the shoulder. From this study we have learned that not only are there differences in the kinematics and kinetics between shoulder types, but also between those of individual members of a particular shoulder group. Normal shoulder kinematics suggests that the box lift can be completed successfully by order of abducting, externally rotating, and extending the arm. The data showed that abduction and adduction, as well as flexion and extension should be the largest motions among the three kinds. Subjects who utilized excessive arm ab-/adduction and axial rotation, as compared to ab/adduction combined with flexion/extension to successfully lift the box to its resting location were considered to have used compensatory motions. Such occurrences were obvious when comparing fluoroscopic data (Figures 6-1 thru 6-3) among the shoulder groups. Despite the somewhat large variations among groups and group members, there are two trends that may be concluded from this study.

1. There is a distinct correlation between the magnitude of joint forces/torques observed and the magnitude of the kinematics of each subject. Furthermore, the expression of the kinematics during the lift directly affects the expression of the forces and torques. For example, in the TSA subjects, the larger the arm abduction, the greater the resultant shoulder forces and torques.

2. No individual performs the box lift in the exact same way. However, subjects of a particular group may tend to perform the activity in a *similar* fashion (see appendix A). This may be due to the fact that all surgeries were performed by the same surgeon and technique, with regard to the implanted subjects.

Chapter 7

Study Limitations and Future Work

7.1 Limitations

There were six major limitations during this study:

At the beginning of the study, it was our intention to have twenty patients; however, during the CT scans, data for one patient was inadvertently copied over that of a TSA patient. Therefore, the study was left with four TSA patients instead of five, for a total of nineteen participants in the study population.

With regard to patient overlays, there were insufficient surgical operation notes to describe the rotation of the head on the humeral stem for the TSA patients. The omitted data included key information, because the CAD implant components must be assembled beforehand in order to create overlays for the TSA patients. Therefore, not knowing the orientation of the head on the stem from the fluoroscopy, I had to estimate the match from fluoroscopy. To address this issue, the TSA implants were segmented from CT to re-create 3D surface models to make the best approximation of the offset of the head. After overlays were completed for all groups and the data was compared, it became apparent that having to estimate the true offset of the humeral head introduced error into the kinematic calculations for the TSA patients. Furthermore, the induced error from the mismatch was not quantified and it's effect on the accuracy of the TSA kinetics was not assessed – but the effects were *not* so extreme that the kinematic and kinetic data for the TSA group could not be compared to the others in this study.

In addition, one of the RCD subjects adducted his arm during the CT scan, causing a shift in the bone density data. As a result, the CAD model of his bone had to be manually reconstructed. The reconstruction introduced a slight lump two inches below the anatomical neck, but it did not cause error in the overlay process.

Metal artifact reduction (MAR) had to be performed on all CT scans of implanted patients. After using the MATLAB program to execute the MAR, the segmented scapula models required a significant amount of surface smoothing, as compared with the other (Normal and RCD) segmented bone models. Quality overlays were created, but the smoothing may have increased the likelihood of error in the fit.

The math model involved three bodies: the humerus, the lower arm, and the hand/box entity. The overlays provided only humeral kinematics. Therefore, I made the assumption of a maximum ten degrees of relative rotation to describe the rotation of the lower arm with respect to the humerus. A maximum of five degrees of relative rotation was assumed for the hand with respect to the lower arm. The assumptions worked for the purposes of executing the mathematical model and validating the results, but it is believed that the inclusion of true lower-arm kinematics into the model would give different and more accurate results.

Another limitation in the model was the assumption of point contact between arm segments as opposed to bearing surface contact. Although the resultant forces at these points are a good estimation of what occurs, bearing surface forces would be more accurate.

7.2 Implications for Future Research

I attempted to determine the axode, or center of rotation (Figure 7-1), for each patient using a special algorithm created by Mahfouz (2003) that calculates the helical axis for the knee, hip, and spine. The results were promising; however, the algorithm has not yet been validated for the shoulder. The benefit of this information is that it is a clear, graphical representation of *in vivo* kinematics, and its use has possible clinical application

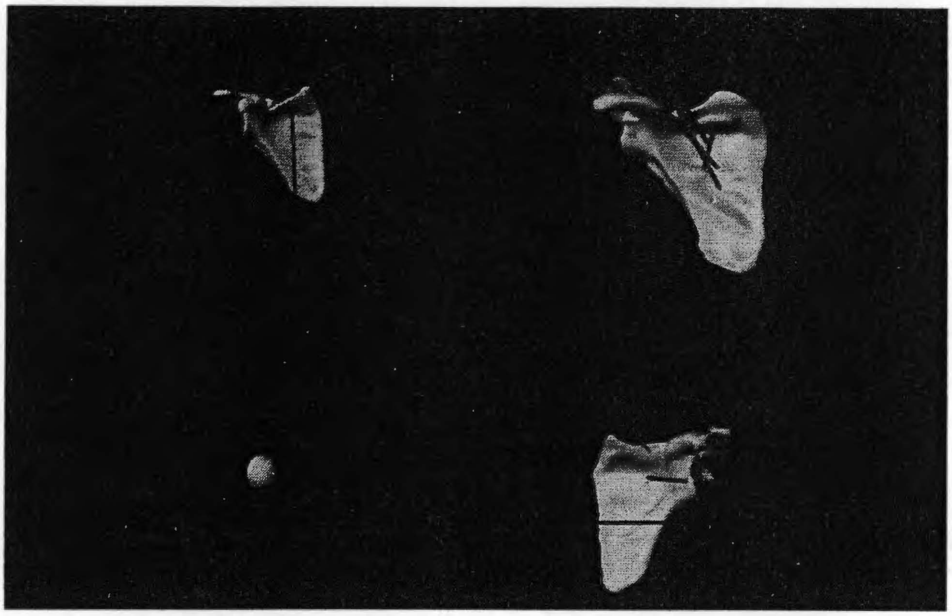

Figure 7-1: Example of Axode Determination for Normal (Top Left), RCD (Top Right), TSA (Bottom Right), and RSA (Bottom Left)

in providing a standard outcome upon which to base optimal surgical outcomes.

Also, future use of the loci tracking method might include determining the correlation between the direction and amount of motion with the phase of the activity being analyzed. Finally, the math model should be modified to include specific muscles and surface contact in order to perform a more accurate calculation of bearing surface forces. It should also include friction and sliding at the joints. Calculating the *in vivo* kinematics of the lower arm and hand in a similar manner as the humerus would also improve the accuracy of the model.

References

References – Publications

1. Alexander EJ, Andriacchi TP, 2001: "*Correcting for Deformation in Skin-Based Marker Systems.*" Journal of Biomechanics 34, 355-361.

2. Andriacchi TP, Alexander EJ, 2000: "*Studies of Human Locomotion: Past, Present and Future.*" Journal of Biomechanics 33, 1217-1224.

3. Borstad JD Ludewig PM, 2002: "*Comparison of Scapular Kinematics Between Elevation and Lowering of the Arm in the Scapular Plane.*" Clinical Biomechanics 17, 650-659.

4. Bull *et al.*, 2005: "*A Novel Technique to Measure Active Tendon Forces: Application to the Subscapularis Tendon.*" Knee Surg Sports Traumatol Arthrosc 13, 145-150.

5. deLeva P, 1996: "*Adjustments to Zatsiorski-Seluyanov's Segment Inertial Parameters*". Journal of Biomechanics 29, 1223-1230.

6. Dennis DA, *et al.*, 2003: "*Multicenter Determination of In Vivo Kinematics After Total Knee Arthroplasty.*" Clinical Orthopaedics and Related Research 416, 37-57.

7. Eisenhart-Rothe RMO *et al.*, 2002: "*Relevance of Arm Position and Muscle Activity on Three-Dimensional Glenohumeral Translation in Patients with Traumatic and Atraumatic Shoulder Instability.*" American Orthopaedic Society for Sports Medicine.

8. Favre *et al.*, 2005: "*An Algorithm for Estimation of Shoulder Muscle Forces for Clinical Use.*" Clinical Biomechanics. *Article in press.*

9. Fuller J, *et al.*, 1997: "*A Comparison of Lower-Extremity Skeletal Kinematics Measured Using Skin- and Pin-Mounted Markers.*" Human Movement Science 16, 219-242

10. Huston RL, 1990: "*Multibody Dynamics*". Butterworth-Heinemann, Stoneham, MA.

11. Kane, T.R. and Levinson D.A, 1985: "*Dynamics: Theory and applications*". McGraw-Hill, New York

12. Kelkar R, Wang VM, Flatow EL, Newton PM, Ateshian GA, Bigliani LU, Pawluk RJ, Mow VC, 2001: "*Glenohumeral Mechanics: A Study of Articular Geometry, Contact, and Kinematics.*" Journal of Shoulder and Elbow Surgery 10, 73-84.

13. Komistek RD, Stiehl JB, Dennis DA, 1998: "*Mathematical Model of the Lower Extremity Joint Reaction Forces using Kane's Method of Dynamics*". Journal of Biomechanics 31, 185-189.

14. Komistek RD, *et al.*, 2005: "*Knee Mechanics: A Review of Past and Present Techniques to Determine In Vivo Loads.*" Journal of Biomechanics 38, 215-228.

15. Labriola *et al.*, 2005: "*Stability and Instability of the Glenohumeral Joint: The Role of Shoulder Joint Muscles.*" Journal of Shoulder and Elbow Surgery 14,32S-38S.

16. Mahfouz MR, Hoff WA, Komistek RD, Dennis DA, 2003: "*A Robust Method for Registration of Three-Dimensional Knee Implant Models to Two-Dimensional Fluoroscopy Images*". IEEE Transactions on Medical Imaging 22(12), 1561-1574.

17. McClure *et al.*, 2001: "*Direct 3-Dimensional Measurement of Scapular Kinematics During Dynamic Movements In Vivo*." Journal of Shoulder and Elbow Surgery 10, 269-277.

18. Murray IA, Johnson GR, 2004: "*A Study of the External Forces and Moments at the Shoulder and Elbow While Performing Everyday Tasks*." Clinical Biomechanics 19, 586-594.

19. Parsons *et al.*, 2002: "*The Effect of Rotator Cuff Tears on Reaction Forces at the Glenohumeral Joint*." Journal of Orthopaedic Research 20, 439-446.

20. Piazza SJ, Delp SL, 2001: "*Three-Dimensional Dynamic Simulation of Total Knee Replacement Motion during a Step-Up Task*". Journal of Biomechanical Engineering 123, 599-606

21. Praagman M, Stokdijk M, Veeger HEJ, Visser B, 2000: "*Predicting Mechanical Load of the Glenohumeral Joint, Using Net Joint Moments*." Cinical Biomechanics 15, 315-321.

22. Rhoad *et al.*, 1998: "*A New In Vivo Technique for Three-Dimensional Shoulder Kinematics Analysis*." Skeleatal Radiology 27, 92-97.

23. Sallay PI, Reed L, 2003: "*The Measurement of Normative American Shoulder and Elbow Surgeons Scores*." Journal of Shoulder and Elbow Surgery 12, 622-627.

25. Williams *et al.*, 2001: "*The Effect of Articular Malposition After Total Shoulder Arthroplasty on Glenohumeral Translations, Range of Motion, and Subacromial Impingement.*" Journal of Shoulder and Elbow Surgery 10, 399-409

26. Yamaguchi *et al.*, 2000: "*Glenohumeral Motion in Patients with Rotator Cuff Tears: A Comparison of Asymptomatic and Symptomatic Shoulders.*" Journal of Shoulder and Elbow Surgery 9, 6-11.

References – Websites

1. The Medical Multimedia Group:
   http://www.medicalmultimediagroup.com/pated/joints/shoulder/

Appendices

Appendix A

Appendix A provides the average kinematics obtained from the 2D-to-3D registration process for each group

Normal Subjects

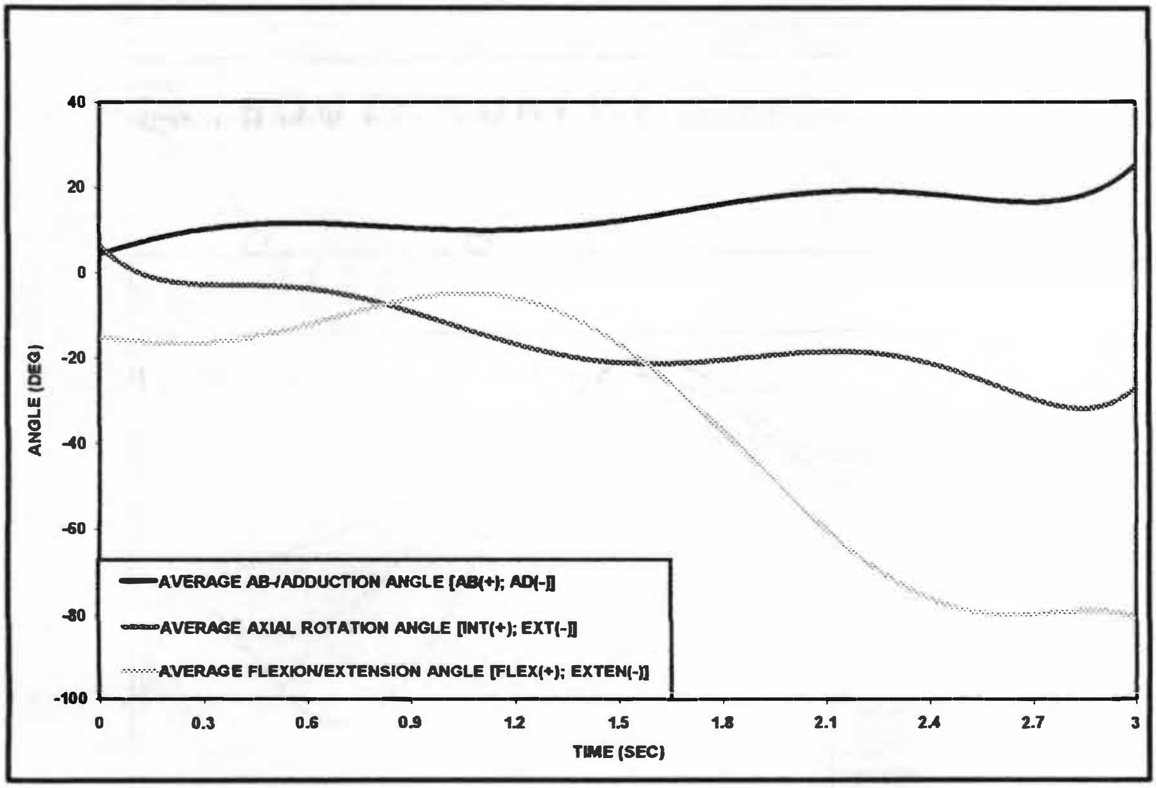

Figure A-1: Average Humeral Rotations for Normal Subjects

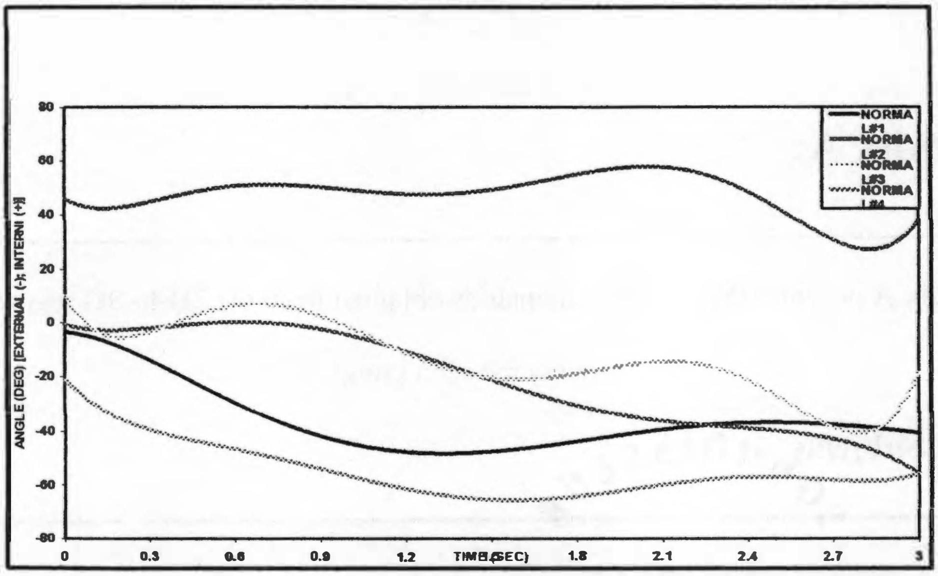

Figure A-2: Normal Subject Axial Rotation Angle of the Humerus

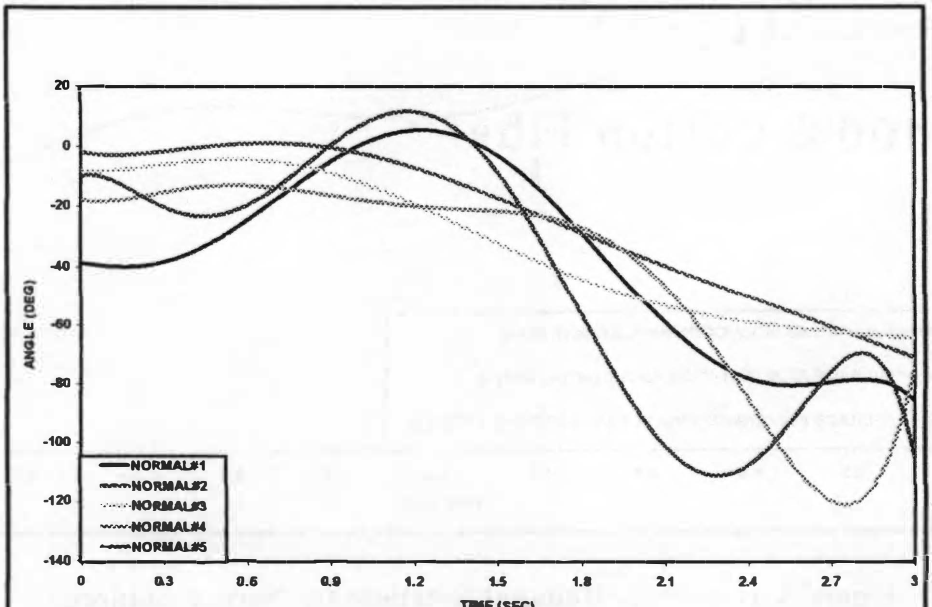

Figure A-3: Normal Subject Flexion/Extension of the Humerus

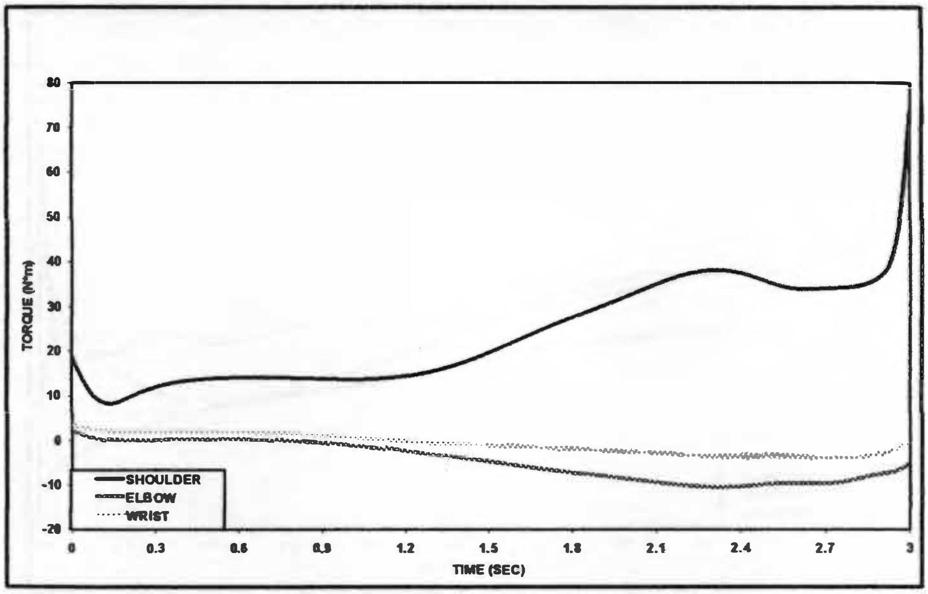

Figure A-4: Average Normal Resultant Joint Torques

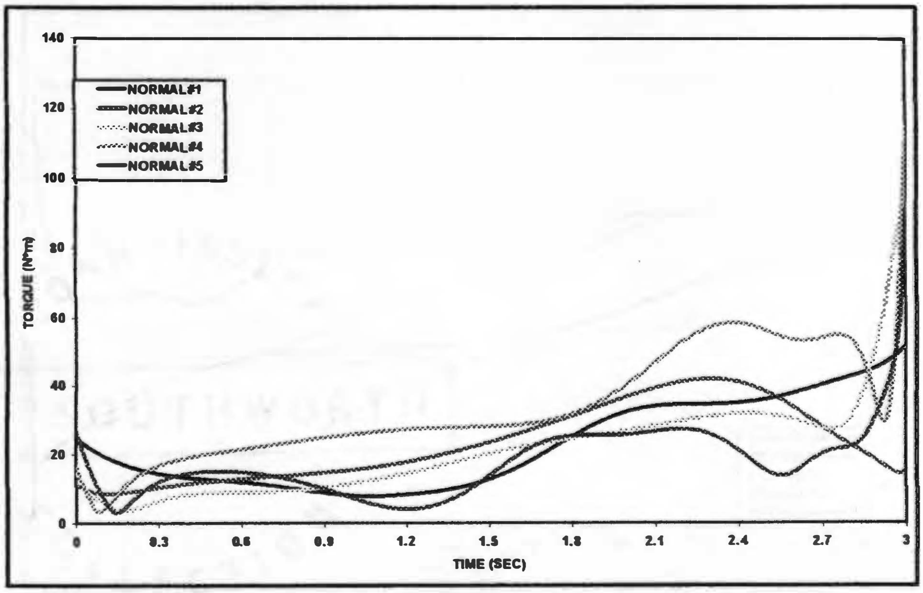

Figure A-5: Normal Subject Resultant Shoulder Joint Torque

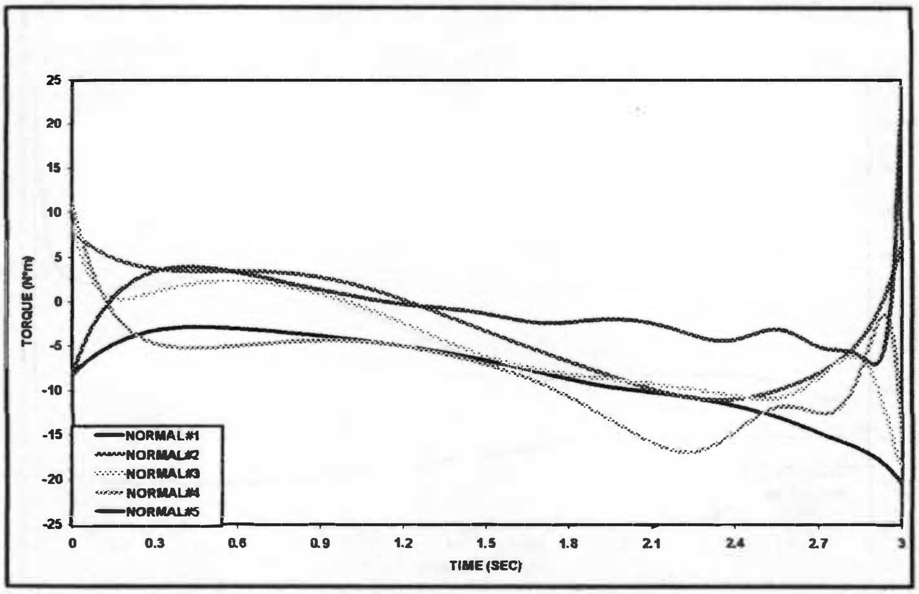

Figure A-6: Normal Subject Resultant Elbow Joint Torque

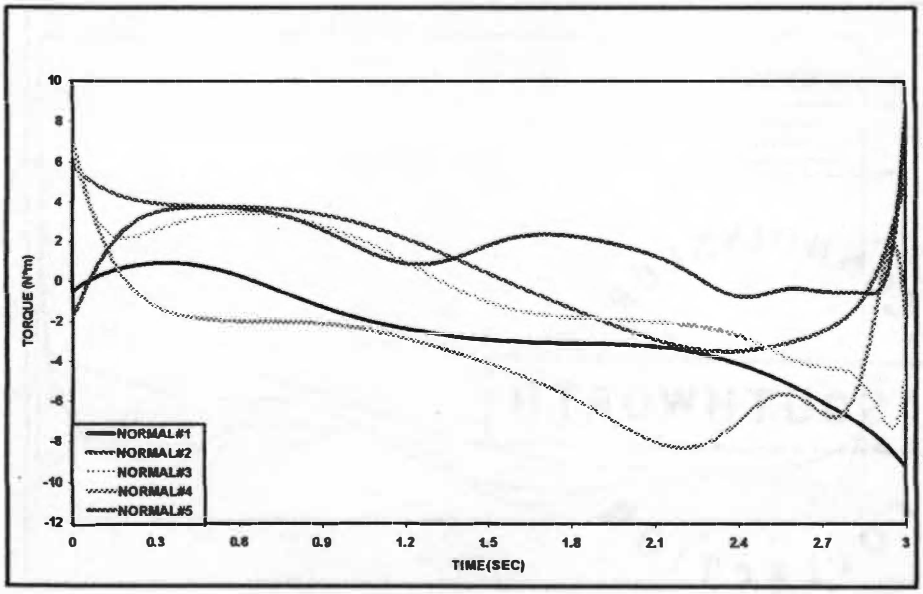

Figure A-7: Normal Subject Resultant Wrist Joint Torque

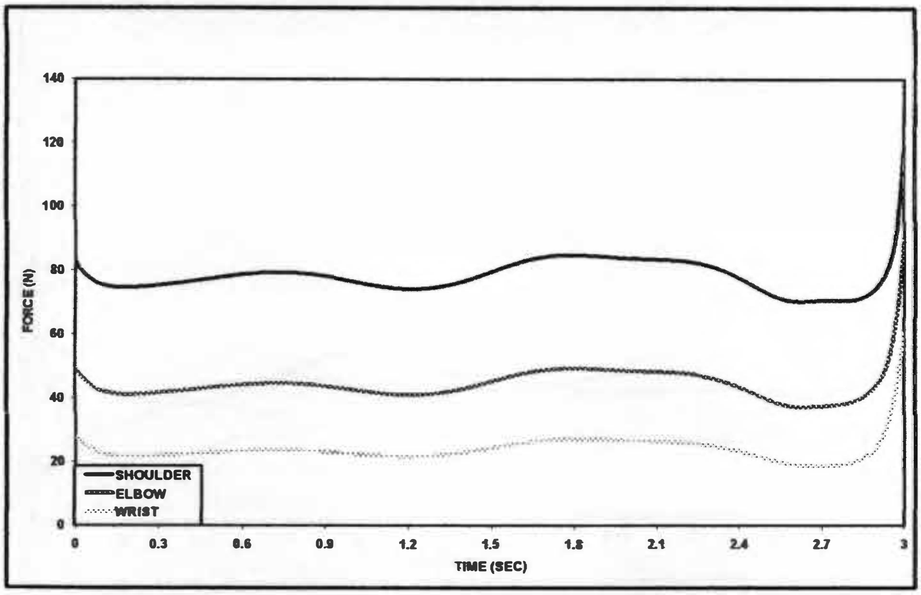

Figure A-8: Average Normal Resultant Joint Forces

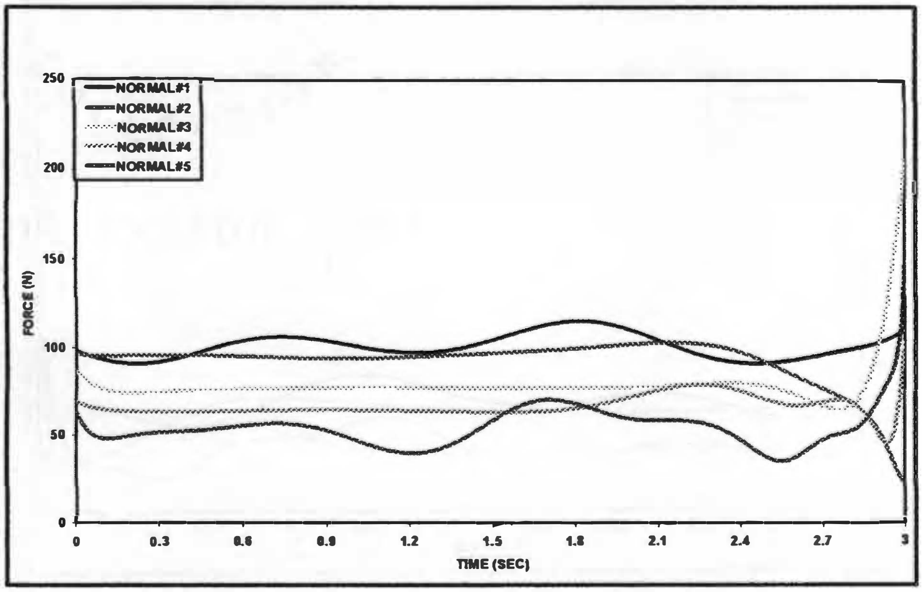

Figure A-9: Normal Subject Resultant Shoulder Joint Force

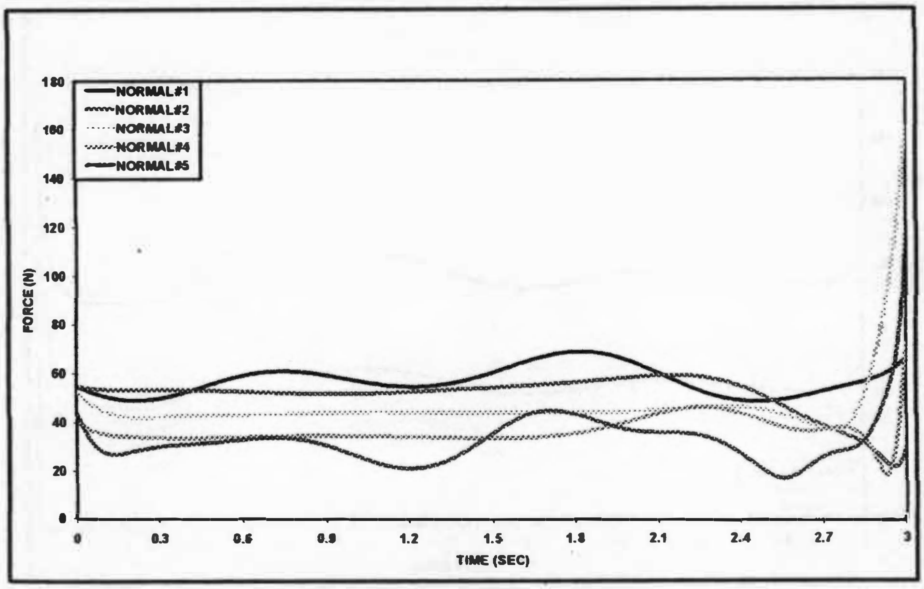

Figure A-10: Normal Subject Resultant Elbow Joint Force

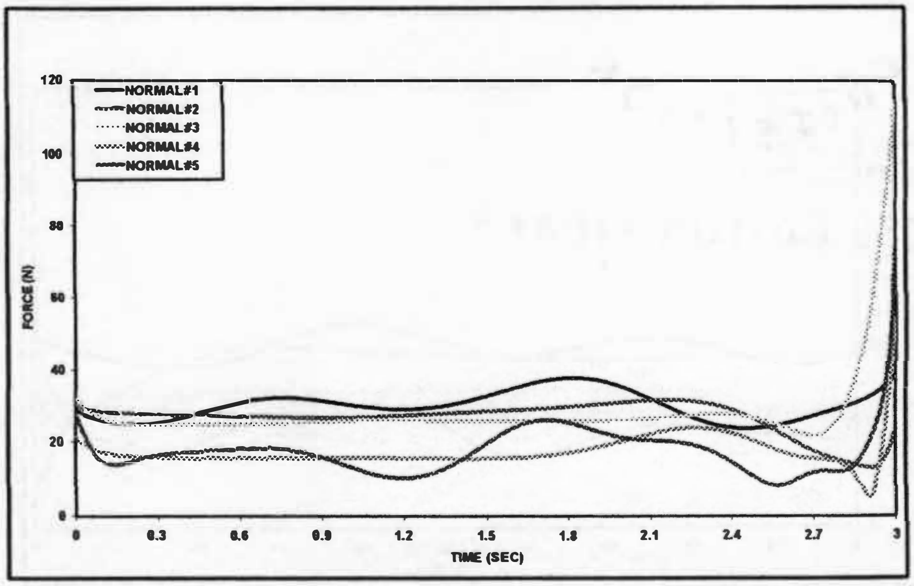

Figure A-11: Normal Subject Resultant Wrist Joint Force

RCD Subjects

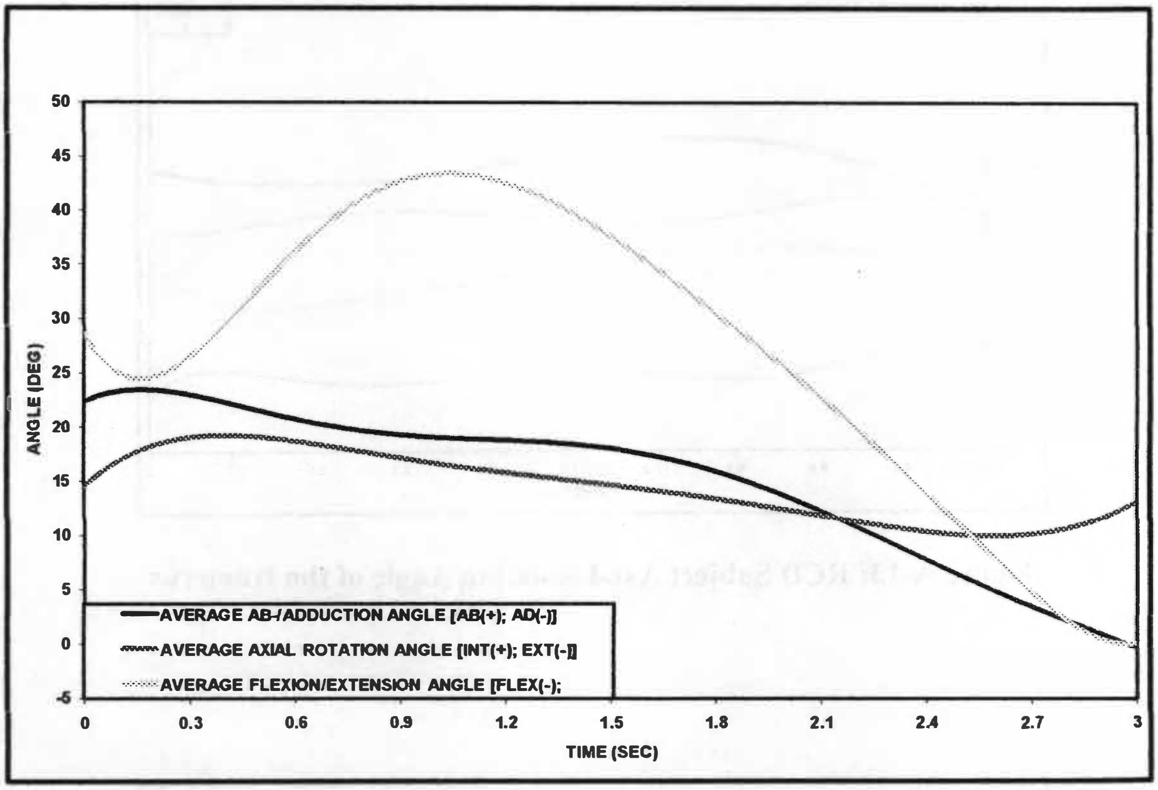

Figure A-12: Average Humeral Rotations for RCD Subjects

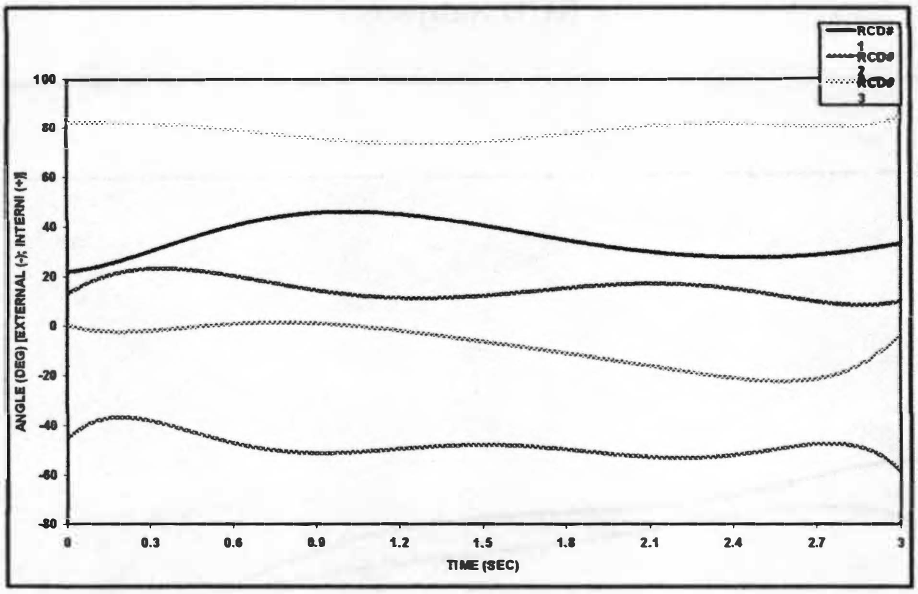

Figure A-13: RCD Subject Axial Rotation Angle of the Humerus

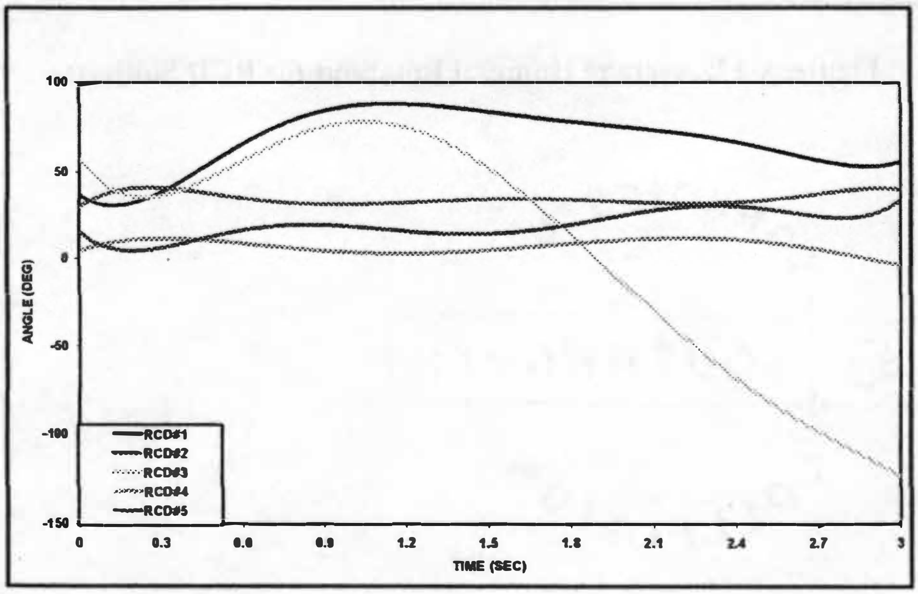

Figure A-14: RCD Subject Flexion/Extension Angle of the Humerus

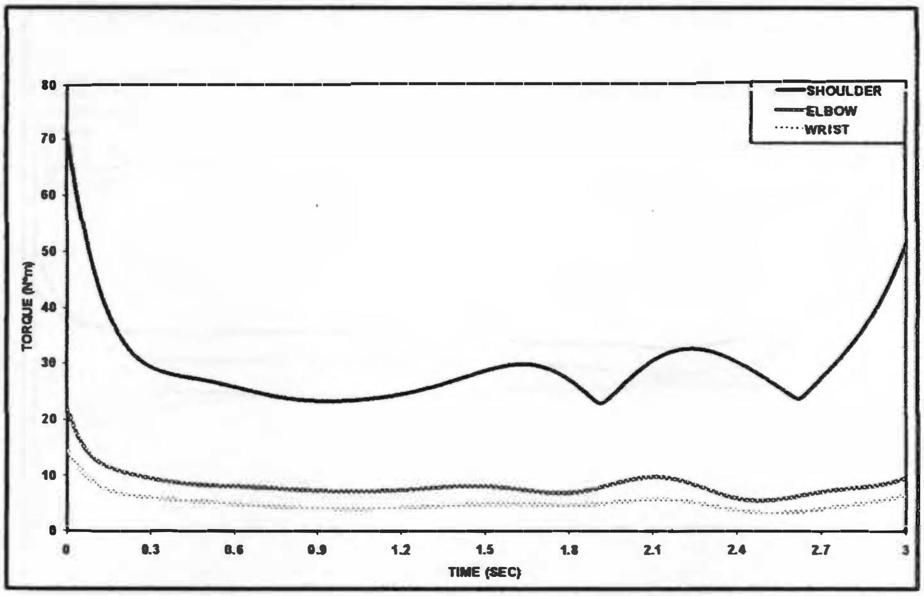

Figure A-15: Average RCD Resultant Joint Torques

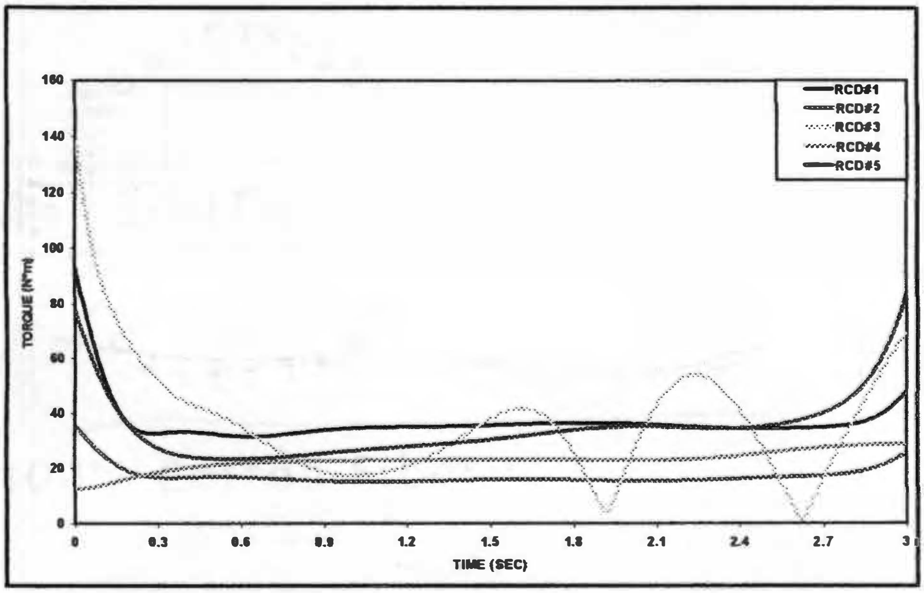

Figure A-16: RCD Subject Resultant Shoulder Joint Torque

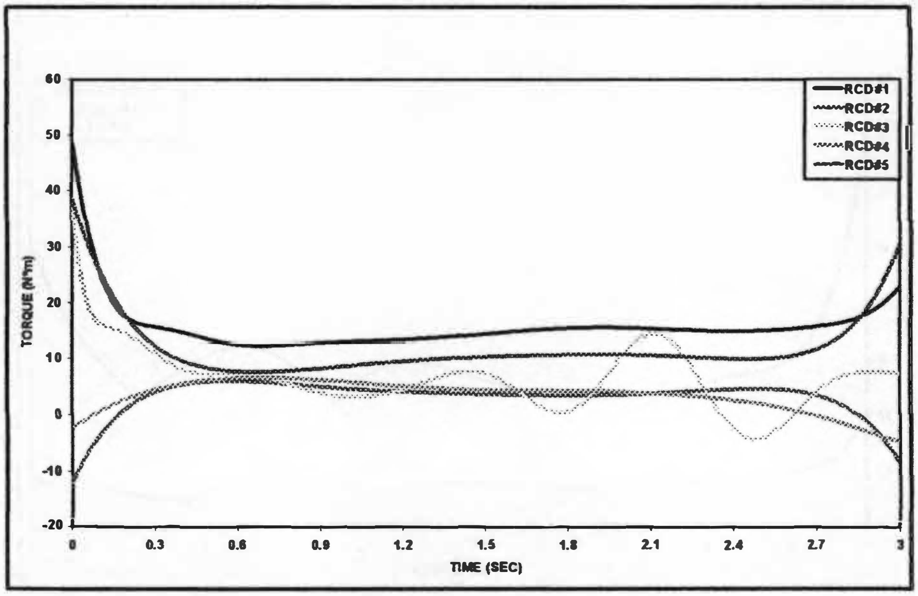

Figure A-17: RCD Subject Resultant Elbow Joint Torque

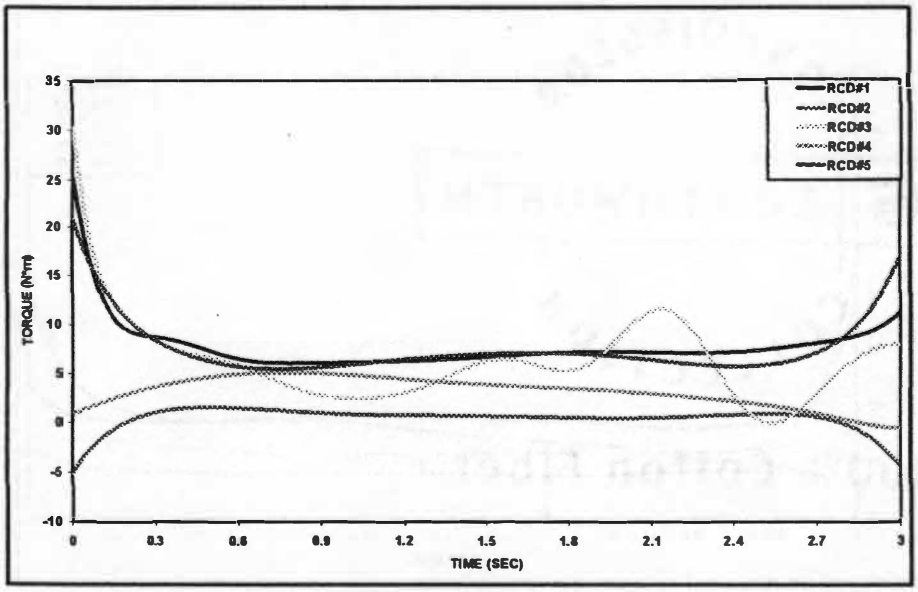

Figure A-18: RCD Subject Resultant Wrist Joint Torque

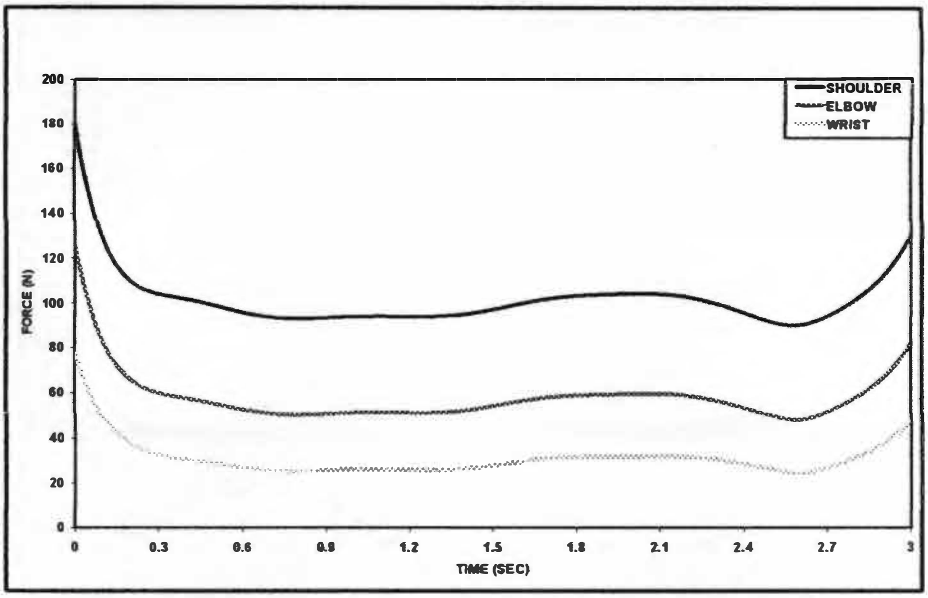

Figure A-19: Average RCD Resultant Joint Forces

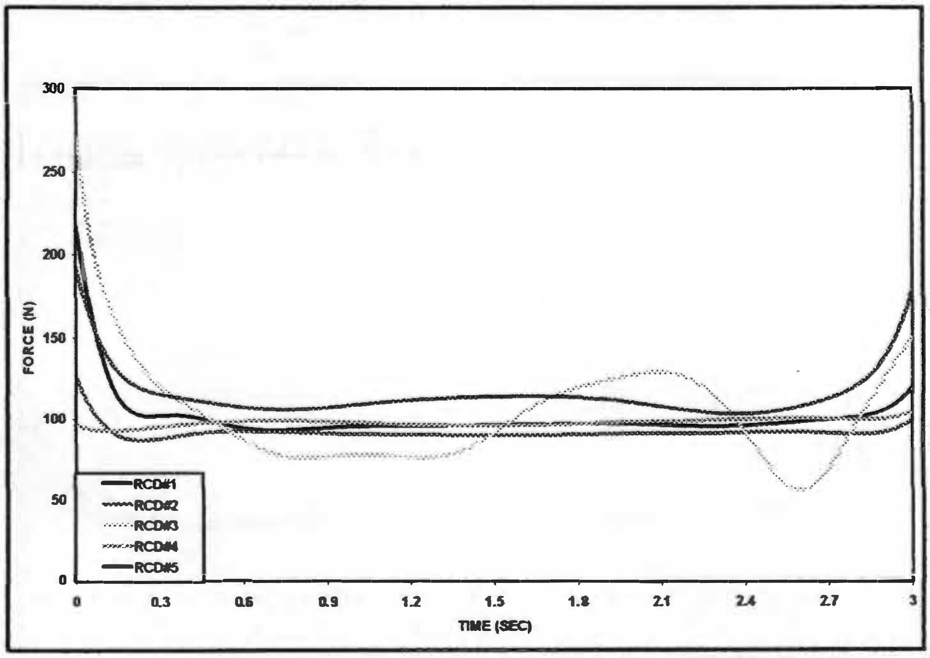

Figure A-20: RCD Subject Resultant Shoulder Joint Force

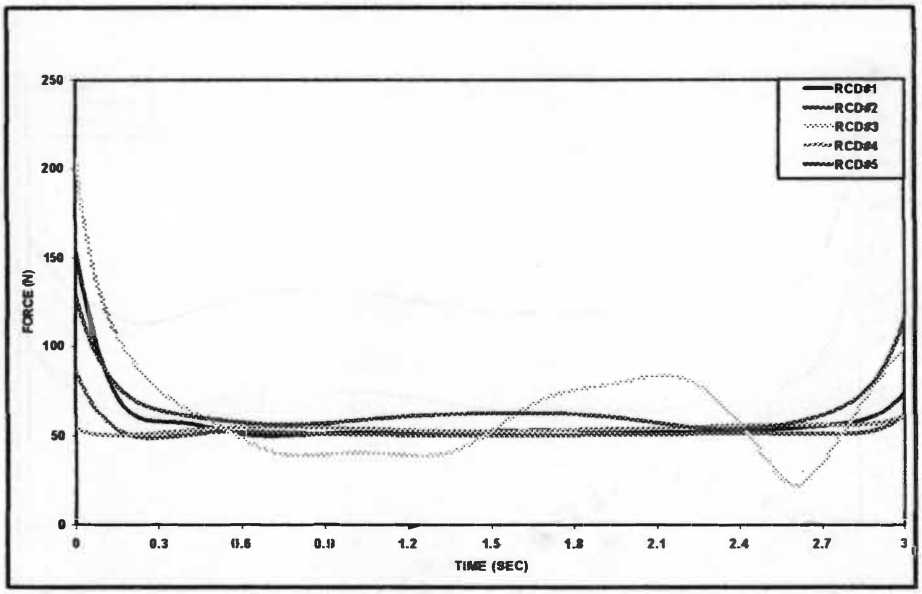

Figure A-21: RCD Subject Resultant Elbow Joint Force

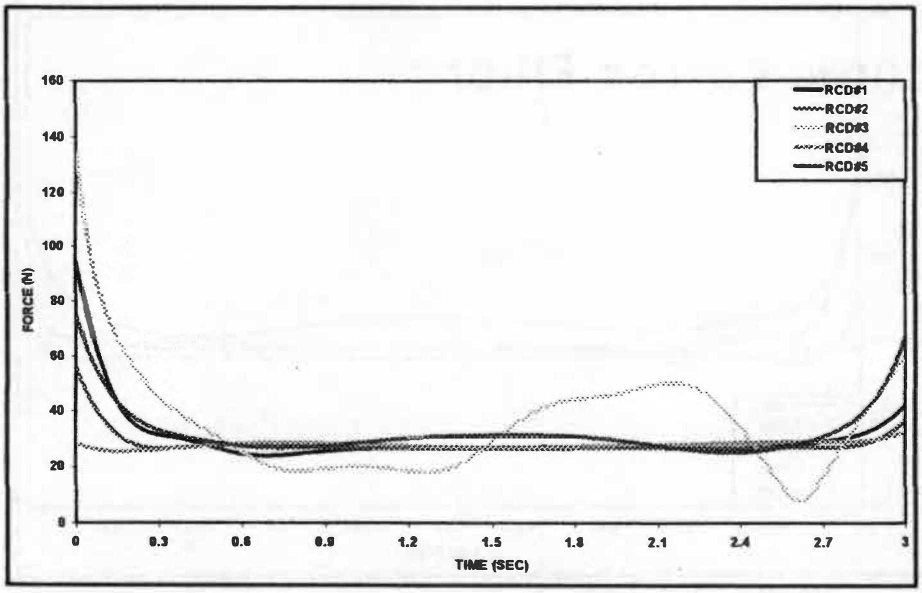

Figure A-22: RCD Subject Resultant Wrist Joint Force

RSA Subjects

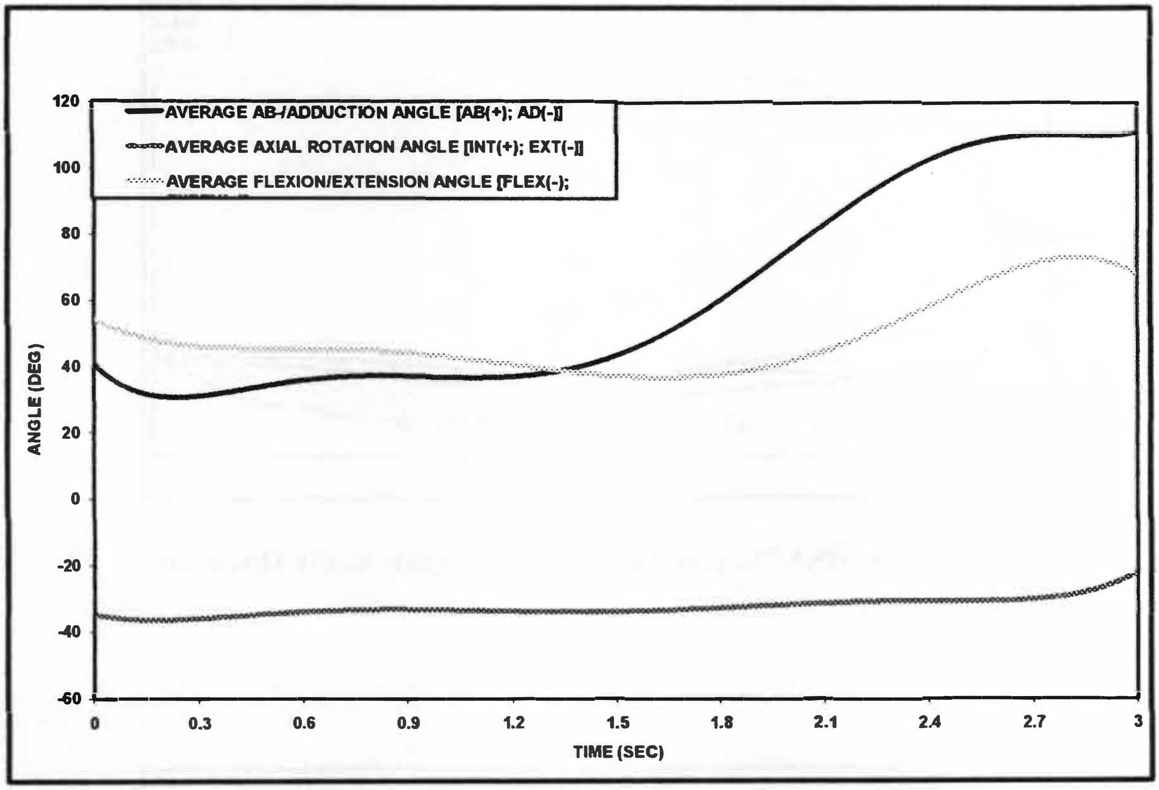

Figure A-23: Average Humeral Rotations for RSA Subjects

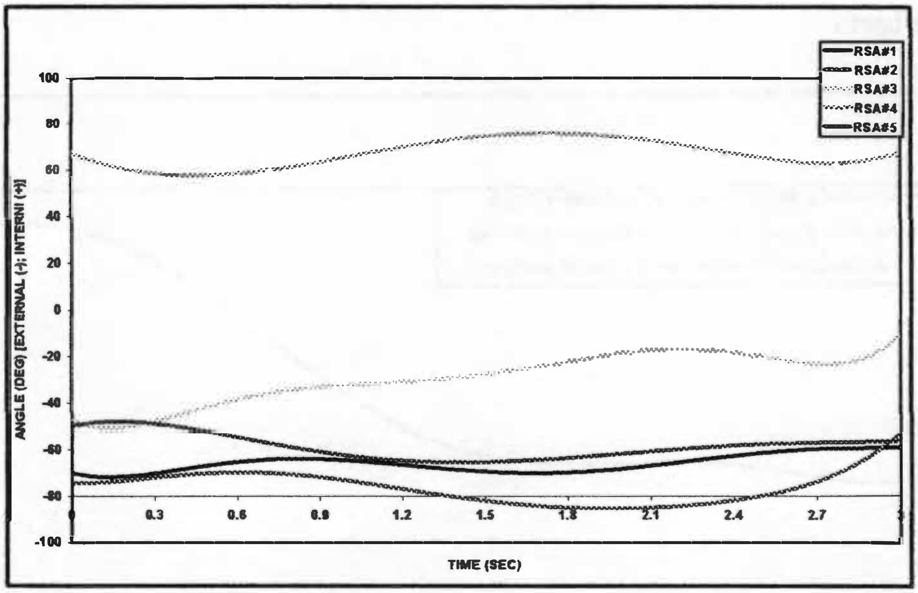

Figure A-24: RSA Subject Axial Rotation Angle of the Humerus

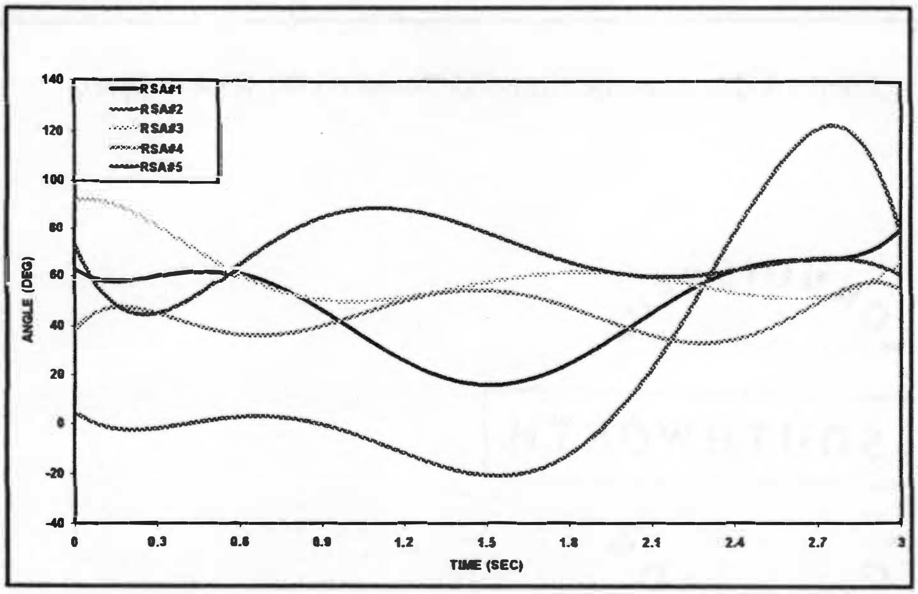

Figure A-25: RSA Subject Flexion/Extention Angle of the Humerus

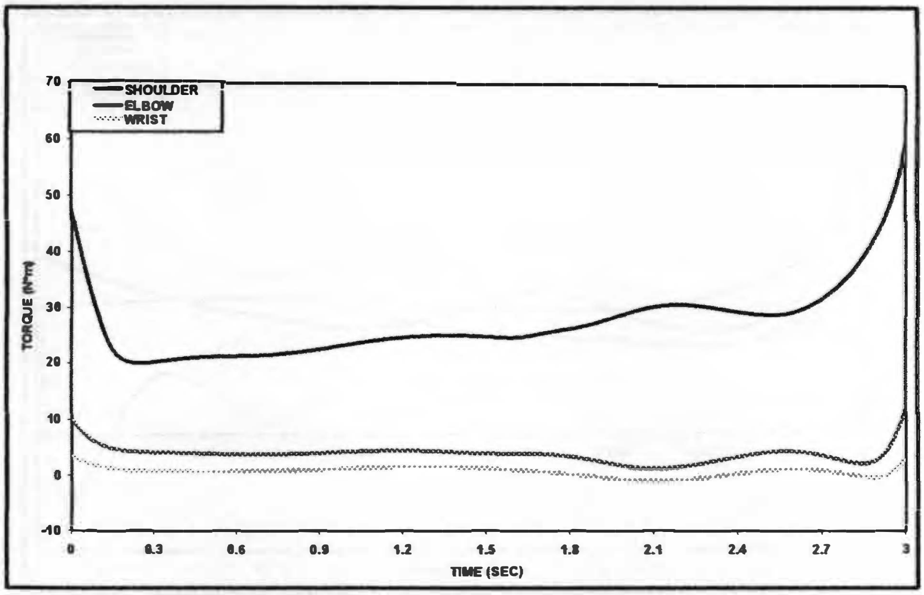

Figure A-26: Average RSA Resultant Joint Torques

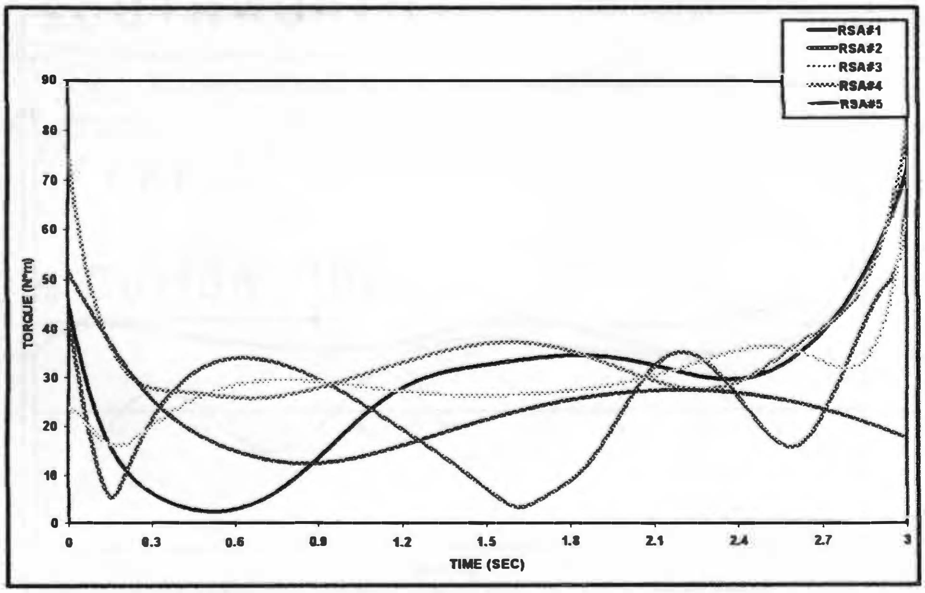

Figure A-27: RSA Subject Resultant Shoulder Joint Torque

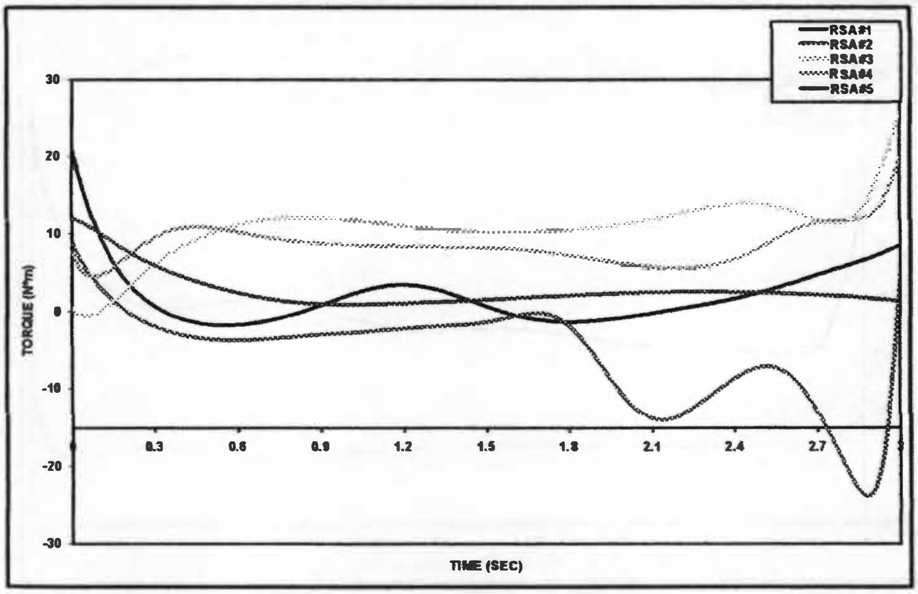

Figure A-28: RSA Subject Resultant Elbow Joint Torque

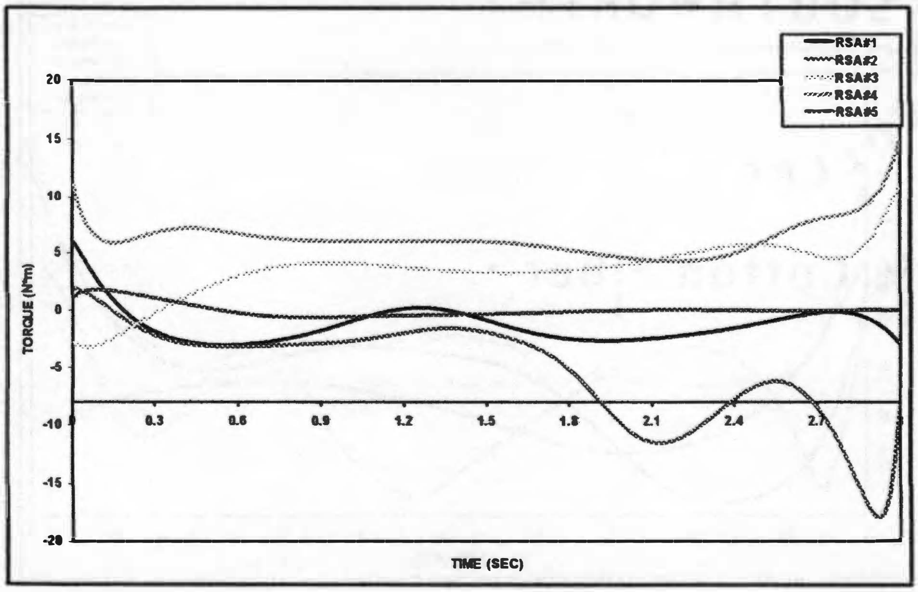

Figure A-29: RSA Subject Resultant Wrist Joint Torque

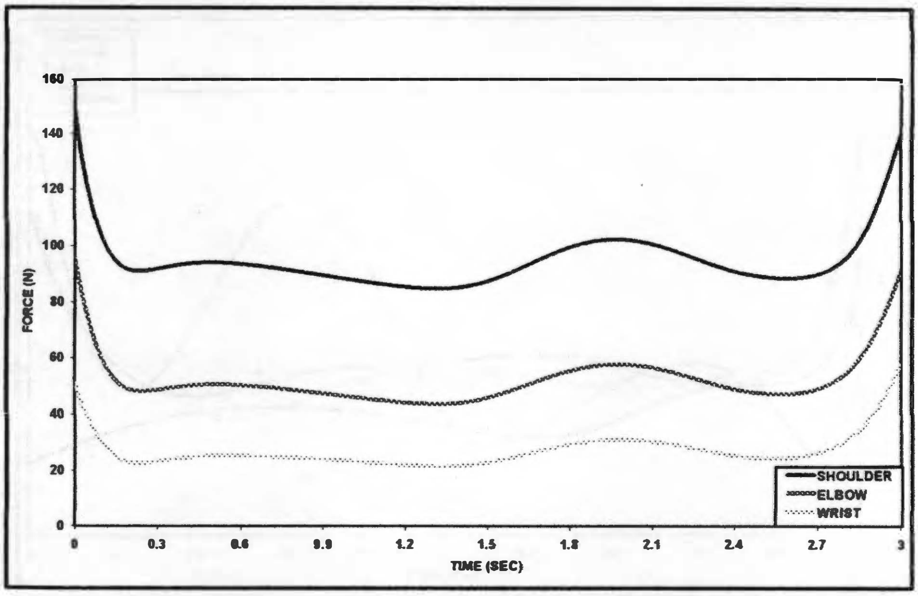

Figure A-30: Average RSA Resultant Joint Forces

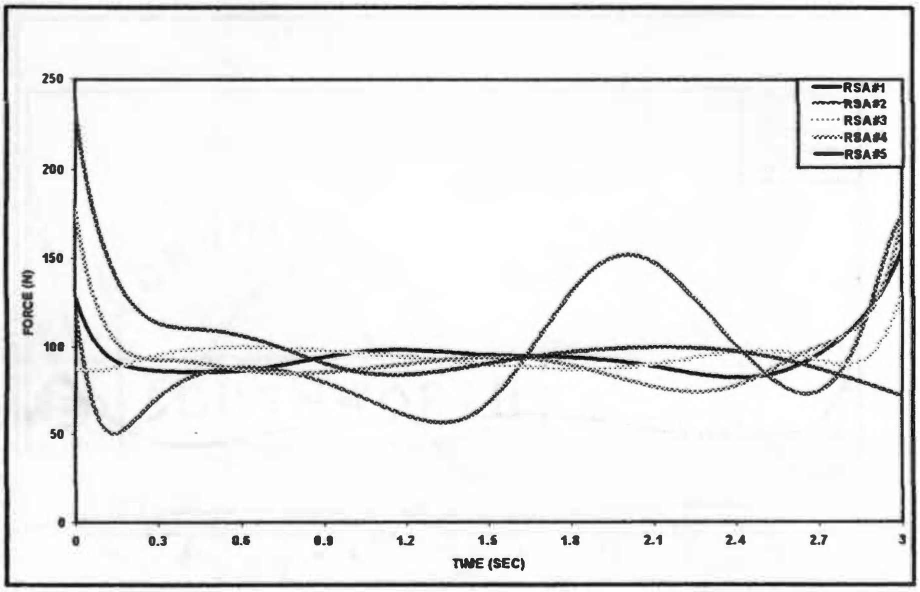

Figure A-31: RSA Subject Resultant Shoulder Joint Force

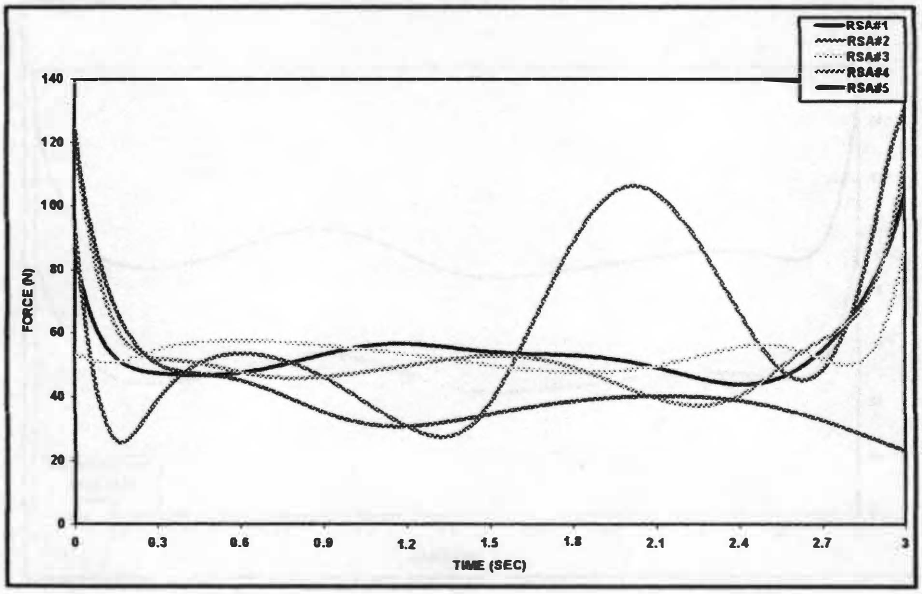

Figure A-32: RSA Subject Resultant Elbow Joint Force

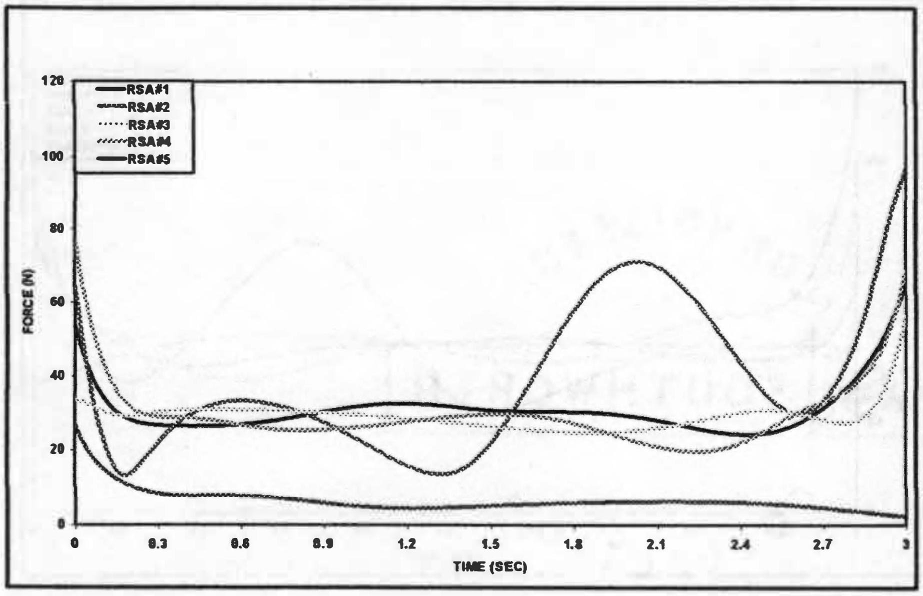

Figure A-33: RSA Subject Resultant Wrist Joint Force

TSA Subjects

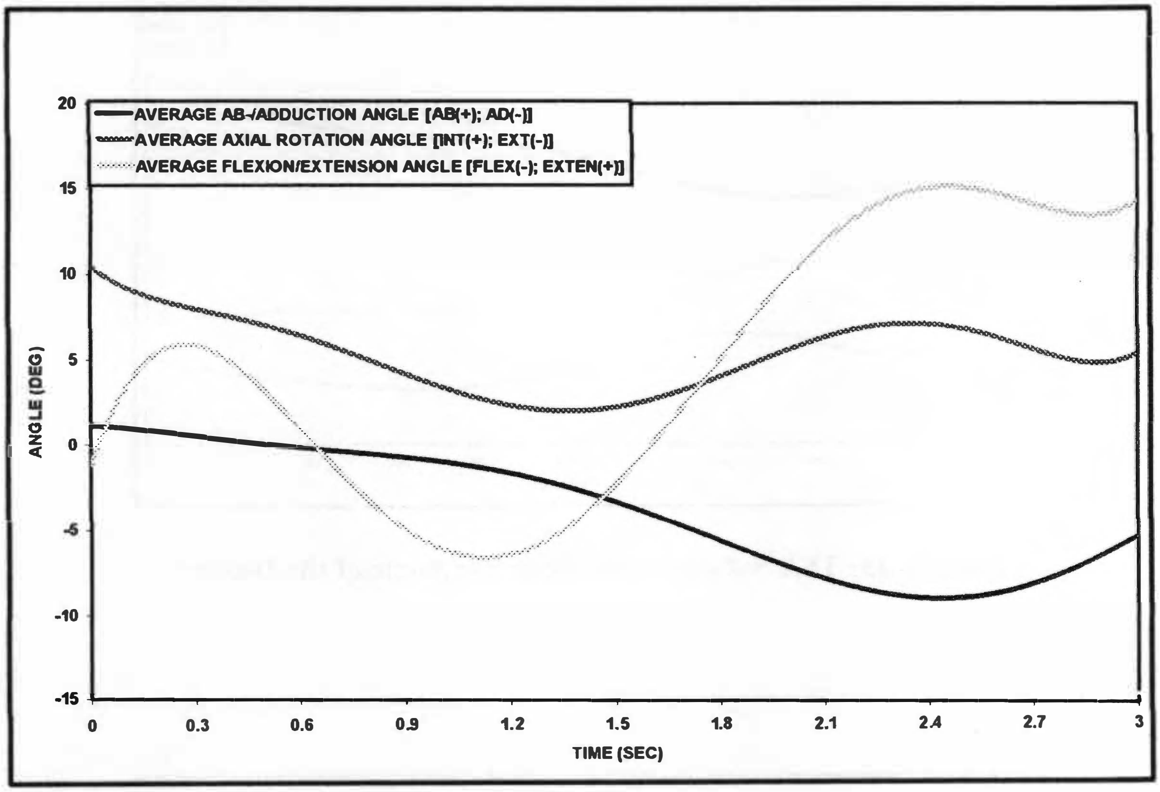

Figure A-34: Average Humeral Rotations for TSA Subjects

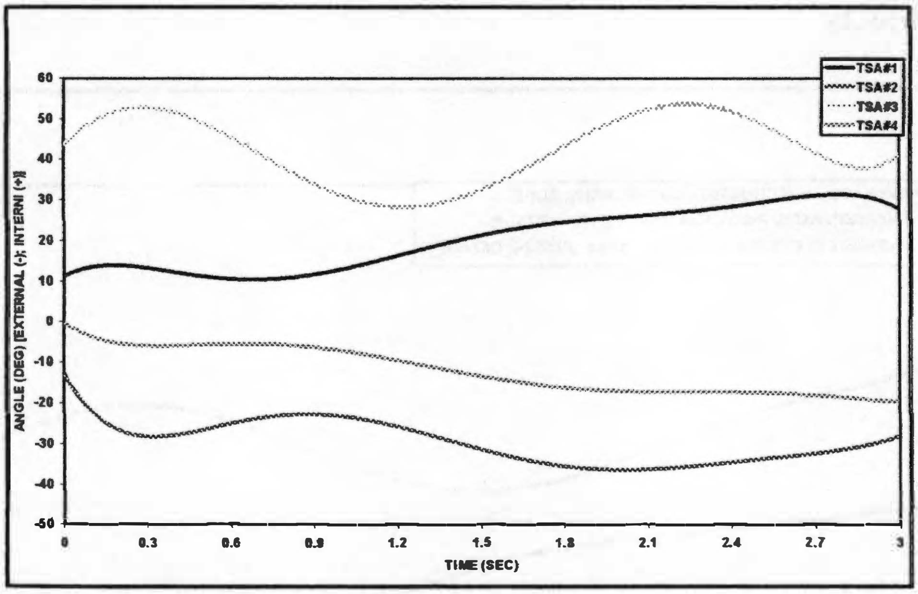

Figure A-35: TSA Subject Axial Rotation Angle of the Humerus

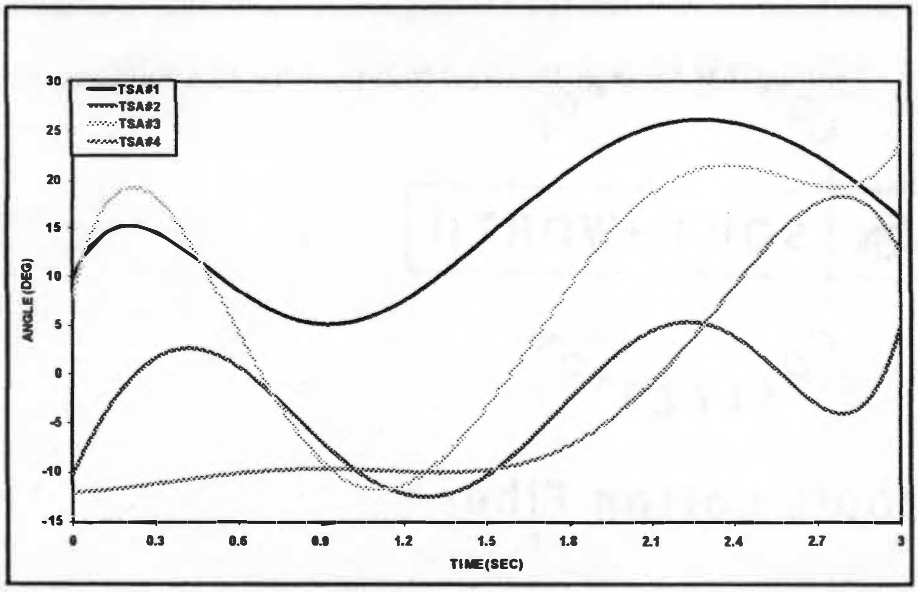

Figure A-36: TSA Subject Flexion/Extension Angle of the Humerus

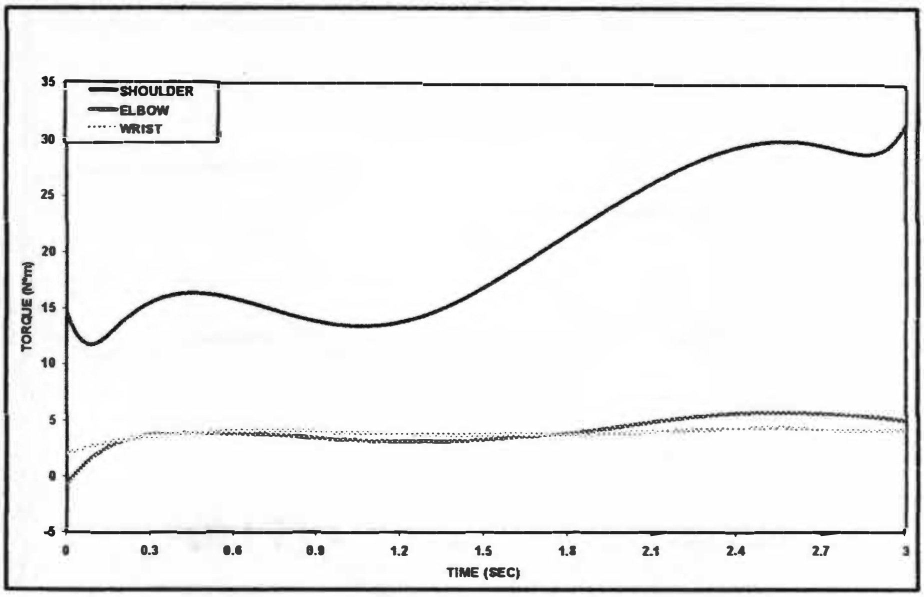

Figure A-37: Average TSA Resultant Joint Torques

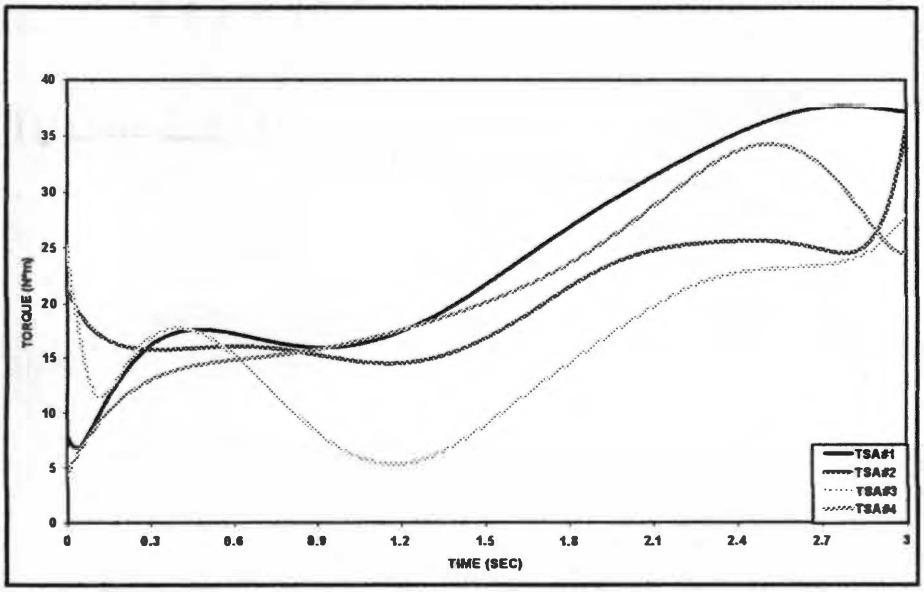

Figure A-38: TSA Subject Resultant Shoulder Joint Torque

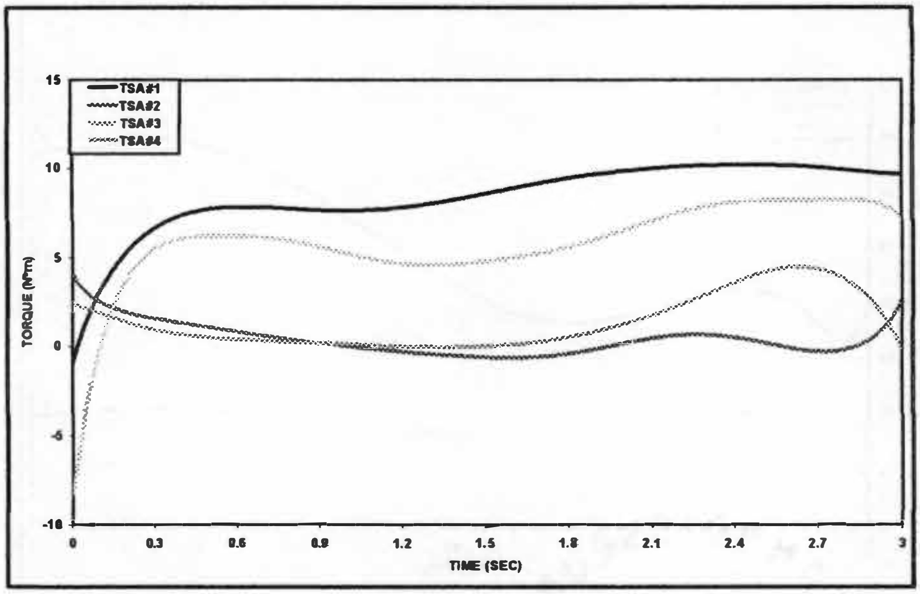

Figure A-39: TSA Subject Resultant Elbow Joint Torque

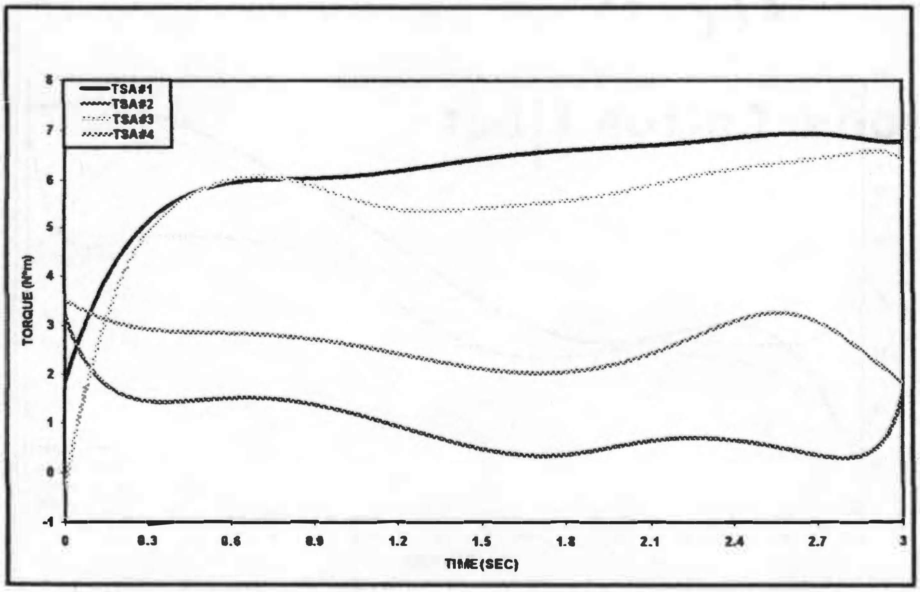

Figure A-40: TSA Subject Resultant Wrist Joint Torque

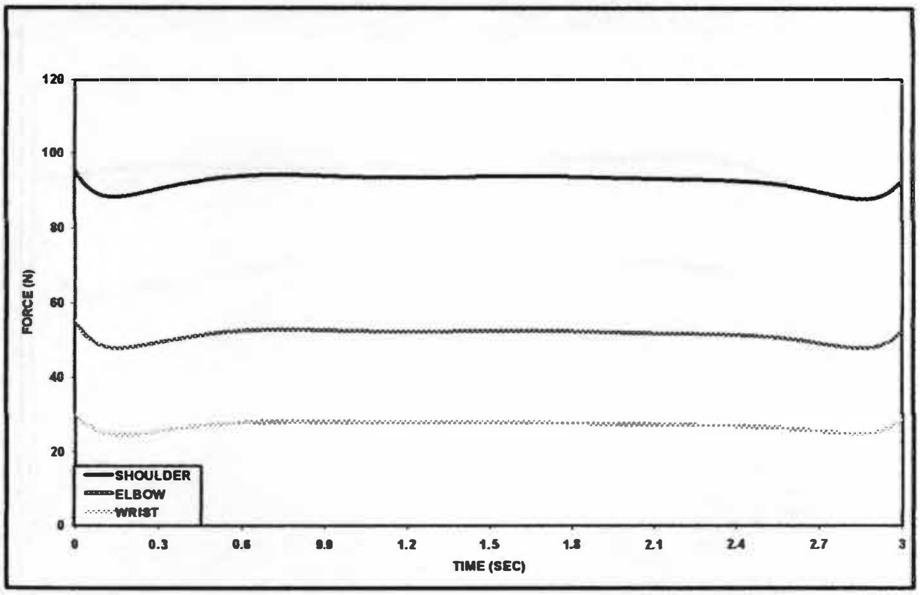

Figure A-41: Average TSA Resultant Joint Forces

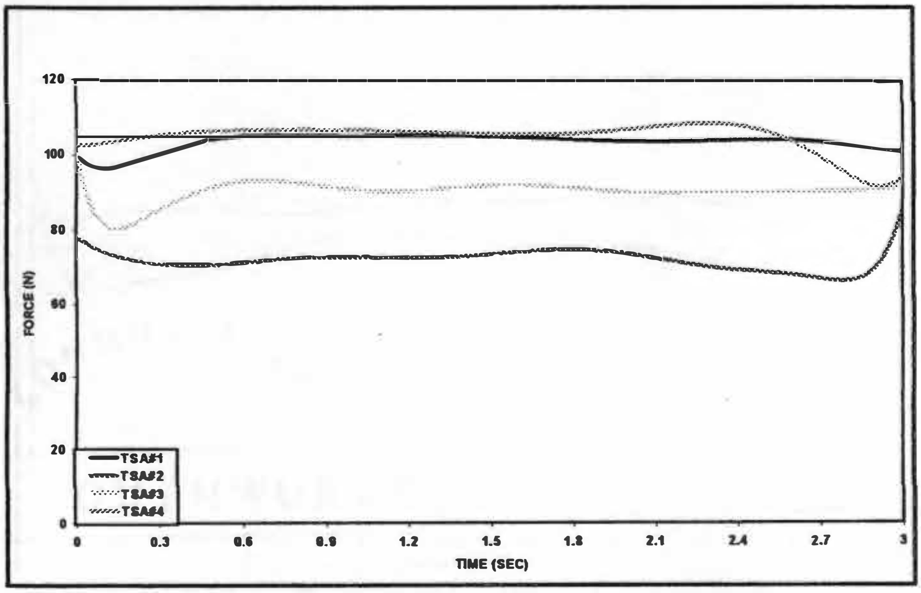

Figure A-42: TSA Subject Resultant Shoulder Joint Force

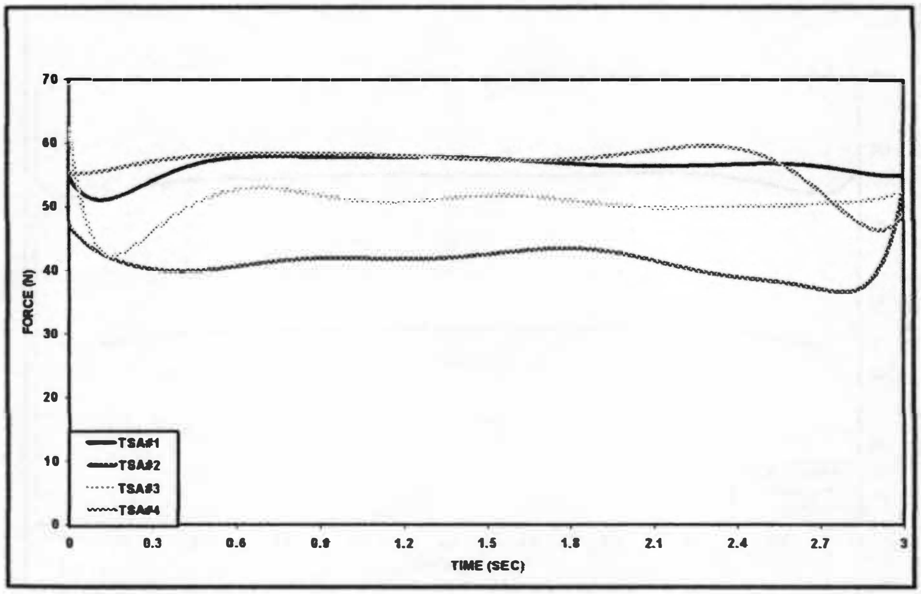

Figure A-43: TSA Subject Resultant Elbow Joint Force

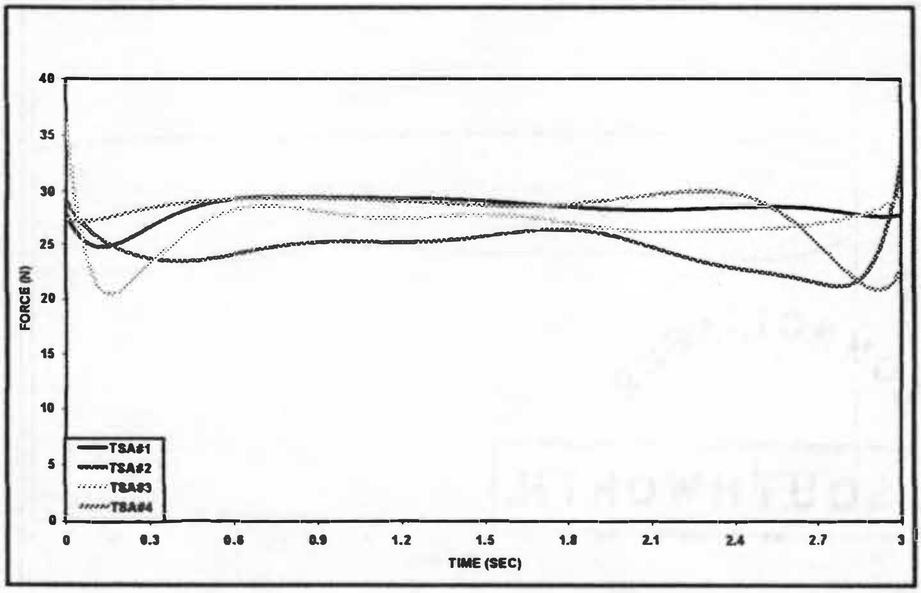

Figure A-44: TSA Subject Resultant Wrist Joint Force

Appendix B

Although Kane's Dynamics is its own entity, it incorporates the advantages of classic theory – namely Newton's Laws and Lagrange's equations. There is also application of d'Alambert's Principle.

In the use of 'Newton-Euler' methods (Newton's laws, momentum principles, and d'Alembert's principle) free-body diagrams of each body in the system are examined. Force or momentum balances then lead to the governing equations. These equations thus contain the interactive and constraint forces acting between the bodies. Hence, with Newton Euler methods the number of equations is as large as the number of variables. Therefore, although the procedure is comprehensive in that all forces and all kinematic variables are needed in the analysis, the procedure is also inefficient – particularly for large multi-body systems.

The use of Lagrange's equations avoids these difficulties by providing an efficient handling of the interactive and constraint forces. With Lagrange's equations, "nonworking" interactive and constraint forces are automatically eliminated from the analysis. This is primarily accomplished through the use of "generalized forces". The disadvantage with Lagrange's equation however lies in the fact that the scalar energy functions (kinetic energy and potential energy) need to be differentiated. This causes a problem when dealing with large multibody systems where the differentiations are extremely cumbersome and unwieldy.

Kane's method combines the advantages of both Newton-Euler methods and the Lagrangian method without introducing the corresponding disadvantages. By using generalized forces, this method avoids the incorporation of non-contributing interactive and constraint forces between the bodies. Also this method avoids the use of energy functions. So the differentiation problem as experienced in the Lagrange's method does not arise. Also in this method differentiation needed to compute velocities and accelerations are obtained through the use of vector products. Therefore this method generates faster results and is well suited for automated numerical computation [text cited from Houston, 1990].

The key to the simplifying power of Kane's method in solving rigid, multi-body dynamics problems lies in his use of d'Alembert's principle. The principle states that the sum of the generalized active forces and the generalized inertia forces is equal to zero. This principle has been more recently recognized as "Kane's Equation" (Houston 1990).

The use of special quantities called generalized speeds, partial velocities, and partial angular velocities is fundamental to the formulation of Kane's Equation, and, thus, the solution to our rigid multi-body dynamics problem. The following is a brief explanation of how one may arrive to a solution using Kane's Equation:

Consider a body B and its mass center, BO, in a reference frame N, with n=6 DOF – having three translational and three rotational degrees of freedom. The configuration of B in N can be described by using quantities called generalized coordinates, $\mathbf{q}_r$ where r is equal to n. Generalized coordinates can either be orientation angles in N of B or translations in N of points fixed on B. Now, the velocity of BO in N, ${}^{N}v^{BO}$, and the angular velocity of B in N, ${}^{N}\omega^{B}$, can be described by

$$ {}^{N}v^{BO} = u_1 * N_1 + u_2 * N_2 + u_3 * N_3 \qquad \text{(B-1)} $$

and

$$ {}^{N}\omega^{B} = u_4 * N_1 + u_5 * N_2 + u_6 * N_3, \qquad \text{(B-2)} $$

respectively, where u_1, u_2, u_3, u_4, u_5, and u_6 are linear combinations of the generalized coordinate derivatives; they are more commonly known as generalized speeds. The first three generalized speeds describe the velocity of BO in N, while the last three describe the angular velocity of B in N. The beauty of generalized speeds is that their incorporation into the angular and translational velocity vectors in the model limits the dynamical equations to first order, therefore increasing computational efficiency.

The generalized speeds are incorporated by introducing partial velocities and partial angular velocities. Partial angular and partial translational velocities are created by differentiating the angular velocity of a body and the translational velocity of its mass center with respect to generalized coordinate derivatives, $\dot{q}_r$. Consider again body B and its mass center, BO. For *n* DOF the partial velocity of BO and partial angular velocity of B in N are defined as follows:

$$^{N}v^{BO}=\sum_{r=1}^{n}{}^{N}\tilde{v}_r^{BO}u_r+\tilde{v}_t \tag{B-3}$$

and

$$^{N}\omega^{B}=\sum_{r=1}^{n}{}^{N}\tilde{\omega}_r^{B}u_r+\tilde{\omega}_t\ , \tag{B-4}$$

where ${}^{N}\tilde{v}_r^{BO}$ is the r^{th} partial velocity of BO in N, and ${}^{N}\tilde{\omega}_r^{B}$ is the r^{th} partial angular velocity of B in reference frame N. The terms $\tilde{v}_t$ and $\tilde{\omega}_t$ are called the partial velocity remainder and partial angular velocity remainder, respectively.

Now, let us assume a set S of *p* points is defined on B, upon which contact and distance forces are acting, as P_m (m=1,..., *p*). For each generalized speed introduced there is an associated generalized active force term. Generalized active forces are defined as

$$\widetilde{F}_r \equiv \sum_{m=1}^{p} {}^N\widetilde{v}_r^{P_m} \cdot R_m \qquad (m = 1,\ldots,p), \tag{B-5}$$

where R_m is the resultant of all forces (contact and distance) acting on points P_m (m= 1,..., p) and ${}^N\widetilde{v}_r^{P_m}$ is the partial velocity of P_m in N. From this definition of generalized active forces, we see a key principle in Kane's method; if a certain point, P_1, say, on B does not have an associate partial velocity, then the forces acting on that point will not be included in the generalized active force term. Furthermore, for that point to have a partial velocity expression associated with it, it must have at least one generalized speed in its velocity expression. If this is not true for P_1, then the forces acting there will be considered as non-contributing and will be neglected from Kane's Equation when it is solved.

We know that any system of forces acting on a rigid body can be replaced by a single resultant force, R, say, and a couple of torque, T. Let point O be the location on B through which R is acting, and assume the action of a torque, T, on B. There is a generalized active force associated with the resultant force and torque acting on B, and is defined by

$$(\widetilde{F}_r)_B = {}^N\widetilde{v}_r^{O} \cdot R + {}^N\widetilde{\omega}_r^{B} \cdot T \qquad (r = 1,\ldots, n). \tag{B-6}$$

This equation is similar to Equation B-5 above, and further implies that, for torques to be solved for; they too must have an associated partial *angular* velocity term. Otherwise, they are neglected.

Again, Kane's Equation states that the sum of the generalized active forces and generalized inertia forces is zero. We have just derived the expressions for generalized active forces, and the derivation of the generalized inertia (also known as "passive") forces is similar. Using the same system of body B in reference frame N, we can replace all inertia forces acting on B with a resultant inertia force, R* and inertia torque, T*. They are determined by

$$R^* \equiv -m^N a^{BO} \tag{B-7}$$

and

$$T^* \equiv -\alpha \cdot \underline{I} - \omega \times \underline{I} \cdot \omega , \tag{B-8}$$

where m is the mass of B, ${}^N a^{BO}$ is the acceleration of BO in N, α is the angular acceleration of body B in N, ω is the angular velocity of B in N, and $\underline{I}$ is the inertia dyadic about the mass center of B. R* and T*, like the active forces, are incorporated into generalized inertia force terms as follows:

$$(\tilde{F}_r{}^*)_B = {}^N\tilde{v}_r^{BO} \cdot R^* + {}^N\tilde{\omega}_r^B \cdot T^* \qquad (r = 1,\ldots, n), \tag{B-9}$$

where, again, we see that no inertia force or torque can be included in the analysis unless it has associated to it a partial velocity term or partial angular velocity term, respectively.

Once the generalized active and generalized inertia forces are accounted for, we can solve Kane's Equation,

$$\tilde{F}_r + \tilde{F}_r^* = 0 \qquad (r = 1,\ldots, n). \tag{B-10}$$

Furthermore, if the number of DOF and generalized speeds are the same, Equation B-10 simplifies to

$$F_r + F_r^* = 0 \qquad (r = 1,\ldots, n). \tag{B-11}$$

This was the case for the present study, and brings up another point – the concept of *constrained* and *unconstrained* forces. In short, if the number of DOF in a system is the same as the number of generalized speeds incorporated into the velocity terms (which implies that the kinematics have been specified), then the resulting partial velocities, partial angular velocities, generalized active forces and generalized inertia forces are *constrained.* In the cases where generalized speeds outnumber the allowable DOF of the system, then at least two generalized speeds are not independent of each other. Furthermore, the aforementioned velocities and forces are deemed *unconstrained.*

In a constrained system, such as the system described above, and the model described in this thesis, each dynamical equation containing a desired unknown is associated with a generalized speed. It is often the case that the unknown forces sought in biomechanical systems are non-contributing (such as contact forces at joints, with equal and opposite components). However, if it is desired to find these non-contributing forces, auxiliary generalized speeds can be used in the velocity terms. 'Auxiliary' means that the generalized speeds have a zero value, yet their presence is needed in the computation in order to formulate the partial velocity and partial angular velocity terms needed to determine the non-contributing forces/torques acting at points (fixed to a body) or bodies in the system. This allows the non-contributing forces to appear in the dynamical equations.

Vita

Matthew Brennon-Kyle Kubo was born and raised in Rock Hill, South Carolina and came to The University of Tennessee as a freshman in 1998. While there he enjoyed marching in The Pride of the Southland marching band for his first three years of college, and had the distinct pleasure of going with the band to march in the Vols' 1998-99 National Championship game against the Florida State Seminoles (which the Vols won 23-16)! He completed his BS in Biomedical Engineering in 2003, and stayed for his MS in Engineering Science for the next two years. During that time he was blessed to meet his now wife-to-be, Rebecca, and will be wed to her on October 15, 2005. Since the successful completion of his thesis defense, Matt has moved to Florida for a new job in orthopaedic design and joyfully awaits his upcoming wedding!